LINEAR COMBUSTION STABILITY ANALYSIS OF OXIDIZER-RICH STAGED COMBUSTION ENGINES

A Dissertation
Presented to
The Academic Faculty

By

Christopher B. Lioi

In Partial Fulfillment
Of the Requirements for the Degree
Doctor of Philosophy in the
School of Aerospace Engineering

Georgia Institute of Technology
May 2019

LINEAR COMBUSTION STABILITY ANALYSIS OF OXIDIZER-RICH STAGED COMBUSTION ENGINES

Approved by:

Dr. Vigor Yang, Advisor
School of Aerospace Engineering
Georgia Institute of Technology

Dr. Timothy Lieuwen
School of Aerospace Engineering
Georgia Institute of Technology

Dr. Lakshmi Sankar
School of Aerospace Engineering
Georgia Institute of Technology

Dr. Robert Funk
Georgia Tech Research Institute
Georgia Institute of Technology

Dr. Krish Ahuja
School of Aerospace Engineering
Georgia Institute of Technology

Date of Approval: November 27th, 2018

To my parents

ACKNOWLEDGEMENTS

Albert Einstein famously remarked that "it is every man's obligation to put back into the world at least the equivalent of what he takes out of it."[1] Thinking back upon my graduate studies, the full weight of this exhortation becomes clear. I will be forever indebted to the many mentors, friends, family members, and collaborators who have helped me achieve my professional and personal goals.

First I would like to extend my most sincere gratitude to my thesis adviser, Dr. Vigor Yang for his support and encouragement throughout my Ph.D. studies. I have been greatly enriched not only by his prodigious technical and scientific expertise, but also his high standards. My own approach to research has been colored by his lessons, and I consider myself to have become a better and more complete scholar under his tutelage. I would also like to thank the other members of my thesis committee Drs. Tim Lieuwen, Krish Ahuja, Lakshmi Sankar, and Rob Funk. I have learned a great deal from each of them both in and out of the classroom.

My graduate studies would have been infinitely more difficult without my many labmates and mentors. Firstly, I owe a huge debt to Dilip Sundaram and Prashant Khare, who put in so much time helping me study for qualifying exams, and setting such sterling examples of graduate research. My labmates and study partners Murali Gopal, Suo Yang, and Shiang Ting-Yeh have also greatly influenced my growth and have challenged me to improve my understanding and research quality. And of course special thanks to my former officemate and comrade Timothy Dawson, who has done so much to help keep me sane.

[1] A. Einstein, *The World as I See It*, 1949

Finally I couldn’t have succeeded without the unwavering love and support of my family. My parents, both of whom are lifelong educators, inspired me from a very young age to pursue higher education. And lastly I am grateful for my partner Chad Bell, who has been extremely patient these past several years. I can only hope to repay his love and patience in kind over the course of our life.

LIST OF TABLES

LIST OF FIGURES

NOMENCLATURE

$\mathcal{A}$	=	Mass-like matrix for wave equation in operator form
A	=	Acoustic amplitude coefficient
$\mathcal{B}$	=	Boundary condition matrix for wave equation in operator form
c	=	Speed of sound (m / s)
c_p	=	Specific heat capacity at constant pressure (J / kg K)
c_V	=	Specific heat capacity at constant volume (J / kg K)
d	=	Orifice spacing in flow distributor
$\mathcal{D}$	=	Species mass diffusivity
$\mathcal{G}$	=	Distributed combustion response matrix for wave equation in operator form
$\mathcal{F}_p$	=	Flame Transfer Function (FTF) based on pressure, x-velocity, y-velocity, w-velocity, or equivalence ratio
k	=	Acoustic wavenumber
L	=	Cavity length (m)
M	=	Mach number, $\bar{u}/\bar{c}$
$\boldsymbol{n}$	=	Unit normal vector
$\boldsymbol{\mathcal{N}}$	=	Wave operator for wave equation in operator form
n_p	=	Pressure coupled gain field of FTF
n_{avg}	=	Average of gain field
$n_{\max}$	=	Maximum of gain field

p	=	Pressure (Pa)
Pr	=	Prandtl number
$\boldsymbol{q}$	=	Parameter vector for sensitivity analysis
$\dot{Q}$	=	Heat release rate
R	=	Cavity radius (m)
$\mathcal{R}$	=	Acoustic reflection coefficient
T	=	Temperature (K)
$\mathcal{T}$	=	Acoustic transmission ceofficient
u	=	Velocity (m / s)
x, r, θ	=	Axial, radial, and azimuthal coordinate in cylindrical coordinates
Y_k	=	Species mass fraction of kth species
Z	=	Acoustic impedance, or mixture fraction

Greek Letters

α	=	Growth constant ($1/\mathrm{s}$)
γ	=	Ratio of specific heats, c_p/c_V
χ	=	Rayleigh conductivity
ν	=	Kinematic viscosity (m^2 / s)
ρ	=	Density ($\mathrm{kg/m}^3$)
ϕ_p	=	Pressure coupled phase field of FTF

ω	=	Angular frequency ($\mathrm{rad/s}$)
Ω	=	Complex eigenfrequency, $\omega + i\alpha$

Subscripts and Superscripts

n, m	=	Azimuthal and radial mode numbers, respectively
b	=	Bias flow
$\sim$	=	Favre-averaged quantity
$\bar{}$	=	Mean value of given quantity
$'$	=	Perturbation value of given quantity
$\hat{}$	=	Complex amplitude of given quantity
$+/-$	=	Downstream / upstream propagating wave

SUMMARY

This thesis concerns the consistent linear acoustic stability analysis of an engine modeled on the RD-170, a prototypical example of an Oxidizer Rich Staged Combustion (ORSC) engine. Both the preburner-turbine assembly as well as the main combustion chamber are studied. The theoretical basis for the stability analysis is an inhomogeneous acoustic wave equation in the pressure.

Boundary effects are accounted for by means of impedance boundary conditions. Theoretical impedance models are employed to describe the physics of various components: the turbine inlet blade row in the preburner assembly, and the flow distributor in the main chamber. In the main chamber, mean flow and combustion response effects are accounted for by means of right hand side source terms in the wave equation.

Two cases are considered for mean flow: piecewise uniform and swirl flow. The swirl flow is generated by time averaging the results from LES of the main chamber injectors. It is found that the mean flow contributes significant damping to the system by means of convecting acoustic energy out of the domain. The swirl flow additionally provides acoustic refraction which further increases the damping. Overall the mean flow is found to far eclipse the other sources of damping.

The response of the combustion to acoustic perturbations is quantified by means of a Flame Transfer Function (FTF). Spatially distributed fields for both the FTF gain and phase are computed from LES data using POD reduction for three different injector recess lengths. A chamber-level response field is constructed as a superposition of fields for individual injectors. It is found that as the recess length decreases, the system becomes

more unstable, due to the fact that the base of the injector nonpremixed flame becomes more exposed to the transverse oscillations in the main chamber. A sensitivity analysis is conducted on a reduced set of scalar quantities which characterize the distributed combustion response fields. The eigenvalue results are found to be most sensitive to the maximum of the gain field, the axial spread of the gain about this maximum value, and the maximum axial slope of the phase field. The radial location of the maximum gain also affects the stability to a lesser extent. The results suggest that to maximize the stability margin of the engine the recess length of the injector should be maximized and the fluid conditions should be such that the flame is wide and combustion is distributed over as large an axial extent as possible.

CHAPTER 1.

Introduction

1.1. Combustion Instabilities

Since their discovery in the late 1930's, combustion instabilities have presented a major obstacle to the design and development of numerous combustion technologies. Over the last half century, a considerable literature on the physics of combustion instabilities has matured in the areas of gas turbines [1], ramjets and scramjets [2, 3], solid [4, 5] and liquid [6, 7] propellant rocket engines, and many others. However, while many of the fundamental physical mechanisms of instability have been elucidated, accurately and consistently determining *a priori* the stability of a combustion device with a complex geometry and a complex flowfield remains a challenging task. The purpose of this dissertation is to begin to fill this gap by developing a numerical modeling framework for combustion instabilities and utilize it to analyze a full scale model oxidizer-rich staged combustion (ORSC) engine. Such engines have recently received increased attention for their potential applications for heavy-lift launch vehicles [8, 9].

Combustion instabilities manifest as coherent, large-amplitude, self-excited flow oscillations centered in narrow bands about the natural acoustic frequencies of the chamber. They result from resonant coupling between the unsteady motions within the chamber and the heat release due to combustion. Low amplitude broadband noise is present in all real combustors in the form of turbulence and acoustic fluctuations. As the flame is perturbed by these unsteady motions, the rate of heat release fluctuates and drives additional flow

oscillations. When the amount of energy added to the acoustic field in this manner exceeds the amount lost due to acoustic radiation and internal damping, the oscillations grow until eventually limited by nonlinear processes. At this point, the system is said to have attained a limit cycle. Only a small fraction of the chemical energy released by combustion must be acquired by oscillatory motions such that their amplitudes become unacceptable. Thus the risk of catastrophic failure is significantly higher for high-energy density systems such as LREs.

The unsteady heat release may not necessarily energize the acoustic field; this depends on the phase relationships between the oscillations in heat release and acoustic pressure. In particular, Rayleigh's criterion [10, 11] dictates that the relative phase between the two must be less than 90 degrees in order for the acoustic field to gain energy. Due to spatial distribution of both quantities, this criterion must be evaluated at each point in the domain; if the following mathematical criterion is met, then Rayleigh's criterion is satisfied:

$$\int_0^\tau \iiint p'(\boldsymbol{r},t)\dot{q}'(\boldsymbol{r},t)\,dV\,dt \geq 0$$

where $\dot{q}'$ represents the fluctuating rate of combustion heat release per unit volume. This physically represents the unsteady work done on the acoustic field during the gas expansion following combustion.

In many LREs, the gas in the main combustion chamber (and the preburner or gas generator depending on the particular cycle) is subject to transcritical or supercritical pressures and temperatures. Many exotic effects arise in this regime, particularly the

disappearance of distinct liquid and gas phases [12, 13]. This may significantly change the character of the flowfield within the combustor. As there are no longer any phase change processes *per se*, there is no time delay associated with atomization or vaporization, but only of interdiffusion of superfluid fuel and oxidizer. Additionally at such high pressures, deviations from ideal gas behavior may become significant. To accurately capture the flow history, the theoretical formulation must be supplemented with an appropriate real fluid equation of state. In general this introduces nonlinear terms into the acoustic wave equation. However, provided that the acoustics remain in the linear regime, such terms may be safely ignored such that all fluid nonidealities may be accounted for in an effective speed of sound [14].

1.2. ORSC Engine Background

Liquid rocket engines may broadly be classified according to the thermodynamic cycle they employ to drive their turbopump assembly. Three important types of engine cycles are expander, gas generator, and staged combustion. In an expander cycle, no combustion takes place before the propellants enter the main combustor. The fuel is heated and expands as it is circulated around the outside of the thrust chamber. In a gas generator cycle, a fraction of the propellants are burned before entering the main combustion chamber and used to drive the turbopump before being exhausted into the diverging portion of the exit nozzle. This allows for the higher pressure head to drive the pump system relative to the expander cycle. Finally, in a staged combustion cycle, a larger fraction of the propellants is combusted in one or more preburners before being passed through the turbine. This may be done in either fuel- or oxidizer-rich mode. The turbine exhaust is then

passed to the main combustion chamber where it is burned with the quantity of the propellants which bypassed the preburner. Staged combustion engines possess numerous advantages over designs employing the other two cycles, particularly lower gas temperatures entering the turbine and higher chamber pressures. High pressures generally have the effect of increasing the overall cycle efficiency, specific impulse, and thrust-to-weight ratio of the engine. Furthermore, oxidizer-rich staged combustion engines exhibit little to no coking or soot formation. The Russian RD-170 is a well-known example of a successful ORSC engine design [15]. A simplified flow diagram for the engine is shown below in Fig. 1 below. A model based on this engine design shall be used throughout this thesis as a case study.

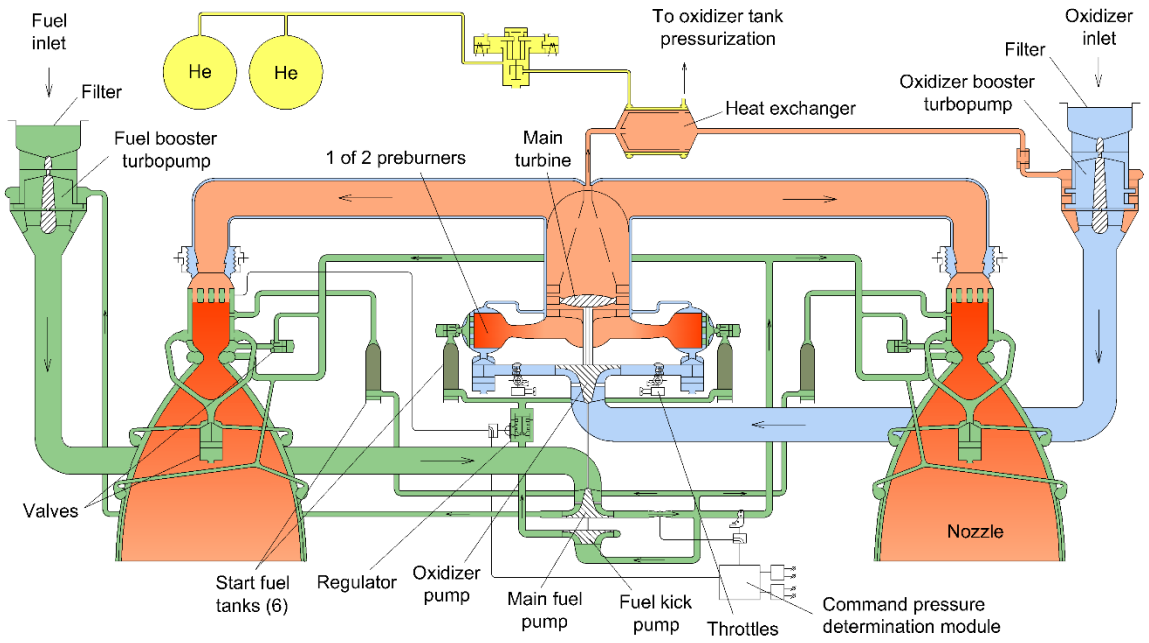

Fig. 1: RD-170 flow diagram

Many previous studies of liquid rocket engine combustion stability have taken the domain of interest to consist only of the main thrust chamber and the converging portion of the exit nozzle. Typically, ad-hoc assumptions are made for upstream boundary conditions. For example, Pieringer et al. [16] assume that the fluctuating mass flow rate vanishes at the injection plane. This condition is equivalent to specifying choked flow, which is a questionable assumption for most liquid rocket engine injectors. Schulze and Sattelmayer [17] correctly note that coupling with feed system components, such as the injectors and propellant domes, may introduce significant additional damping and/or driving effects and must be incorporated in some more comprehensive manner. Towards addressing this concern, this thesis deals with a class of engines which may be idealized to include a main combustion chamber connected by some number of injectors to an oxidizer dome. Fig. 2 and Fig. 3 show respectively the main combustion chamber (MCC) and preburner (PB) of an ORSC engine modeled on the RD-170 engine. Fig. 4 shows the gas volume of the assembly consisting of two preburners joined to the turbine inlet hub. All diagrams are adapted from [9].

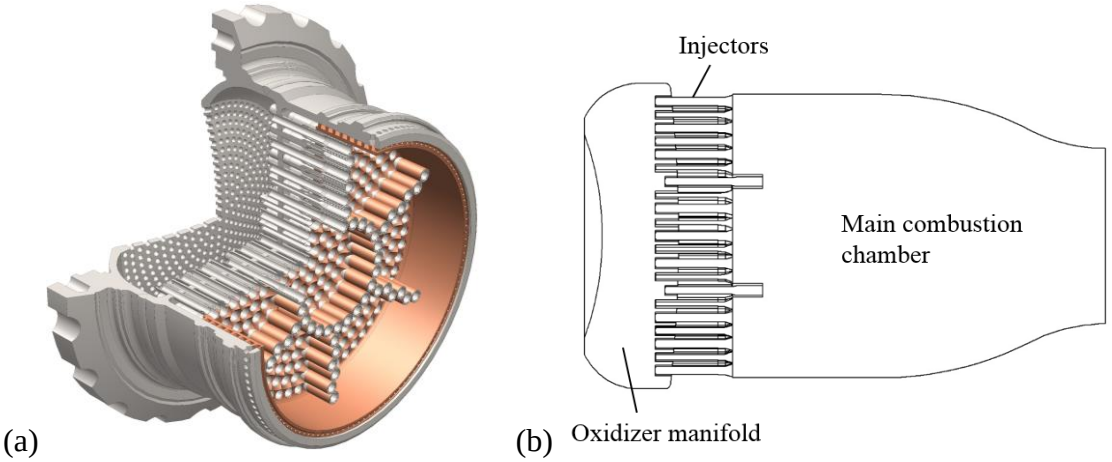

Fig. 2: Schematic of oxidizer-rich staged combustion (ORSC) thrust chamber assembly (a) chamber cross-section (b) longitudinal cutaway of chamber

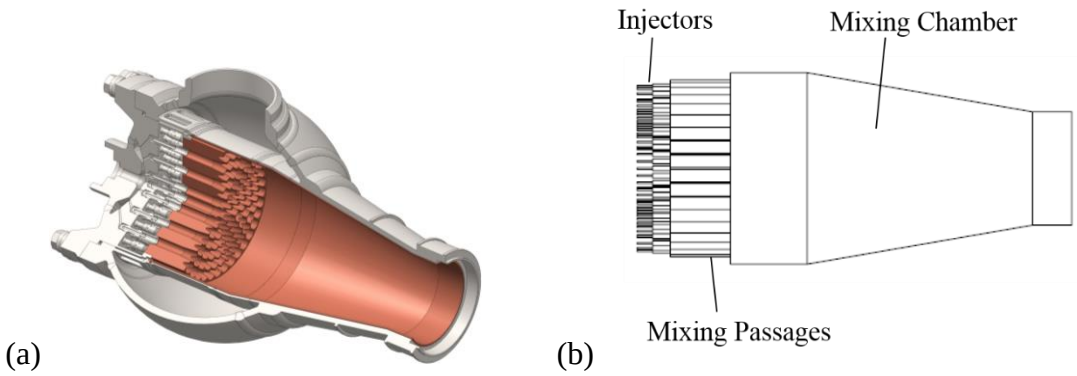

Fig. 3: Schematic of oxidizer-rich staged combustion (ORSC) preburner (a) chamber cross-section (b) longitudinal cutaway of chamber

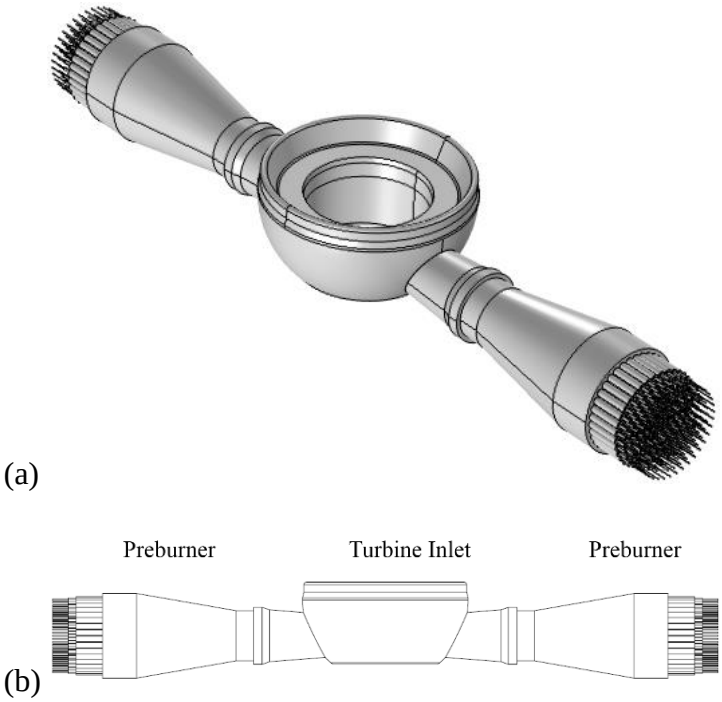

Fig. 4: ORSC engine preburner-turbine assembly (a) 3/4 view of gas volume (b) longitudinal cross section.

When the preburner products of combustion pass through the turbine inlet annulus, they go to drive the main turbopump shaft. A schematic of a turbopump rotor assembly modeled on that of the RD-170 is shown in Fig. 5. The turbine itself consists of several blades emerging radially outward from the central turbine shaft.

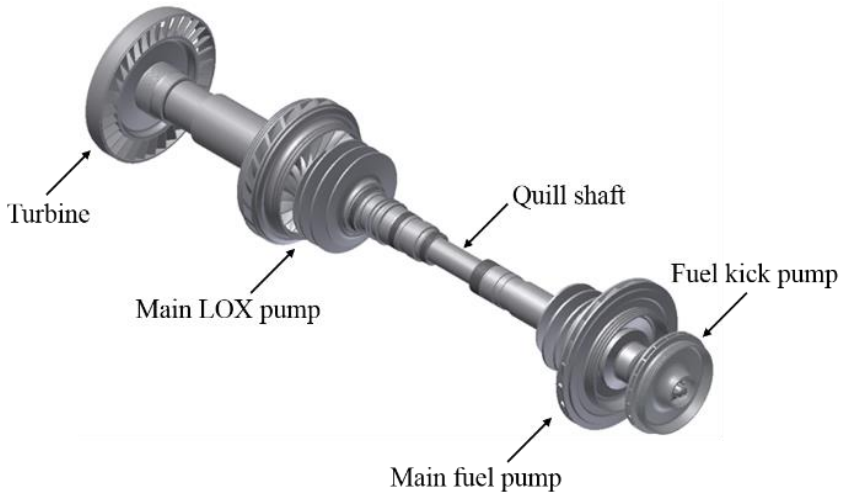

Fig. 5: General model of RD-170 turbopump rotor assembly.

The nature of the flowfield within and near the injectors is critical for determining the acoustic stability of the entire system. Fig. 6 below shows more detailed views of the two types of injector elements in the main combustion chamber, also modeled on the RD-170 engine. Likewise Fig. 7 shows a detailed view of an injector modeled on that of the RD-170 preburner. All injectors in this design are of the gas centered swirled coaxial (GCSC) type. In the main injectors, oxidizer is introduced axially and meets with an annular swirling fuel flow. By contrast, in the preburner injector the fuel and oxidizer stages are reversed, and the fuel is introduced tangentially into the inner passage.

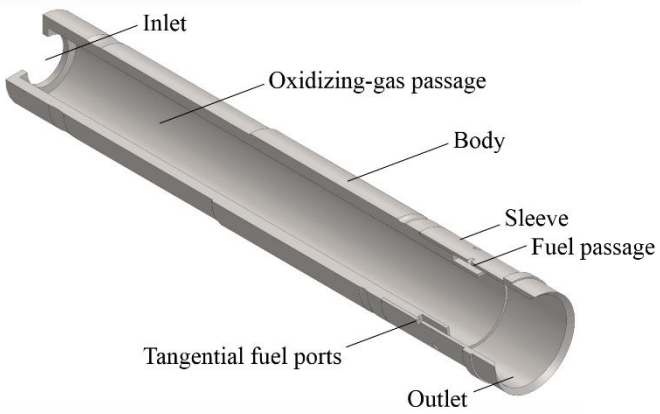

(a)

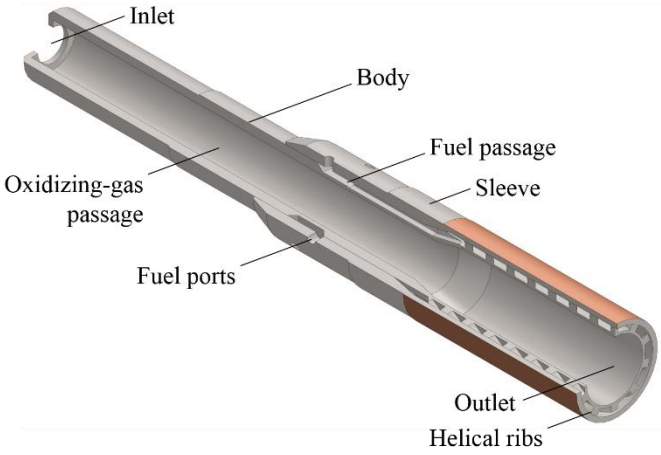

(b)

Fig. 6: Cross-section of injectors in main combustion chamber (a) main injector element (b) baffle injector element

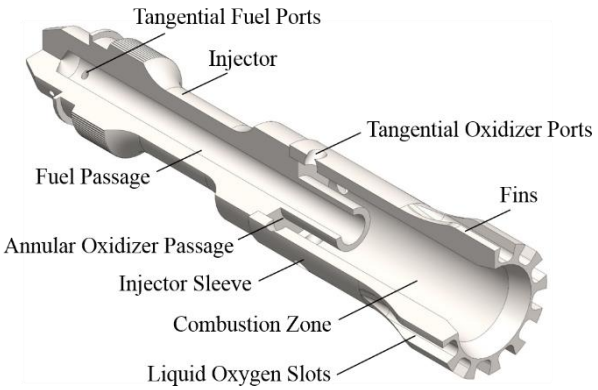

Fig. 7: Cross-section of preburner injector

1.3. Theoretical Analysis

Strategies for predicting combustion instabilities vary on a continuum from purely analytical to purely numerical. Some robust theoretical analyses have been developed, such as the now classical formulation of Culick et al. [18-20]. As elaborated further in Section 2.1 and Appendix A, an inhomogeneous wave equation for the acoustic pressure p' may be derived in the form

$$\nabla^2 p' - \frac{1}{\bar{c}^2}\frac{\partial^2 p'}{\partial t^2} = h \tag{1a}$$

$$\boldsymbol{n} \cdot \nabla p' = -f \tag{1b}$$

The terms h and f contain all inhomogeneous terms accounting for unsteady gas dynamics, mean flow effects, combustion response, etc. The unsteady pressure and velocity fields are expanded in a generalized Fourier series in the chamber normal modes with unknown time-varying coefficients $\eta_n(t)$:

$$p' = \bar{p} \sum_{n=0}^{\infty} \eta_n(t) \psi_n(\boldsymbol{x}) \tag{2a}$$

$$u' = \sum_{n=0}^{\infty} \frac{1}{\bar{\gamma} k_n^2} \frac{d\eta_n}{dt} \nabla \psi_n(\boldsymbol{x}) \tag{2b}$$

where $k_n = \Omega_n / \bar{c}$ is the wave number, and the normal modes ψ_n satisfy the classical Helmholtz equation supplemented by an impermeability condition,

$$\nabla^2 \psi_n + k_n^2 \psi_n = 0 \tag{3a}$$

$$\boldsymbol{n} \cdot \nabla \psi_n = 0 \tag{3b}$$

It is to be noted that normal modes in three dimensions generally conform to a nomenclature involving three integral indices. However, because the modes may be considered as an infinite set ordered by increasing natural frequency, a single index n is sufficient to identify them unambiguously and is used here as shorthand.

A coupled system of ordinary differential equations governing the evolution of the modal amplitudes $\eta_n(t)$ can be derived by the application of a volume averaging procedure. Multiply the wave equation (1a) by ψ_n, the Helmholtz equation (3a) by p', and subtract the latter from the former. Then integrate the resulting moment over the control volume to produce

$$\iiint (\psi_n \nabla^2 p' - p' \nabla^2 \psi_n) dV - \frac{1}{\bar{c}^2} \iiint \psi_n \frac{\partial^2 p'}{\partial t^2} dV - k_n^2 \iiint p' \psi_n dV = \iiint \psi_n h \, dV$$

The first term on the left hand side can be transformed into a surface integral by an application of the divergence theorem. Then, upon introducing the boundary conditions from Eq. (1b) and Eq. (3b), we have

$$-\frac{1}{\bar{c}^2}\iiint \psi_n \frac{\partial^2 p'}{\partial t^2}\,dV - k_n^2 \iiint p'\psi_n dV = \iiint \psi_n h\,dV + \oiint \psi_n f\,dS \tag{4}$$

Now, substituting in the modal expansion for pressure (2a) and integrating termwise,

$$\sum_{m=0}^{\infty} \frac{d^2\eta_n}{dt^2}\left(\iiint \psi_n\psi_m\,dV\right) + \omega_n^2 \sum_{m=0}^{\infty} \eta_m(t)\left(\iiint \psi_n\psi_m\,dV\right)$$

$$= -\frac{\bar{c}^2}{\bar{p}}\left(\iiint \psi_n h\,dV + \oiint \psi_n f\,dS\right)$$

Furthermore, by orthogonality,

$$\iiint \psi_n\psi_m\,dV = E_n^2\delta_{nm}$$

where the Euclidean norm is given by

$$E_n^2 = \iiint \psi_n^2\,dV$$

and δ_{nm} denotes the Kronecker delta function. With this specification, only a single term survives in each of the infinite summations in the foregoing equation, leaving

$$\frac{d^2\eta_n}{dt^2} + \omega_n^2\eta_n = F_n \tag{5a}$$

$$F_n = -\frac{\bar{c}^2}{\bar{p}E_n^2}\left(\iiint \psi_n h\,dV + \oiint \psi_n f\,dS\right) \tag{5b}$$

Equations (5a) and (5b) form the basis for both a linear and a nonlinear analysis of combustion instabilities.

1.3.1. Linear Theory

If the nonlinear terms in acoustic pressure and velocity in the groups h and f are neglected, then ultimately one may derive expressions for frequency shifts and linear growth constants associated with each physical process. For example, damping constants associated with the exit nozzle, viscothermal damping of acoustic waves at solid boundaries, and damping due to suspended condensed particles may be written as [19]

$$\alpha_n^N = -\frac{\bar{c}}{2E_n^2} \iint\limits_{\text{nozzle}} \left(\text{Re}\left\{\frac{1}{Z_N}\right\} + M \right) \psi_n^2 \, dS \tag{6}$$

$$\alpha_n^v = -\frac{1}{2E_n^2}\sqrt{\frac{\omega_n \nu}{2}}\left[\frac{1}{k_n^2} \iint\limits_{\substack{\text{inert} \\ \text{surface}}} \|\nabla\psi_n - (\boldsymbol{n}\cdot\nabla\psi_n)\boldsymbol{n}\|^2 dS + \frac{\gamma-1}{\sqrt{\text{Pr}}} \iint\limits_{\substack{\text{inert} \\ \text{surface}}} \psi_n^2 \, dS\right] \tag{7}$$

$$\alpha_n^p = -\frac{1}{2}\frac{\sigma}{1+\sigma}\left[\frac{X_1(\omega_n)}{E_n^2} \iiint \left(\frac{\|\nabla\psi_n\|}{k_n}\right)^2 dV + (\gamma-1)\frac{C}{\bar{c}_p} X_2(\omega_n)\right] \tag{8}$$

where some slight modifications in notation have been made; additional details on the nomenclature can be found in the references. For combustion, one may similarly derive [11, 21],

$$\alpha_n^C = \frac{(\gamma-1)\omega_n}{2\pi\bar{p}E_n^2} \iiint \psi_n \, dV \int_t^{t+\tau_n} \eta_n \dot{Q}' \, dt \tag{9}$$

where $\dot{Q}'$ represents the fluctuating rate of heat release due to combustion, and τ_n is the period of the nth normal mode. Then the net linear growth rate of the mode is given simply as $\alpha_n = \alpha_n^C + \alpha_n^N + \alpha_n^v + \alpha_n^p + \cdots$

The representations (6)-(9) are physically illuminating, and have the advantage of providing information about the perturbed motions in terms only of the unperturbed mode shapes and natural frequencies. However, because they take the form of integrals of the chamber normal modes they cannot in general be evaluated in closed form. This is inconvenient for real combustors with a complex geometry and flowfield.

1.3.2. Nonlinear Theory

Retaining all terms in Eqs. (5a) and (5b) except those arising from unsteady heat release yields the system

$$\frac{d^2\eta_n}{dt^2} + \omega_n^2\eta_n = -\sum_{i=0}^{\infty}\left(D_{ni}\frac{d\eta_i}{dt} + E_{ni}\eta_i\right) - \sum_{i=0}^{\infty}\sum_{j=0}^{\infty}\left(A_{nij}\frac{d\eta_i}{dt}\frac{d\eta_j}{dt} + B_{nij}\eta_i\eta_j\right) \quad (10)$$

which includes additional linear modal coupling effects not included in the linear stability analysis, and where the coefficients can be written explicitly in terms of the chamber natural frequencies and mode shapes [22, 23]. Additional terms appear if unsteady combustion is considered, but these remain unclosed in that some response functions must still be specified [24]. Equation (10) represents an infinite system of coupled, nonlinear ordinary differential equations, each with an infinite number of terms. For real engines, only a few modes must be considered, but even under such simplification, an analytical solution to (10) remains elusive.

The most straightforward application of this analysis is to numerically integrate the appropriately truncated system in Eq. (10), given numerical values of the coefficients, to determine the entire time history of all the η_n in the presence of nonlinearities. This would reveal the presence of limit cycle oscillations, and provide a numerical estimate of their amplitudes. However, additional analytical progress can be achieved by employing a time averaging procedure. Suppose the solution for the n^{th} mode may be expressed in the following form

$$\eta_n(t) = r_n(t)\sin[\omega_n t + \phi_n(t)] \tag{11}$$

with a time varying amplitude and phase. In transforming the problem from one variable to two, an additional degree of freedom is introduced, and therefore a second constraint is required. This is chosen to be

$$\frac{d\eta_n}{dt} \equiv \omega_n r_n(t)\cos[\omega_n t + \phi_n(t)] \tag{12}$$

Introducing these forms into the system (10) leads to a first order system of nonlinear equations in the amplitude and phase:

$$\frac{dr_n}{dt} = \frac{1}{\omega_n} F_n(r_n, \phi_n)\cos(\omega_n t + \phi_n) \tag{13a}$$

$$\frac{d\phi_n}{dt} = -\frac{1}{\omega_n r_n} F_n(r_n, \phi_n)\sin(\omega_n t + \phi_n) \tag{13b}$$

The time averaging procedure is predicated on the existence of two widely separated time scales exhibited by this solution: a “fast” time scale, proportional to the period of oscillation, and a “slow” time scale, over which the functions r_n and ϕ_n gradually vary. In

view of this disparity, Eqs. (13a) and (13b) are integrated over a time interval τ in the fast variable (say a typical acoustic period), over which the amplitude and phase remain approximately constant. Then,

$$\frac{dr_n}{dt} \approx \frac{1}{\omega_n \tau} \int_t^{t+\tau} F_n(r_n, \phi_n) \cos(\omega_n t + \phi_n)\, dt \tag{14a}$$

$$\frac{d\phi_n}{dt} \approx -\frac{1}{\omega_n r_n \tau} \int_t^{t+\tau} F_n(r_n, \phi_n) \sin(\omega_n t + \phi_n)\, dt \tag{14b}$$

The averaging procedure eliminates all high-frequency components from the solution such that Eqs. (14a) and (14b) are considerably easier to numerically integrate than the system given by (10). More importantly, these equations facilitate a nonlinear stability analysis which may furnish closed form estimates for limit cycle amplitudes in terms of model parameters [23-25]. For example, Wicker et al. [25] used the averaging method above to analyze the dynamics of a two-mode system in a baffled combustor. The limit cycle amplitude for the first mode is found to be

$$r_1 = \sqrt{\frac{\alpha_1 \alpha_2}{a_1 b_1}\left[1 + \left(\frac{2\theta_1 - \theta_2 - \Omega_1}{2\alpha_1 + \alpha_2}\right)^2\right]}$$

where α_1 and α_2 denote the growth constants of the first and second tangential mode, and the other parameters are defined in the references. The group $a_1 b_1 < 0$ for the case considered which indicates that in order for the limit cycle to exist, it is also necessary that $\alpha_1 \alpha_2 < 0$. In other words, one mode must be stable and one must be unstable in order for a limit cycle to be attained. Numerical integration of the amplitude equations (14a,b) corroborate this conclusion, as shown below:

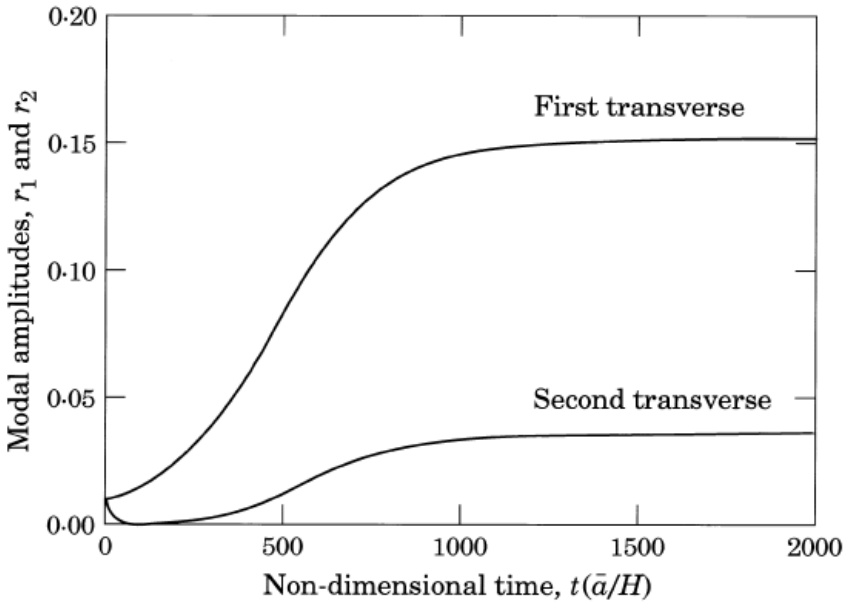

Fig. 8: Time histories of modal amplitudes of 1T and 2T modes in baffled combustion chamber. From [25].

From the plot it can be seen that indeed at early non-dimensional times the 1T mode grows while the 2T mode decays.

Except for the determination of accurate eigenmodes and natural frequencies, this nonlinear formulation is formally insensitive to the details of the chamber geometry. Additionally, higher order acoustic and combustion nonlinearities can be incorporated in a straightforward manner [26, 27], though the importance of such effects has not yet been conclusively established.

1.3.3. Combustion Response Modeling

The principal driver of acoustic oscillations in combustion chambers is the fluctuation in heat release rate due to flow forcing of the flame. Before they are useful for practical assessment of combustion chambers, the analyses discussed in the previous section – or any other formulation – must be supplemented with a model for this quantity in terms of acoustic parameters. Due to the complexity of turbulent combustion processes, this modeling task represents one of the key challenges in the development of an accurate stability analysis.

The nature of the combustion in any device is highly dependent on the geometric configuration of and the flowfield within the injectors. Because of the extremely large range of physical regimes in which combustion can take place, probably no completely general theoretical model for combustion response can be established. However, robust theoretical studies have emerged in recent years which help to explain and predict the nature of the heat release response under a variety of conditions.

Most progress has been made in the thin flamelet regime, in which the flame thickness is taken to be much smaller than the smallest hydrodynamic length scale. Under this hypothesis the flame may be idealized as an infinitely thin interface separating two regions of the flow. In the case of premixed flames, the interface is identified with the zero isocontour of a nonphysical field variable G. The field obeys a nonlinear convection-diffusion equation given by [28, 29]

$$\frac{\partial G}{\partial t} + \boldsymbol{u} \cdot \nabla G = s_L |\nabla G|$$

where s_L represents the laminar flame speed. Fleifil et al. [30] conducted one of the first analytical studies of premixed flame response to acoustic forcing by means of a linearized analysis of this equation. This formulation admits relatively simple incorporation of equivalence ratio perturbations [31-33], flame stretch effects [34, 35], and corrections for weak turbulence [36]. Most analyses have neglected gas expansion, and as such are rigorously valid only in the limit of vanishing density jump across the flame. Furthermore, additional studies are required as to the response of flames under arbitrarily strong turbulence, and with multiply connected topologies. Notwithstanding these limitations, this modeling approach yields good agreement with experimental observations in many cases.

Existing analysis for nonpremixed flames follows a similar strategy. The appropriate field variable in this case is the mixture fraction Z, defined as the ratio of mass originating from the fuel stream to the total mass at a given spatial location. It is governed by a linear convection diffusion equation [28, 29]

$$\frac{\partial Z}{\partial t} + \boldsymbol{u} \cdot \nabla Z = \mathcal{D}\nabla^2 Z$$

where $\mathcal{D}$ represents the mass diffusivity, which is assumed approximately equal for all species. In the classical Burke-Schumann limit of infinitely fast chemistry, the flame sheet is identified with the stoichiometric isosurface of the mixture fraction field. The linearity of the Z-equation renders it easier to solve than the G-equation, but its ellipticity complicates extraction of the spatiotemporal dynamics of the flame surface from the solution. Study of the forced response of nonpremixed flames is considerably less mature than that of premixed flames, however promising analysis in this direction has been undertaken [37-42], mostly in the context of laminar flames.

The most typical method of quantifying combustion response is the Flame Transfer Function (FTF) [43], defined as the ratio of the normalized heat release perturbation to the normalized flow perturbation, for example: $\mathcal{F}(\omega) = \left(\dot{Q}'/\bar{\dot{Q}}\right)/(p'/\bar{p})$. In the flamelet regime, analytical models have been developed based on the spatially integrated heat release utilizing the foregoing field equations which define the flame surface. Transfer functions have also been successfully measured experimentally and deduced from computational results. As with the analytical results many of these transfer functions, particularly from experimental measurements, are based on the spatially integrated heat release and are therefore global quantities for the system.

Fig. 9 shows the results for FTF magnitude based on the spatially integrated heat release axial-diffusion sensitive nonpremixed flames. The flame response exhibits strong low-pass filter behavior, especially in the limit of large Peclet number. This is typical of both premixed and nonpremixed flames, and tends to mean that low frequency modes are preferentially excited and are therefore the prime candidates for instability.

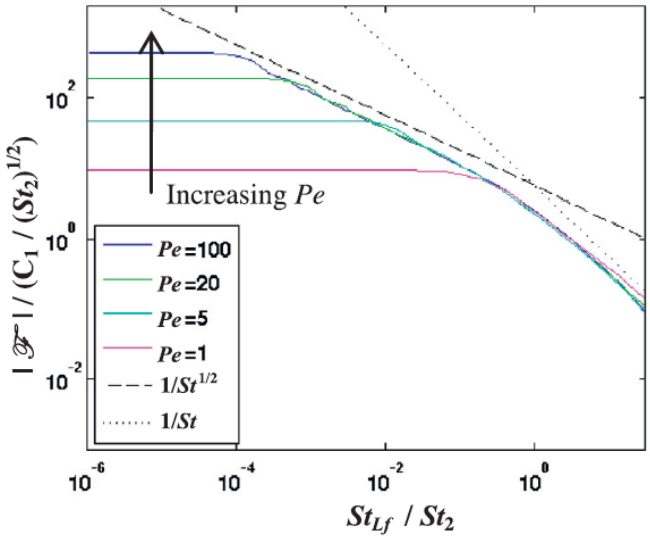

Fig. 9: FTF amplitude as a function of Strouhal number for different Peclet numbers. From Magina and Lieuwen [42].

In the ORSC engines considered in this thesis, a common injector configuration is the gas centered swirled coaxial (GCSC) injector. This design promotes a high rate of mixing, and improves flame stabilization through the generation of toroidal recirculation zones [44, 45]. In this configuration, a purely axial flow of oxidizer occupies the central passage, while a swirling fuel flow is introduced into an outer annulus via tangential passages. A nonpremixed jet flame is stabilized in the shear layer between the two streams and extends downstream for several injector diameters. The aforementioned work on nonpremixed flame dynamics is therefore of particular interest to the problem.

1.4. Numerical Analysis

On the other end of the spectrum are purely numerical treatments. The complete set of governing equations is solved over the domain, thus automatically accounting for all possible physics with minimal modeling. This remains an extremely computationally expensive task, to the extent that it may not be practical to run a sufficient number of cases during the design stage of an engine. A general strategy which has emerged to reduce the required resources is to numerically compute the acoustics of a chamber by solving some set of linearized perturbation equations, with all small scale processes affecting acoustic damping or driving being modeled either by theory or more detailed computations. Various particular methods may be found in the literature, including formulations based on the linearized Euler equations [46], acoustic perturbation equations [16], and the Helmholtz equation [47, 48].

Urbano et al. [49] present an analysis of a realistic model LRE combustor utilizing one such strategy. LES was first used to compute the reacting flowfield at several operating points. Time averaged distributions of density and speed of sound were used as inputs to a Helmholtz solver to investigate the acoustic field. In a follow up study, Urbano et al. [50] abandoned the reduced order acoustic solver and utilized LES alone to investigate the chamber acoustics and flame response. In both works, a postprocessing scheme was introduced in which the injector plane was partitioned by means of radial and azimuthal dividers into several cells, each containing a single flame. Unsteady heat release was integrated spatially over each cell and interaction with the acoustic pressure field was quantified by means of the Rayleigh index [51].

Although the purely computational approach may give considerably more accurate results for particular cases than the simplified theoretical treatments discussed in the previous sections, it leaves much of the underlying physics opaque. Thus as a tool to aid in the design of real engines, numerical analysis would best be utilized to complement, rather than to supplant, theoretical analysis.

1.5. Research Contributions and Dissertation Outline

This thesis proposes a consistent, high-fidelity strategy for predicting the linear stability of an oxidizer-rich staged combustion engine. An acoustic stability analysis is conducted using combustion response data from LES of appropriate injector configurations and a sensitivity analysis is conducted to identify controlling physics. The principle contributions are:

- Established a complete, consistent, linear stability analysis and applied it to a case study of a model engine which has a complex geometry and closely mimics a real ORSC engine.
- Incorporation of realistic chamber-level mean flow fields and distributed combustion response generated from LES of individual injectors. The effect of the injector design is investigated through simulations with three distinct injector recess lengths.
- A sensitivity analysis of a reduced set of scalar parameters characterizing the distributed combustion which demonstrate the controlling physics of the

combustion-acoustic interactions for acoustically and convectively noncompact flames.

CHAPTER 2.

Theoretical Formulation

2.1. Acoustic Wave Equation

The flow within a liquid rocket engine thrust chamber is complicated by the presence of multiple phases and chemical reactions. A brute force method of studying the flowfield would involve numerically solving the conservation equations for mass, momentum, energy, and chemical species in two phases. However this is an extremely expensive task which leaves much of the underlying physics opaque. A simplified two-phase formulation, due originally to Culick [18, 19], may be used instead. The conservation equations for mass, momentum, and energy incorporating a condensed phase are re-written to describe an equivalent single phase medium whose properties are mass-weighted averages of the original phases. Instead of solving the species transport equations with detailed chemical kinetics, the effect of chemistry may be incorporated as a global rate of heat release and rate of change of mean molecular weight. A single nonlinear acoustic wave equation may be extracted from this system, which incorporates all relevant physics as source terms:

$$\frac{1}{\bar{\rho}\bar{c}^2}\frac{\partial^2 p'}{\partial t^2} - \frac{1}{\bar{\rho}}\nabla^2 p' = -\mathcal{M} + \frac{1}{\bar{\rho}}\nabla\cdot\boldsymbol{\mathcal{D}} \tag{15}$$

where

$$\mathcal{M} = \frac{1}{\bar{\rho}\bar{c}^2}\left(\overline{\boldsymbol{u}}\cdot\nabla\frac{\partial p'}{\partial t} + \bar{\gamma}\frac{\partial p'}{\partial t}\nabla\cdot\overline{\boldsymbol{u}} + \frac{\partial(\boldsymbol{u}'\cdot\nabla p')}{\partial t} + \bar{\gamma}\frac{\partial(p'\nabla\cdot\boldsymbol{u}')}{\partial t} - \frac{\partial\mathcal{P}'}{\partial t}\right) \tag{16}$$

and

$$\boldsymbol{\mathcal{D}} = \bar{\rho}(\overline{\boldsymbol{u}} \cdot \nabla \boldsymbol{u}' + \boldsymbol{u}' \cdot \nabla \overline{\boldsymbol{u}}) + \left(\bar{\rho}\boldsymbol{u}' \cdot \nabla \boldsymbol{u}' + \rho' \frac{\partial \boldsymbol{u}'}{\partial t}\right) - \boldsymbol{\mathcal{F}}' \tag{17}$$

The boundary condition for Eq. (15), which replaces the classical von Nuemann condition, is

$$-\frac{1}{\bar{\rho}}(\boldsymbol{n} \cdot \nabla p') = \boldsymbol{n} \cdot \frac{\partial \boldsymbol{u}'}{\partial t} + \boldsymbol{n} \cdot (\overline{\boldsymbol{u}} \cdot \nabla \boldsymbol{u}' + \boldsymbol{u}' \cdot \nabla \overline{\boldsymbol{u}} + \boldsymbol{u}' \cdot \nabla \boldsymbol{u}') + \frac{1}{\bar{\rho}}\boldsymbol{n} \cdot \left(\rho' \frac{\partial \boldsymbol{u}'}{\partial t}\right) + \frac{1}{\bar{\rho}}\boldsymbol{n} \cdot \boldsymbol{\mathcal{F}}' \tag{18}$$

where $\boldsymbol{n}$ denotes a unit normal vector on the boundary oriented toward the interior of the domain. A derivation of these equations, including an explanation of the nomenclature, may be found in Appendix A. Note that approximating the fluctuating pressure and velocity fields as syntheses of the chamber acoustic modes would by definition fail to satisfy this condition.

The source terms have been separated into the groups (16) and (17) to emphasize the analogy of various flow inhomogeneities to classical acoustic sources. The purely scalar terms contained in $\mathcal{M}$ represent unsteady mass flux and are analogous to monopole sources. Likewise the purely vector terms in $\boldsymbol{\mathcal{D}}$ represent unsteady forces and correspond to dipole sources. In general there may also be second order tensor terms which physically represent fluctuating shear stresses due, for example, to turbulence. However these terms, analogous to quadrupole sources in classical acoustics, are neglected in this analysis. The efficiency of such sources is uniformly small for the frequency ranges of interest in LREs. The group $\mathcal{P}'$ represents contributions from chemical heat release and volumetric forces

and $\boldsymbol{\mathcal{F}}'$ represents various interphase momentum transfer processes (e.g., drag forces on liquid droplets).

Because the present analysis is concerned with linear stability, all second order terms in Eqs. (15) and (18) are discarded. Furthermore, we shall neglect the dipole flow contributions on the grounds that they account for acoustically compact regions of vorticity which are more appropriately modeled than resolved. Then, assuming all quantities vary harmonically as $e^{i\Omega t}$, the system reduces to

$$-\frac{1}{\bar{\rho}}\left(\frac{\Omega^2}{\bar{c}^2}\hat{p}+\nabla^2\hat{p}\right)=-\frac{i\Omega}{\bar{\rho}\bar{c}^2}\left(\overline{\boldsymbol{u}}\cdot\nabla\hat{p}+\bar{\gamma}\hat{p}\nabla\cdot\overline{\boldsymbol{u}}+\mathcal{P}'\right) \tag{19}$$

$$-\frac{1}{\bar{\rho}}(\boldsymbol{n}\cdot\nabla\hat{p})=i\Omega(\boldsymbol{n}\cdot\widehat{\boldsymbol{u}})+\boldsymbol{n}\cdot(\overline{\boldsymbol{u}}\cdot\nabla\widehat{\boldsymbol{u}}+\widehat{\boldsymbol{u}}\cdot\nabla\overline{\boldsymbol{u}}) \tag{20}$$

where we have also neglected the linear contributions from $\boldsymbol{\mathcal{F}}'$. Introducing the impedance $Z\equiv\hat{p}/(\boldsymbol{n}\cdot\widehat{\boldsymbol{u}})$, the boundary condition (18) may be expressed as

$$-\frac{1}{\bar{\rho}}(\boldsymbol{n}\cdot\nabla\hat{p})=\left(i\Omega+\overline{\boldsymbol{u}}\cdot\nabla+\boldsymbol{n}\cdot\nabla\overline{\boldsymbol{u}}\cdot\boldsymbol{n}\right)\frac{\hat{p}}{Z}$$

which is equivalent to the boundary condition of Myers [52]. In this form, it is capable of describing impedance surfaces over which there is an arbitrary spatially nonuniform slip velocity. Finally, in the absence of mean flow and heat release, the system reduces to

$$-\frac{1}{\bar{\rho}}\left(\frac{\Omega^2}{\bar{c}^2}\hat{p}+\nabla^2\hat{p}\right)=0 \tag{21}$$

$$-\frac{1}{\bar{\rho}}(\boldsymbol{n}\cdot\nabla\hat{p})=i\Omega\frac{\hat{p}}{Z} \tag{22}$$

As $Z \to \infty$, one recovers the classical Helmholtz equation for the normal modes of a chamber. Solving this system will produce the chamber's undamped eigenmodes. The natural frequencies may be used as nominal inputs to frequency-dependent submodels, which may in turn be applied to calculate the eigenmodes and complex eigenfrequencies $\Omega = \omega + i\alpha$ of the system in the presence of acoustic damping and driving modeled by Eq. (19). It is noted that according to the sign convention used here,

$$e^{i\Omega t} = e^{i(\omega + i\alpha)t} = e^{i\omega t}e^{-\alpha t}$$

Thus, a positive value of α indicates a damped wave, whereas a negative value indicates a driven wave. In the present work, all eigenvalue analyses are conducted using the finite element solver COMSOL.

2.2. Gas Properties

Evaluation of correct gas properties, particularly the speed of sound, is crucial to the success of any acoustic analysis. The RD-170 utilizes liquid RP-1 kerosene as fuel and gaseous oxygen as oxidizer in both the main combustion chamber and preburner. Kerosene is a mixture of various hydrocarbons with an overall ratio of hydrogen to carbon atoms of approximately 1.94. To simplify the chemical kinetics modeling, heptylcyclopentane ($C_{12}H_{24}$), a single-species surrogate fuel, is considered. Its thermodynamic properties closely approximate those of RP-1. The stoichiometric equation of this surrogate fuel with oxygen can be written as

$$C_{12}H_{24} + 18O_2 \rightarrow 12CO_2 + 12H_2O$$

From the reaction, the stoichiometric oxidizer-to-fuel ratio $(\mathrm{O/F})_{\mathrm{stoic}}$ is determined to be 3.43. The actual oxidizer-to-fuel ratio $(\mathrm{O/F})_{\mathrm{act}}$ is 52.311 in the preburner and 2.6 in the main combustion chamber. The equivalence ratio is defined as

$$\phi = \frac{(\mathrm{F/O})_{\mathrm{act}}}{(\mathrm{F/O})_{\mathrm{stoic}}} = \frac{(\mathrm{O/F})_{\mathrm{stoic}}}{(\mathrm{O/F})_{\mathrm{act}}}$$

Thus the equivalence ratio in the preburner is 0.0655 and that in the main chamber is 1.32. In a general fluid mixture, the speed of sound is computed by

$$\bar{c}^2 = \frac{c_p}{c_V}\left(\frac{\partial p}{\partial \rho}\right)_{T,Y_k}$$

where p and ρ are related by an appropriate real fluid equation of state [13, 14]. Likewise the constant pressure and constant volume specific heat capacities are computed for the given temperature from NASA polynomial fits.

2.2.1. Main Chamber and Oxidizer Dome Properties

The pressure within the main chamber is 245.5 bar, and that within the oxidizer dome is 270 bar. Under these conditions, the gas may still be considered as ideal and thus additional thermodynamic properties may be obtained through elementary thermodynamic relationships.

Table 1: Gas properties at chemical equilibrium conditions for RD-170 engine

Parameter	GOX Manifold	Main Chamber
O/F ratio	52.31	2.60
Equivalence ratio	0.066	1.32
Temperature, K	687.7	3676.1
Pressure, bar	270	245.5
Heat capacity ratio	1.33	1.2
Enthalpy, kJ/kg	-463.31	-1644.54
Entropy, kJ/kg·K	5.876	10.64
Constant pressure heat capacity, J/kg·K	1056.40	2035.65
Specific gas constant, J/kg·K	260.56	343.43
Molecular weight, g/mole	31.91	24.21
Density, kg/m^3	150.70	19.45
Sound speed, m/s	487.5	1231.9
Kinematic viscosity $\times 10^{-6}$, m^2/s	0.243	5.26
Thermal conductivity, W/m·K	0.048	0.290
Thermal diffusivity $\times 10^{-6}$, m^2/s	0.3	7.32

2.2.2. Preburner Properties

At 520 bar, the pressure in the preburner is nearly double that in the main chamber. At these conditions, the real gas behavior must be accounted for. The NIST REFPROP code is utilized to compute gas properties [53], which uses molecular data from the extensive NIST database and high fidelity explicit equations of state based on the Helmholtz free energy [54]. This model is known to exhibit better agreement with experimental data than typical cubic equations of state for several elementary hydrocarbon species. Fig. 10 shows a comparison between the calculated speeds of sound of the combustion products in the preburner and the corresponding values for an ideal gas at the same conditions.

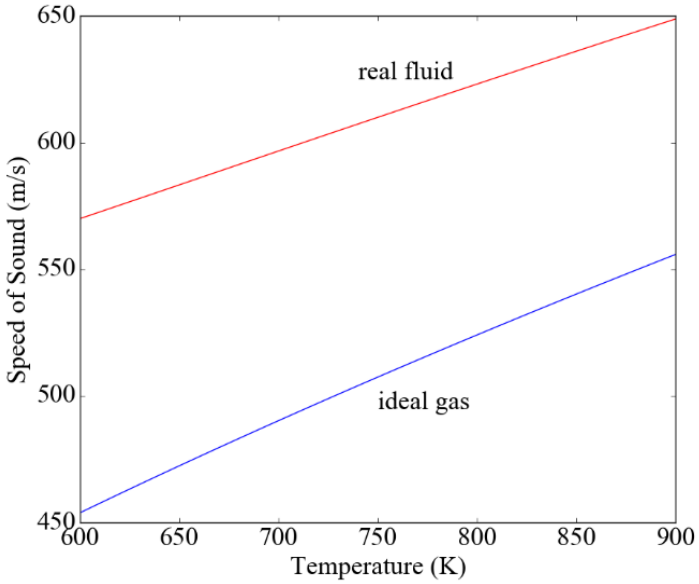

Fig. 10: Speeds of sound of ideal and real fluid for preburner combustion products at $\bar{p} = 520\ \text{bar}, \phi = 6.55 \times 10^{-2}$

The real-fluid speeds of sound nearly mirror the $\sim\sqrt{T}$ temperature dependence of the ideal gas speed of sound. However, reduction in compressibility due to intermolecular forces cause the speed of sound to be approximately 20% higher for the real-fluid versus the ideal gas over the entire temperature range investigated. It should be noted that the chemical composition of the mixture for these calculations was chosen by assuming complete combustion without product dissociation. The former assumption is justified by the extremely oxidizer rich environment in the preburner, and the latter by the high chamber pressure.

Combustion is initiated in the injector passage. The wide mixing passages and the bulk of the chamber are where the combustion products mix with the cold unburned

oxidizer, so as to allow the temperature and composition to become spatially uniform. The temperature in the injector passage is significantly higher than in the rest of the chamber. Table 2 lists the corresponding densities and speeds of sound populated in the model.

Table 2: Fluid properties for each subdomain computed from REFPROP

	Injection Element	Mixing Passage	Main Chamber
$\bar{\rho}$ (kg/m)	87.5	185	220
$\bar{c}$ (m/s)	903	660	619

2.3. Closing the Heat Release Term

The principal volumetric source of sound is the heat release due to combustion. Neglecting other volumetric sources we may express $\hat{\mathcal{P}} = (\bar{\gamma} - 1)\hat{\dot{Q}}$, where $\hat{\dot{Q}}$ is the spatial distribution of heat release at a certain frequency. This in turn must be expressed in terms of acoustic quantities to enable practical computations. The most common formulation in the linear regime is a closure involving a Flame Transfer Function (FTF). In general we may write

$$\frac{\hat{\dot{Q}}}{\bar{\dot{Q}}} = \mathcal{F}_p(\boldsymbol{r},\omega)\frac{\hat{p}}{\bar{p}} + \mathcal{F}_u(\boldsymbol{r},\omega)\frac{\hat{u}}{\bar{c}} + \mathcal{F}_v(\boldsymbol{r},\omega)\frac{\hat{v}}{\bar{c}} + \mathcal{F}_w(\boldsymbol{r},\omega)\frac{\hat{w}}{\bar{c}} + \mathcal{F}_\phi(\boldsymbol{r},\omega)\frac{\hat{\phi}}{\bar{\phi}} \quad (23)$$

with a complex-valued transfer function associated with each primitive variable. The speed of sound has been used as the reference for all velocity perturbations so as to make the

model formally valid at zero mean flow velocity. For the sake of generality these have been left as functions of both space and frequency.

We shall retain only the contributions from pressure perturbations so as to achieve the closure with the fewest derivatives. Expressing the FTFs in amplitude-phase form, and making the appropriate substitutions, Eq. (19) becomes

$$-\frac{1}{\bar{\rho}}\left(\frac{\Omega^2}{\bar{c}^2}\hat{p}+\nabla^2\hat{p}\right)=-\frac{i\Omega}{\bar{\rho}\bar{c}^2}(\bar{\boldsymbol{u}}\cdot\nabla\hat{p}+\bar{\gamma}\hat{p}\nabla\cdot\bar{\boldsymbol{u}})$$

$$+i\Omega\frac{\bar{\gamma}-1}{\bar{\rho}\bar{c}^2}\bar{\dot{Q}}n_p(\boldsymbol{r},\omega)e^{i\phi_p(r,\omega)}\frac{\hat{p}}{\bar{p}}$$

In addition to the time averaged velocity field, we now require at most the gains and phases of the pressure- and velocity-coupled Flame Transfer Functions.

Rather than extract transfer functions and flow fields for an entire chamber, suppose that we may extract such fields for only a single injector and construct chamber-level fields by superposition like so:

$$\begin{aligned}-\frac{1}{\bar{\rho}}\left(\frac{\Omega^2}{\bar{c}^2}\hat{p}+\nabla^2\hat{p}\right)&\\ =-\frac{i\Omega}{\bar{\rho}\bar{c}^2}\left[\nabla\hat{p}\cdot\sum_k\bar{\boldsymbol{u}}_k(\boldsymbol{r}-\boldsymbol{r}_k)+\bar{\gamma}\hat{p}\sum_k\nabla\cdot\bar{\boldsymbol{u}}_k(\boldsymbol{r}-\boldsymbol{r}_k)\right]&\\ +i\Omega\frac{\bar{\gamma}-1}{\bar{\rho}\bar{c}^2}\bar{\dot{Q}}\frac{\hat{p}}{\bar{p}}\sum_k n_{p,k}(\boldsymbol{r}-\boldsymbol{r}_k,\omega)e^{i\phi_{p,k}(r-r_k,\omega)}&\end{aligned}\tag{24}$$

where $\boldsymbol{r}_k$ represent the centerline coordinates of each injector in the chamber. Each of the fields $\bar{\boldsymbol{u}}_k, n_{p,k}, \phi_{p,k}$ have compact support only in the near field of a single injector. Computation of these quantities is discussed in more detail in Chapter 4.

CHAPTER 3.

Modeling of Damping Processes

Because the acoustic solver utilized for the eigenvalue study is strictly inviscid, any physical processes that would tend to damp acoustic waves must be modeled by means of impedance boundary conditions or user-specified source terms. The damping in all cases may ultimately be attributed to energy being transferred from the acoustic field to either the vortical or entropy field by the action of viscosity. Detailed models for particular processes in each component will be discussed in detail in the subsequent sections for both the main chamber assembly and preburner.

3.1. Main Chamber Assembly

In the main chamber assembly, as shown in Fig. 2 the two components which are expected to contribute most of the acoustic damping are the upstream flow distributor and the injectors themselves.

3.1.1. Flow Distributor Damping

The oxidizer manifold is terminated upstream by a flow distributor plate, which acts as a perforated acoustic liner with bias flow. It is known that liners damp acoustic energy and have found extensive use in a variety of combustion devices, particularly gas turbines. The mechanism of absorption may be described as follows. Incident acoustic

waves cause periodic shedding of vortices from the rims of the liner orifice. Some of the energy in the incident acoustic wave is reflected, some transmitted, and some appears as the kinetic energy of the vortices. If the vortices impinge on a downstream obstacle, they may excite additional acoustic waves. Otherwise, they will dissipate into incoherent turbulence and their energy will be permanently lost to the acoustic field. The magnitude of this damping is increased significantly in the presence of bias flow.

We shall employ the modeling approach of Hughes and Dowling [55], which rests on the theory of Howe [56] to describe the impedance of the distributor. Consider for the moment the flow distributor to be a plane interface between two gas regions, with the geometric properties shown in Fig. 11 below. A bias flow of average magnitude u_b traverses each orifice, the direction being immaterial.

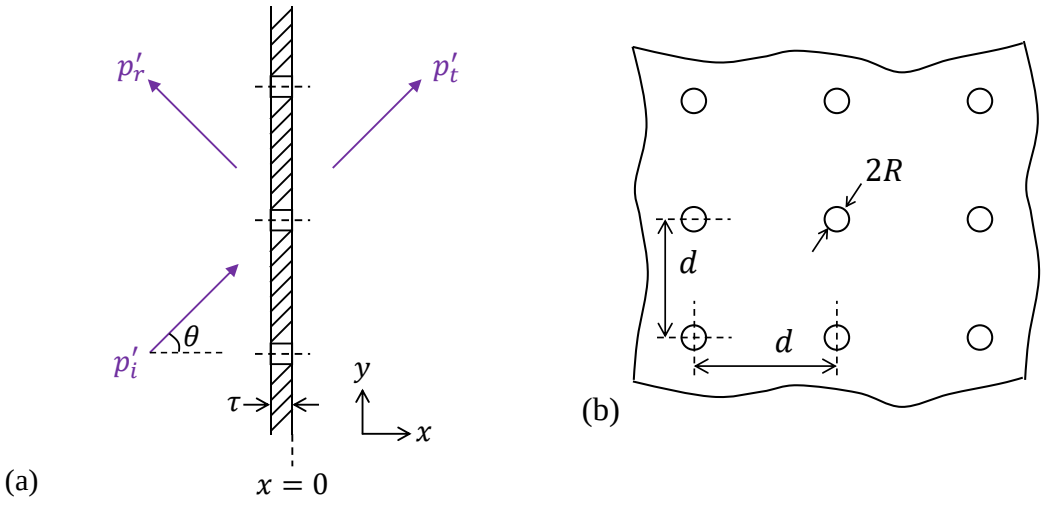

Fig. 11: Notional perforated liner with geometric parameters

Assume for the moment that in the near field of the plate all acoustic waves are plane. In the region $x < 0$, the acoustic pressure field is composed of a wave incident at some angle θ, and a reflected wave. In $x > 0$, there is only a transmitted wave:

$$p'_-(x,y,t) = \left(e^{-ik_1 x - ik_2 y} + \mathcal{R}e^{ik_1 x - ik_2 y}\right)e^{i\omega t}$$

$$p'_+(x,y,t) = \mathcal{T}e^{-ik_1 x - ik_2 y}e^{i\omega t}$$

where $k_1 = k\cos\theta$ and $k_2 = k\sin\theta$. We suppose that the inter-orifice separation d is smaller than a typical acoustic wavelength $(d/\lambda \ll 1)$, but large enough such that the shear layers of adjacent orifices do not interact $(d/R \gg 1)$. In this regime, the liner may be treated as a homogeneous compliant surface whose absorptive properties may be constructed from those of a single orifice. The fields must obey the following matching conditions at the plate [57]:

$$\left.\frac{\partial p'_-}{\partial x}\right|_{x=0} = \mathcal{N}\chi(p'_+ - p'_-)|_{x=0} \qquad \left.\frac{\partial p'_+}{\partial x}\right|_{x=0} = \mathcal{N}\chi(p'_+ - p'_-)|_{x=0}$$

where $\mathcal{N}$ is the number density of orifices on the plate, and χ is the Rayleigh conductivity of an orifice, defined as the ratio of fluctuating volume flux within an orifice to the applied unsteady pressure load. Enforcing these conditions on the model fields given above reveals

$$\mathcal{R} = \frac{k_1}{k_1 + 2i\mathcal{N}\chi}$$

where it should be noted that only the component of the incident wave normal to the screen participates in the reflection. This may be related to the impedance by

$$Z = \frac{1+\mathcal{R}}{1-\mathcal{R}\cos\theta}\frac{\bar{\rho}\bar{c}}{} \tag{25}$$

to yield

$$\frac{Z}{\bar{\rho}\bar{c}} = \frac{1}{\cos\theta} + \frac{kd^2}{i\chi} \tag{26}$$

where, for the square arrangement of orifices used in this example, the number density has been expressed as $\mathcal{N} = 1/d^2$. Various physical models may be developed for the Rayleigh conductivity [56, 58]. One such classical model due to Howe [56] produces a conductivity of the form $\chi = 2R(\gamma - i\delta)$ where the functions γ and δ depend on the orifice radius, bias flow velocity, and the frequency of the incident acoustic wave in the following way:

$$\gamma = \frac{I_1(k_bR)\left[1+\frac{1}{k_bR}\right] + \frac{4}{\pi^2}e^{2k_bR}\cosh(k_bR)\,K_1(k_bR)\left[\cosh(k_bR) - \frac{\sinh(k_bR)}{k_bR}\right]}{I_1(k_bR)^2 + \frac{4}{\pi^2}e^{2k_bR}\cosh^2(k_bR)\,K_1(k_bR)^2} \tag{27}$$

$$\delta = \frac{\frac{2}{\pi k_bR}I_1(k_bR)K_1(k_bR)e^{2k_bR}}{I_1(k_bR)^2 + \frac{4}{\pi^2}e^{2k_bR}\cosh^2(k_bR)\,K_1(k_bR)^2} \tag{28}$$

where I_1 and K_1 denote modified Bessel functions of order 1 of the first and second kind, respectively, and $k_b = \omega/u_b$ is a convective wave number. The linearized theory which produces these expressions is predicated on the assumption of a high Reynolds number bias flow. In this case, the flowfield may be approximated as inviscid in every region except within an infinitely thin cylindrical vortex sheet shed from the orifice rim. The functions γ and δ are plotted in Fig. 12 below.

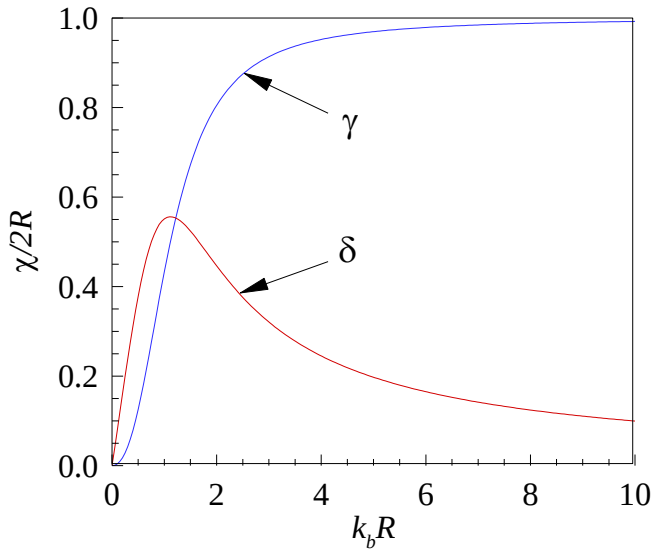

Fig. 12: Real and imaginary parts of Rayleigh conductivity as a function of Helmholtz number

Note the behavior in the two important limits $k_bR \to 0$ and $k_bR \to \infty$. In the former case, which corresponds either to low frequency or high bias flow velocity, the conductivity approaches zero and so the liner approximates an acoustically rigid boundary. On the other hand in the high k_bR limit, which corresponds either to high frequency or low bias flow velocity, $\chi \to 2R$ as expected from classical potential theory.

3.1.2. Injector Damping

For simplicity, the presence of any liquid film within the injectors is ignored, and the volume is assumed to be filled entirely with gaseous oxidizer. The two principle acoustic damping mechanisms are (1) viscous damping of acoustic waves and (2) energy

transfer from the acoustic to the vortical mode at inlet and outlet orifices. The relative importance of these mechanisms may be estimated in terms of the Strouhal number $\mathrm{St}_\omega = \omega R/\hat{u}$, where $\hat{u}$ is the amplitude of the acoustic velocity and R is the injector radius [59]. If $\mathrm{St}_\omega \gg 1$, viscous dissipation dominates the damping.

An equivalent impedance can be derived for the injection surface by taking into account viscous dissipation. For a wave incident at an angle θ, we have

$$\frac{Z}{\bar{\rho}\bar{c}} = e^{i\pi/4}\sqrt{\frac{\bar{c}^2}{\omega\nu}}\left(\sin^2\theta + \frac{\bar{\gamma}-1}{\sqrt{\mathrm{Pr}}}\right)^{-1} \tag{29}$$

The factor $e^{i\pi/4} = (1+i)/\sqrt{2}$ indicates that both the real and imaginary parts of the impedance are the same, and the phase is a constant. Thus the amplitude may simply be taken as either $\sqrt{2}\mathrm{Re}\{Z\}$ or $\sqrt{2}\mathrm{Im}\{Z\}$. For the gas properties presented in Table 1, Fig. 13 shows the frequency variation of the temperature.

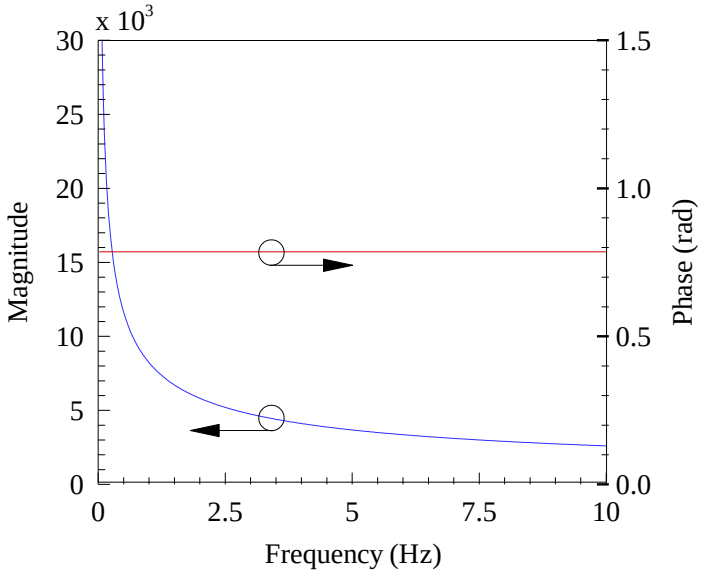

Fig. 13: Equivalent impedance of acoustic boundary layer $Z/\bar{\rho}\bar{c}$ as seen by plane waves at grazing incidence

The impedance remains high for the entire frequency range of concern, and in particular $|Z| \to \infty$ as $f \to 0$. In the presence of viscous dissipation within the acoustic boundary layer, a variational analysis incorporating Eq. (27) shows that the wave number for the quasi-plane waves propagating in a duct of radius R can be expressed as

$$k_v = \frac{\omega}{\bar{c}} + \frac{e^{-i\pi/4}}{R}\sqrt{\frac{\omega\nu}{\bar{c}^2}}\left(1 + \frac{\bar{\gamma} - 1}{\sqrt{\mathrm{Pr}}}\right) \tag{30}$$

These results are valid provided the acoustic boundary layer remains laminar. At high Reynolds numbers additional damping may arise due to turbulence penetrating the acoustic boundary layer [60, 61], and in that case corrected damping models should be employed.

We define a complex speed of sound $\bar{c}_v \equiv \omega/k_v$, and a complex density $\rho_v \equiv k_v Z/\omega$. Utilize these gas properties in the computation accounts indirectly for the presence of viscous damping, and circumvents the numerical difficulties of direct application of Eq. (27) to the injection surface.

3.2. Preburner Assembly

As shown in Fig. 4, the products of combustion from the preburners enter the turbine inlet hub and flow through an annular passage leading to the turbine blades. The model is truncated at this plane, and must be supplied with an appropriate impedance condition. The problem of transmission through blade rows was first addressed in the study by Kaji and Okazaki [62, 63], in which the effects of mean-flow Mach number, blade spacing, and relative angle between the blades and the flow were quantified as a function of wave number. Muir [64] generalized the analysis to allow for a three-dimensional acoustic field and nontrivial blade camber. Back propagating acoustic waves can also be generated due to the acceleration of nonisentropic density or temperature fluctuations (known collectively as entropy waves) as well as vorticity waves, through the rotor-stator assembly [65]. Cumpsty and Marble [66] used a quasi one-dimensional theory to determine the reflected pressure wave in such a scenario at low frequencies. Recently, high-fidelity techniques such as Large Eddy Simulation (LES) has been employed to explore this mechanism from the perspective of combustion noise and elucidate in more detail the effect of blade geometry [67].

In the present investigation the turbine blade row, as shown in Fig. 5, has a hub-to-tip ratio that is small in comparison with the average turbine radius. Therefore we may employ the thin annulus approximation and neglect higher order three dimensional acoustic motions in the derivation of blade row impedance. Thus we may make use of the quasi-1D results of [62]. Consider such a blade row that has been unrolled and interacts with locally plane acoustic waves, as shown below in Fig. 14.

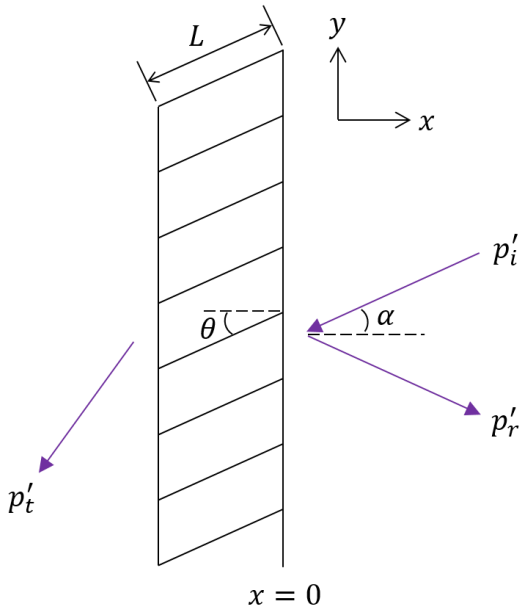

Fig. 14: Acoustic interaction with blade row. Incident, reflected, and transmitted waves denoted respectively by p_i', p_r' and p_t'.

The blade chord length is denoted by L and θ denotes the blade angle with respect to the horizontal. The wave incident on the blade row at some angle α is partially reflected and partially transmitted. We express the pressure fields in the upstream (p'_-) and downstream (p'_+) regions of the blade row as a superposition of plane waves:

$$p'_+(x,y,t) = p'_i(x,y,t) + \mathcal{R}p'_r(x,y,t) \tag{31}$$

$$p'_-(x,y,t) = \mathcal{T}p'_t(x,y,t) \tag{32}$$

where $\mathcal{R}$ and $\mathcal{T}$ denote the reflection and transmission coefficients. Matching the fields across the blade row by means of the linearized conservation equations yields expressions for these quantities. The impedance may again be written in terms of the reflection coefficient according to the relation (25). Assuming time harmonic variation with frequency ω and wave number $k = \omega/\bar{c}$, we have ultimately

$$\frac{Z}{\bar{\rho}\bar{c}} = \frac{1}{\cos\alpha}\left[2\sqrt{1 + \frac{\sin^2 kL}{4}\left(\frac{\cos\theta}{\cos\alpha} - \frac{\cos\alpha}{\cos\theta}\right)^2} - 1\right] \tag{33}$$

Fig. 15 shows example calculations for both the reflection coefficient and impedance for a fixed blade angle of attack θ and several different angles of wave incidence α. For a nominal blade chord length of 0.08 m, the wavenumber covers a frequency range of 0-3870 Hz.

Equation (33) reveals some important special cases that are of interest to designers. For all angles of incidence, the reflection coefficient is maximized at $kL = \pi/2$, when the blade chord length is equal to one quarter of the acoustic wavelength. Likewise it vanishes at $kL = \pi$, when the blade chord length is equal to one half of the acoustic wavelength because there is no phase difference between the incident and transmitted wave. The latter case presents an attractive rule of thumb. It must not, however, be regarded as a rigorous quantitative criterion because the waves incident on the turbine blade row are not perfectly planar, and because multiple wavelengths are likely to be represented in the acoustic field. Furthermore, it should be emphasized that these impedance values correspond to the case

of negligible mean flow, in which the effects of vorticity and entropy waves are not considered.

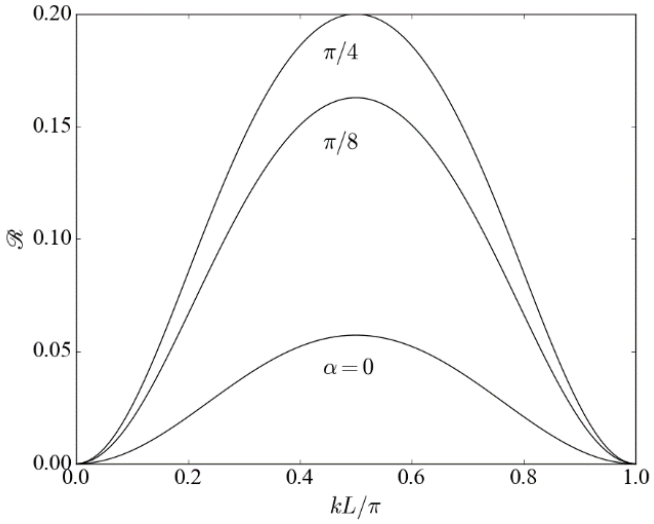

(a)

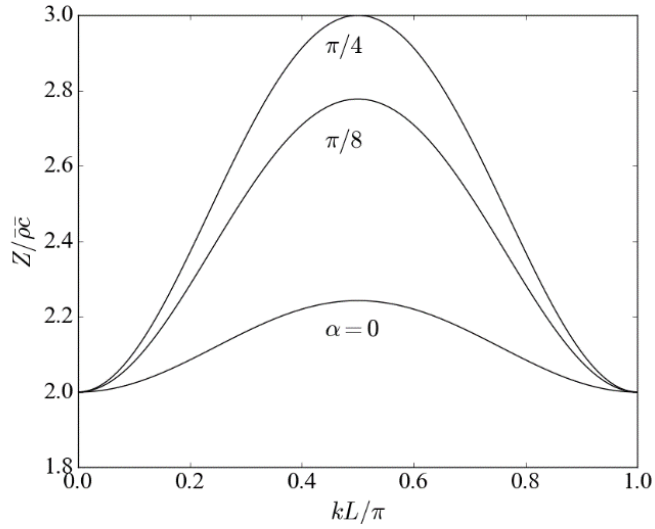

(b)

Fig. 15: (a) Reflection coefficient and (b) impedance of turbine blade row. Angle of attack fixed at $\theta = 60°$

To incorporate this impedance boundary condition into the acoustic model, the local incidence angle of waves at the boundary must be related to the acoustic velocities via $\tan\alpha = \hat{u}_y/\hat{u}_x$.

CHAPTER 4.

Combustion Response Modeling and Sensitivity Analysis

The most important submodel for a useful acoustic stability analysis is that for the response of the combustion process to unsteady flow motions. This aspect of the problem has consistently proven to be the most difficult, and is likely a main source of uncertainty in instability models. A principal reason for this is the intrinsic complexity of turbulent combustion processes. For the Reynolds numbers encountered in typical LREs, a wide range of length and time scales are represented in the flowfield and in the flame itself. Accurately accounting for these, as well as the chemical processes involved in the heat release is a particularly complex task. Another reason is the fact that combustion response models may be highly sensitive to system specific parameters such as injector geometry. Taken together, these facts make the development of a combustion response model which is generally applicable, even to a restricted class of system such as LREs, highly unlikely. Response functions must be determined specifically for a given system to ensure quantitative accuracy.

The engines of interest in this thesis utilize gas centered swirl coaxial (GCSC) type injectors. Fig. 6 schematically shows the configuration of this system. The inner core consists of non-swirling oxidizer from an upstream manifold. An outer annulus of swirling fuel is injected and traverses the length of an oxidizer post before meeting with the oxidizer stream. Upon settling out of ignition transients, a swirling turbulent nonpremixed flame is established in the injector cup. It is stabilized in the small recirculation region directly

adjacent to the oxidizer post tip. The dynamic response of nonpremixed flames has received comparatively less attention than that for premixed flames, but some theoretical and numerical investigations have been performed which provide a valuable starting point.

4.1. Mean Velocity Fields

The complex three dimensional injector flowfields are characterized by an in-house LES code [45, 68, 69]. Fig. 16 shows a schematic view of the injector configuration based on the RD-170 injectors in Fig. 6a which is used in LES.

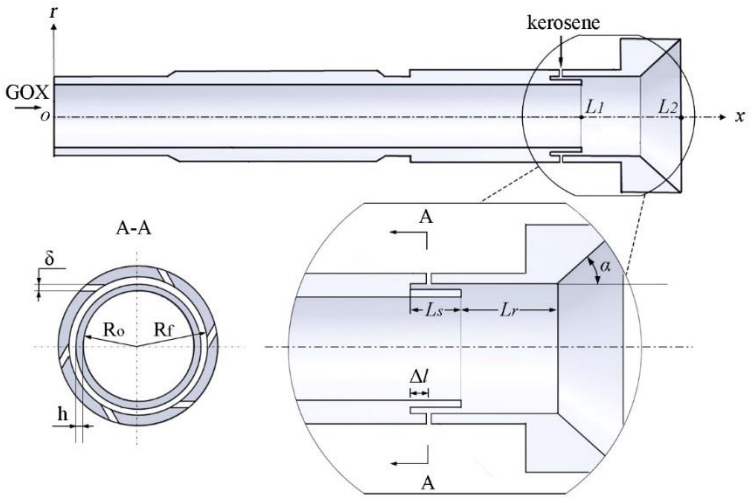

Fig. 16: GCSC injector diagram

Table 3: GCSC injector dimensions

Fuel inlet diameter δ (mm)	0.66
Shield thickness h (mm)	5.76
Inner annular radius R_o (mm)	5.62
Outer annular radius R_f (mm)	7.03
Inlet to shield tip length L_1 (mm)	93
Shield tip to injector outlet L_2 (mm)	113.1
Shield length L_s (mm)	5.5
Recess length L_r (mm)	10.5
Axial location of fuel injection port Δl (mm)	2
Spreading angle α	42°

Fig. 17 shows snapshots of the temperature field from LES for three different fuel shield lengths. It can be seen that the recess length has a noticeable effect on the flowfield, mainly through its alteration of the recirculation zone on the fuel-side.

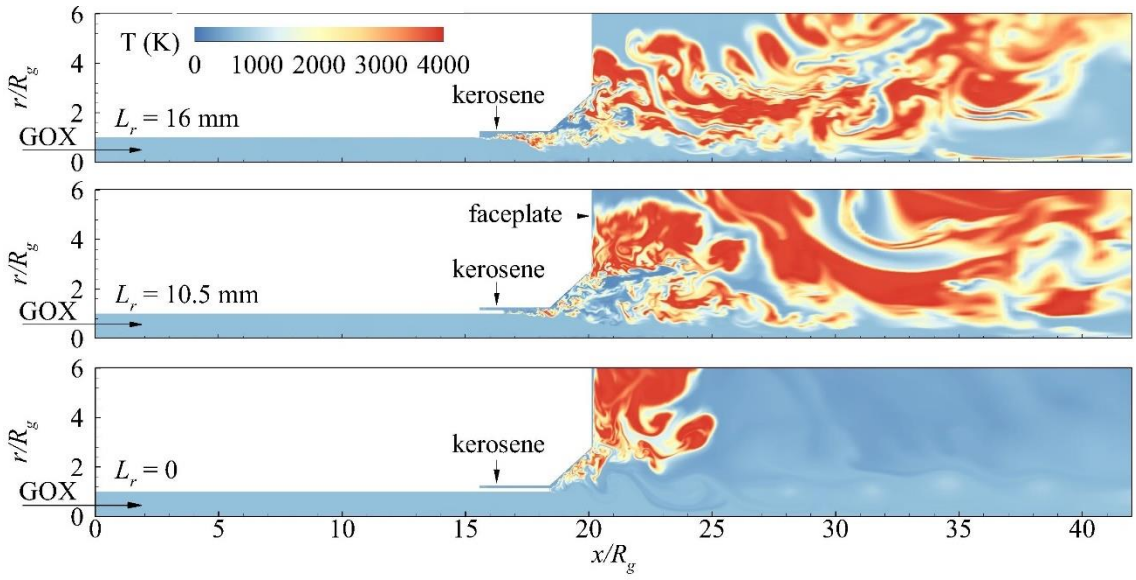

Fig. 17: Temperature field for reacting flow with (a) full recess (b) intermediate recess (c) no recess. From [68]

The first two source terms on the right hand side of Eq. (24) shows that the background flow may affect the acoustic motions in two primary ways: convection and refraction. The effect of uniform mean flow on acoustic propagation in ducts has been well studied, and its effects are primarily convective. Cutoff frequencies are lowered in the presence of mean flow, thus at a given frequency of oscillation more modes are potentially cut-on than without flow. When the velocity field is spatially varying, refraction also occurs whereby wavefronts are distorted by virtue of being convected at different velocities at different points in space. Fig. 18 shows the distributions of time-averaged velocity components downstream of the injector. The fields for the three injector recesses are similar to the extent that only those for one recess length (intermediate) are used to illustrate the difference in stability between uniform and nonuniform flow.

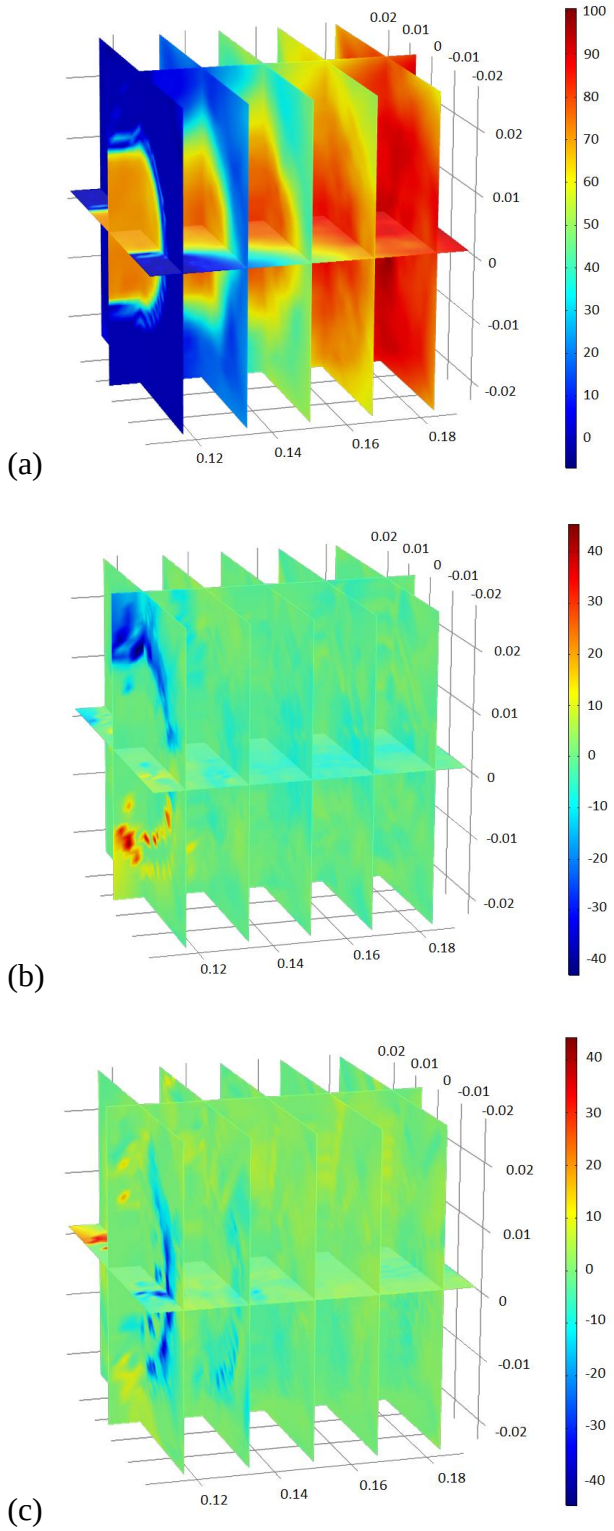

Fig. 18: Time averaged velocity fields from LES (a) u-velocity (b) v-velocity (c) w-velocity

The swirl is evidenced in the v- and w- velocity plots in Fig. 18b and c. The strength of the swirl is strongest in the near field of the exit plane and quickly diminishes downstream, whereas the axial velocity increases. Both of these effects are attributable to the gas expansion associated with combustion.

4.2. Combustion Response Functions

In order to determine the combustion response first the heat release must be computed from the primitive LES variables. By means of the unsteady flamelet equation, the reaction rate for the kth species may be expressed

$$\widetilde{\dot{\omega}}_k = \tilde{\rho}\frac{\partial \tilde{Y}_k}{\partial t} - \tilde{\rho}\mathcal{D}\left|\nabla \tilde{Z}\right|^2 \frac{\partial^2 \tilde{Y}_k}{\partial \tilde{Z}^2} \tag{34}$$

where $\mathcal{D}, Y_k$ and Z denote respectively the mass diffusivity, species mass fractions, and the tilde denotes Favre-averaging. Then the heat release is computed from the reaction rates and enthalpies of formation as

$$\tilde{\dot{Q}} = \sum_{k=1}^{N} \widetilde{\dot{\omega}}_k h_k^0 \tag{35}$$

The Favre-averaged heat release along with the corresponding flow variables are assumed to contain all the necessary unsteady information for the construction of the combustion response fields.

Numerically-based system identification (SI) methodology has been applied to LES data, and the extracted FTF was then utilized within a network model to characterize the intrinsic thermoacoustic instability. This approach was further improved to model the noise

and forego the necessity for external excitation of the system. Parametric SI based on the Box-Jenkins model was employed in lieu of Wiener-Hopf and modeled the noise along with the acoustic transfer matrices. This study found that the same noise model was captured for both the LES simulation with and without external acoustic excitation, increasing confidence that the transfer function correctly represents the physical mechanisms driving combustion instability.

Proper Orthogonal Decomposition (POD) [70, 71], which is known in other contexts as Karhunen-Loeve decomposition [72] or principle component analysis (PCA), is a well-established technique for data reduction and feature extraction. For a given flow variable $f(\boldsymbol{r}, t)$, the POD analysis can determine a set of orthogonal functions φ_j, such that the projection of f onto the first n functions,

$$\hat{f}(\boldsymbol{r}, t) = \bar{f}(\boldsymbol{r}) + \sum_{j=1}^{n} a_j(t)\varphi_j(\boldsymbol{r}) \tag{36}$$

minimizes the error, defined as $E\left(\left\|f - \hat{f}\right\|^2\right)$. Here $a_j(t)$ represents the temporal variation of the jth mode, and $E(\cdot)$ and $\|\cdot\|$ denote respectively the time average and L^2 norm. The mode shapes φ_j are ordered in such a way that the lowest modes have the highest energy as defined by the inner product on f.

From a statistical standpoint, the objective of a data-driven relationship between unsteady release and flowfield variables relies on correlation data analysis. A typical approach is to use the cross-correlation and autocorrelation information to obtain the relationship, which can be incorporated into the classical $n - \tau$ model for a single time lag. This can be interpreted physically as a representation of a single dominant physical

process that governs the gain of unsteady head release. In order to generalize this relationship for multiple time lags, as it is evident that the combustion process has a range of relevant time scales, the following statistical transfer function model can be utilized for quantifying the effect of velocity on unsteady heat release:

$$\dot{Q}'_j(t) = \sum_{k=1}^{K_p} \sum_{\tau=0}^{K_\tau} \beta_{k\to j}(\tau) p'_k(t-\tau) + \epsilon_j(t), \qquad j = 1, \dots, K_{\dot{Q}} \tag{37}$$

where $\dot{Q}'_j(t)$ and $u'_j(t)$ are the time-varying coefficients of the jth mode of $\dot{Q}$ and p, up to a maximum of $K_{\dot{Q}}$ and K_p modes, respectively. The symbol $\beta_{k\to j}(\tau)$ is the transfer weight from the kth mode of u to the jth of $\dot{Q}$, at a time lag of τ up to a maximum of K_τ time lags, and $\epsilon_j(t)$ are zero-mean noise process. As a statistical model, the formulation in the previous equation can be viewed as a large-scale, coupled system of sparse Box-Jenkins transfer models with multiple inputs [73]. The additional details are provided in Ref. [74].

Physically, the pressure and heat release from the LES have some spectral content which is characterized by their POD modes, and Eq. (37) can be viewed as selecting out the response at the appropriate frequencies. The responses shown in Fig. 19 and Fig. 20 are thus the response fields at only the nominal 1T and 2T frequencies.

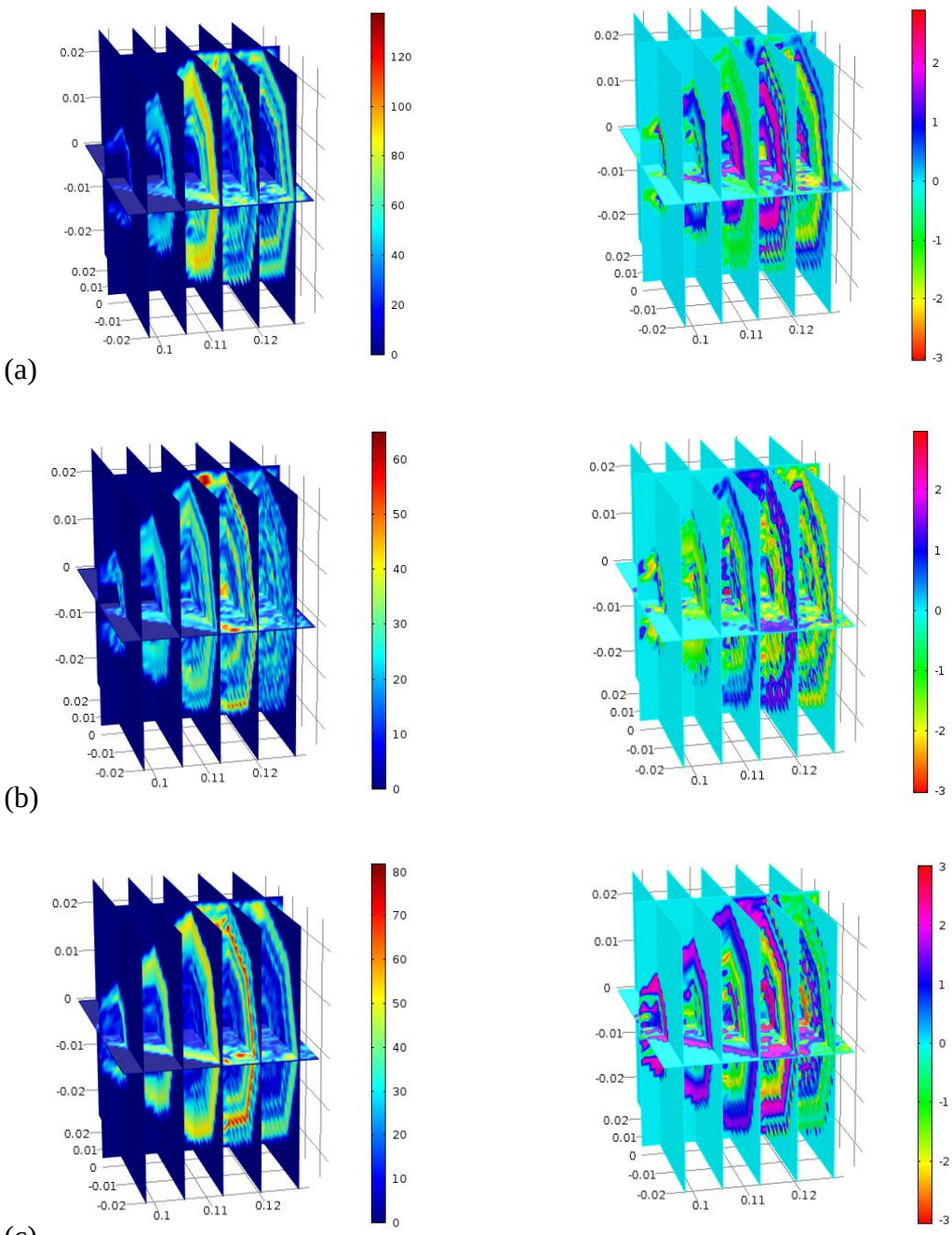

Fig. 19: FTF gain (left) and phase (right) at 1T frequency. (a) no recess (b) intermediate recess (c) full recess

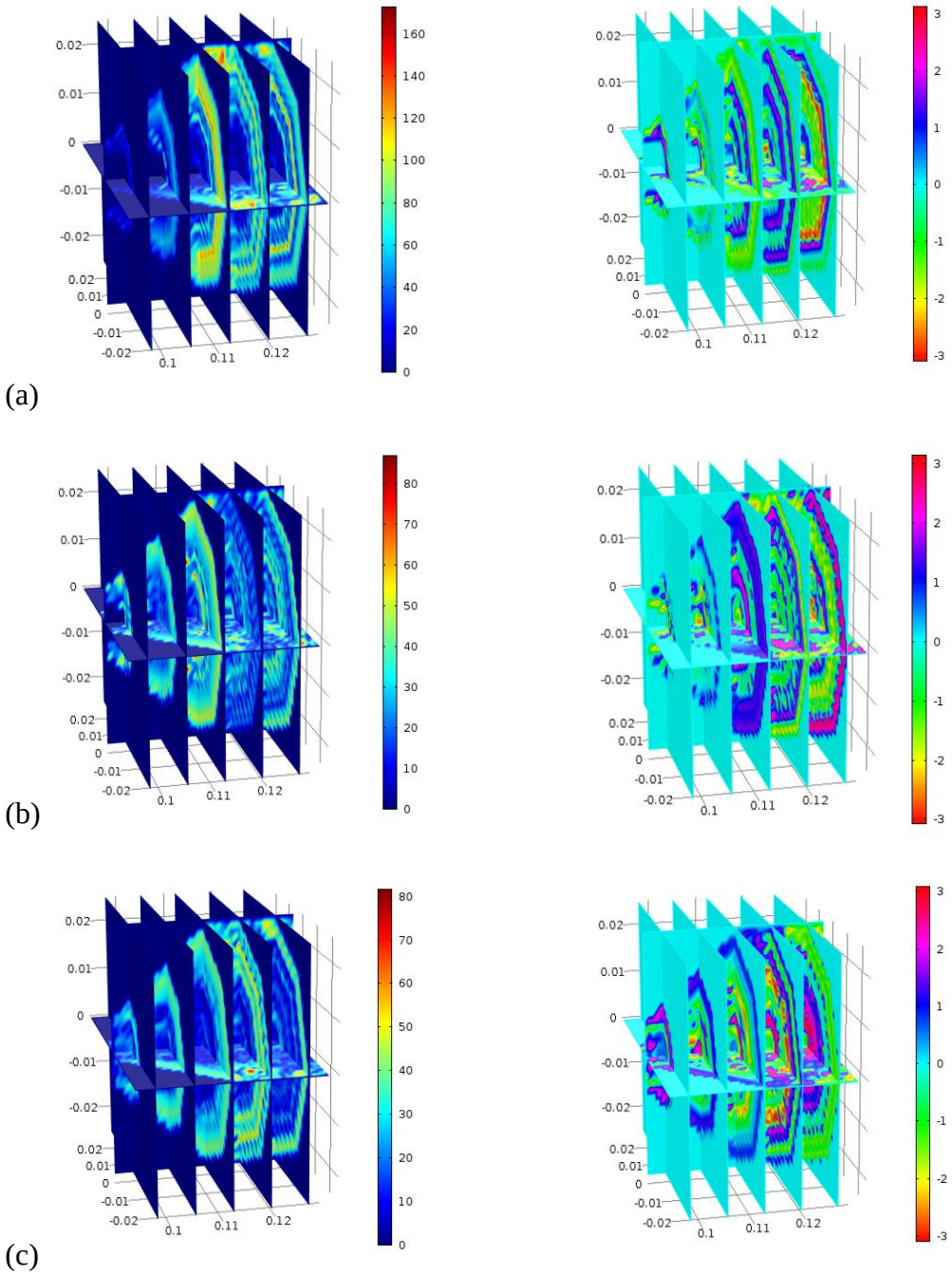

Fig. 20: FTF gain (left) and phase (right) for 2T mode. (a) no recess (b) intermediate recess (c) full recess

Finally it should be noted that the use of a pressure-coupled, rather than a velocity-coupled transfer function is a possibly significant approximation. Physically, it is known that in general flame response is primarily kinematic in nature. The principle driver of heat release oscillations is fluctuating velocity which wrinkles the flame front and modulates its area. This means that the most rigorous method of capturing the flame response physics would involve the deduction of three separate flame transfer functions coupled to each of the three fluctuating velocity components. Additionally, velocity coupled responses would cause terms involving the gradient of the acoustic pressure to arise in the wave equation. These two issues: the large volume of input data coupled with the form of the acoustic source term, greatly complicate convergence of the model.

In utilizing the pressure-coupled response, we have thus made a significant assumption – that the response field accounts *implicitly* for all of the flame response arising from unsteady motions. In other words, we assume that the pressure fluctuations and the velocity fluctuations are closely correlated. This assumption may be violated, however, in cases where the pressure-velocity relationship (in the form of the linearized momentum equation) takes significantly different forms for different acoustic modes. Further work is needed to fully clarify this issue.

4.3. Sensitivity Analysis

The level of detail made available by the combustion response extracted from LES is generous; however, there is still significant uncertainty associated with the Flame Transfer Function used in the acoustic analysis. This is likely to be the most significant

source of error for the acoustic eigenvalues and mode shapes, and a robust quantification of the sensitivities to FTF parameters must be undertaken. Adjoint analysis [75-77] has recently seen application in the sensitivity analysis and uncertainty quantification in parametric studies of thermoacoustic systems, having been adapted from earlier use in hydrodynamics [78].

In previous studies, the extremely simplified models utilized for FTF facilitated the sensitivity analysis as well as the acoustic stability analysis. The spatially integrated combustion response functions that they employ may be characterized by as few as two scalar parameters – namely the gain and phase – which constitute a two-dimensional input space. If we consider a single acoustic mode at a time, the frequency and growth rate likewise constitute a two-dimensional output space. An immediate difficulty arises when generalizing to a spatially distributed heat release. Considering that the gain and phase may take on values at any point in the continuum, the initial space becomes in principle infinite-dimensional. For a sensitivity analysis of this new system to be intelligible, a (small) finite sent of parameters which characterizes the field must first be chosen.

For the gain field we choose these to represent the strength of the response as well as the extent of its non-compactness. First, we take the average value of the gain over the entire field n_{avg}. We shall also consider the maximum value, as well as the coordinates at which it occurs: $n_{\max}, \left(x_{n_{\max}}, r_{n_{\max}}\right)$. As a measure of the noncompactness of the flame we also consider the axial "spread" of the gain about the maximum value, $\Delta x_{n_{\max}}$ which we define as the distance between the axial locations upstream and downstream of $n_{\max}$ at which the field attains the average value.

We shall also consider quantities which represent how quickly the phase changes in space over the axial direction; in particular, the axial derivative of the phase at the x-location of the maximum gain, as well as the average of the axial phase slope over the entire field. Values for these quantities evaluated from the fields shown in Fig. 19 and Fig. 20 are displayed in the table below.

Table 4: Combustion response field properties

	1T			2T		
	No Recess	Medium Recess	Full Recess	No Recess	Medium Recess	Full Recess
n_{avg}	20.5	18.5	19.3	23.6	19.6	20.1
$n_{\max}$	118	65	81.1	150	86.2	81.7
$x_{n_{\max}}$ (cm)	11.6	11.5	12	11.8	10.8	11.6
$r_{n_{\max}}$ (cm)	2.1	2.2	1.82	2.2	1.1	2.0
$\Delta x_{n_{\max}}$ (cm)	0.7	0.6	0.65	0.56	0.61	0.49
$\frac{\partial \phi}{\partial x}\Big\|_{\text{avg}} \left(\frac{\text{rad}}{\text{cm}}\right)$	-0.13	-0.09	-0.10	-0.13	-0.11	-0.12
$\frac{\partial \phi}{\partial x}\Big\|_{n_{\max}} \left(\frac{\text{rad}}{\text{cm}}\right)$	-0.11	-0.26	-0.21	-0.16	-0.25	-0.27

The sensitivity analysis relies on the Discrete Adjoint (DA) method which will be reviewed in this section; the development will follow that of Magri et al [76]. We combine the wave equation with combustion response (24) and the impedance boundary condition (22) and recast in operator notation:

$$[\mathcal{A} + \mathcal{B}(\Omega, \boldsymbol{q}) - \mathcal{G}(\Omega, \boldsymbol{q})]\hat{p} + \Omega^2\hat{p} = 0 \tag{38}$$

where the vector $\boldsymbol{q}$ contains all the system parameters including those associated with the boundary conditions, geometry, and flame response. For the current study, this will consist only of the FTF parameters. The operators in (33) are given by

$$\mathcal{A} = \bar{c}^2\nabla^2$$

$$\mathcal{B} = \boldsymbol{n} \cdot \nabla + \frac{i\bar{\rho}\Omega}{Z}$$

$$\mathcal{G} = \frac{\bar{\gamma} - 1}{\bar{\rho}\bar{c}}\bar{\dot{Q}}\sum_k n_{p,k}^{\omega}(\boldsymbol{r} - \boldsymbol{r}_k)e^{i\phi_{p,k}^{\omega}(\boldsymbol{r}-\boldsymbol{r}_k)}$$

More compactly,

$$\mathcal{N}(\Omega, \boldsymbol{q})\hat{p} = 0 \tag{39}$$

where the inhomogeneous Helmholtz operator is $\mathcal{N}(\Omega, \boldsymbol{q}) = \mathcal{A} + \mathcal{B}(\Omega, \boldsymbol{q}) - \mathcal{G}(\Omega, \boldsymbol{q}) + \Omega^2$. We consider perturbations in the system parameters of the form $\boldsymbol{q} = \boldsymbol{q}_0 + \epsilon\boldsymbol{q}_1$ where ϵ is a small numerical parameter. The acoustic eigenfrequencies and eigenfunctions are likewise perturbed; to second order in perturbation amplitude, Taylor expansion reveals

$$\Omega(\boldsymbol{q}_0 + \epsilon\boldsymbol{q}_1) \approx \Omega(\boldsymbol{q}_0) + \left.\frac{\partial\Omega}{\partial\boldsymbol{q}}\right|_0 \epsilon + \frac{1}{2}\left.\frac{\partial^2\Omega}{\partial\boldsymbol{q}^2}\right|_0 \epsilon^2 \equiv \Omega_0 + \epsilon\Omega_1 + \epsilon^2\Omega_2$$

$$\hat{p}(\boldsymbol{q}_0 + \epsilon\boldsymbol{q}_1) \approx \hat{p}(\boldsymbol{q}_0) + \left.\frac{\partial\hat{p}}{\partial\boldsymbol{q}}\right|_0 \epsilon + \frac{1}{2}\left.\frac{\partial^2\hat{p}}{\partial\boldsymbol{q}^2}\right|_0 \epsilon^2 \equiv \hat{p}_0 + \epsilon\hat{p}_1 + \epsilon^2\hat{p}_2$$

where in the last equalities we have defined the first and second order perturbations to Ω and $\hat{p}$. The eigenvalue problem in the absence of perturbations is simply

$$\mathcal{N}(\Omega_0, \boldsymbol{q}_0)\hat{p}_0 = 0 \tag{40}$$

where $\hat{p}_0$ is the undisturbed eigenfunctions. The theory of adjoint sensitivity relies heavily on the existence of the so-called adjoint eigenfunction $\hat{p}_0^\dagger$ which is found as the solution to the dual problem to (40):

$$\mathcal{N}(\Omega_0, \boldsymbol{q}_0)^{\mathrm{H}}\hat{p}_0^\dagger = \left(\hat{p}_0^\dagger\right)^{\mathrm{H}}\mathcal{N}(\Omega_0, \boldsymbol{q}_0) = 0 \tag{41}$$

where $(\cdot)^{\mathrm{H}}$ denotes the complex transpose ("Hermitian") operator. Introducing the perturbation expansions into the problem (41) we have

$$\mathcal{N}(\Omega_0 + \epsilon\Omega_1 + \epsilon^2\Omega_2, \boldsymbol{q}_0 + \epsilon\boldsymbol{q}_1)(\hat{p}_0 + \epsilon\hat{p}_1 + \epsilon^2\hat{p}_2) = 0$$

Expanding the operator out reveals the first order $\mathcal{O}(\epsilon)$ perturbation problem is

$$\mathcal{N}(\Omega_0, \boldsymbol{q}_0)\hat{p}_1 + \left.\frac{\partial\mathcal{N}}{\partial\Omega}\right|_0 \Omega_1\hat{p}_0 + \left.\frac{\partial\mathcal{N}}{\partial\boldsymbol{q}}\right|_0 \boldsymbol{q}_1\hat{p}_0 = 0 \tag{42}$$

And likewise for the second order $\mathcal{O}(\epsilon^2)$ perturbation problem:

$$\begin{aligned}\mathcal{N}(\Omega_0, \boldsymbol{q}_0)\hat{p}_2 + \left.\frac{\partial\mathcal{N}}{\partial\Omega}\right|_0 \Omega_1\hat{p}_1 + \left.\frac{\partial\mathcal{N}}{\partial\Omega}\right|_0 \Omega_2\hat{p}_0 + \left.\frac{\partial\mathcal{N}}{\partial\boldsymbol{q}}\right|_0 \boldsymbol{q}_1\hat{p}_1 + \frac{1}{2}\left.\frac{\partial^2\mathcal{N}}{\partial\Omega^2}\right|_0 \Omega_1^2\hat{p}_0 \\ + \left.\frac{\partial^2\mathcal{N}}{\partial\Omega\partial\boldsymbol{q}}\right|_0 \boldsymbol{q}_1\Omega_1\hat{p}_0 + \frac{1}{2}\left.\frac{\partial^2\mathcal{N}}{\partial\boldsymbol{q}^2}\right|_0 \boldsymbol{q}_1^2\hat{p}_0 = 0\end{aligned} \tag{43}$$

The first and second order eigenfrequency perturbations can be extracted by multiplying the foregoing equations by $\left(\hat{p}_0^\dagger\right)^{\mathrm{H}}$ and applying the adjoint property (41):

$$\Omega_1 = -\frac{1}{P_0}\left(\hat{p}_0^\dagger\right)^{\mathrm{H}}\left.\frac{\partial\mathcal{N}}{\partial\boldsymbol{q}}\right|_0 \boldsymbol{q}_1\hat{p}_0 \tag{44}$$

and

$$\Omega_2 = -\frac{\left(\hat{p}_0^{\dagger}\right)^{\mathrm{H}}}{P_0}\left[\left.\frac{\partial \mathcal{N}}{\partial \Omega}\right|_0 \Omega_1 \hat{p}_1 + \left.\frac{\partial \mathcal{N}}{\partial \boldsymbol{q}}\right|_0 \boldsymbol{q}_1 \hat{p}_1 + \frac{1}{2}\left.\frac{\partial^2 \mathcal{N}}{\partial \Omega^2}\right|_0 \Omega_1^2 \hat{p}_0 \right.$$

$$\left. + \left.\frac{\partial^2 \mathcal{N}}{\partial \Omega \partial \boldsymbol{q}}\right|_0 \boldsymbol{q}_1 \Omega_1 \hat{p}_0 + \frac{1}{2}\left.\frac{\partial^2 \mathcal{N}}{\partial \boldsymbol{q}^2}\right|_0 \boldsymbol{q}_1^2 \hat{p}_0\right] \tag{45}$$

where for brevity we have defined

$$P_0 \equiv \left(\hat{p}_0^{\dagger}\right)^{\mathrm{H}} \left.\frac{\partial \mathcal{N}}{\partial \Omega}\right|_0 \hat{p}_0$$

With these formulas, the frequency and growth rate perturbations are then given simply by

$$\omega_1 = \mathrm{Re}\{\Omega_1\} \qquad \alpha_1 = \mathrm{Im}\{\Omega_1\} \qquad \omega_2 = \mathrm{Re}\{\Omega_2\} \qquad \alpha_2 = \mathrm{Im}\{\Omega_2\}$$

according to the sign convention outlined in Section 2.1. The operator partial derivatives must be approximated by finite differences as follows, where δ is a small numerical parameter:

$$\left.\frac{\partial \mathcal{N}}{\partial \boldsymbol{q}}\right|_0 \boldsymbol{q}_1 \approx \mathcal{N}(\Omega_0, \boldsymbol{q}_0 + \epsilon \boldsymbol{q}_1) - \mathcal{N}(\Omega_0, \boldsymbol{q}_0)$$

$$\left.\frac{\partial \mathcal{N}}{\partial \Omega}\right|_0 \approx \frac{\mathcal{N}\big((1+\delta)\Omega_0, \boldsymbol{q}_0\big) - \mathcal{N}(\Omega_0, \boldsymbol{q}_0)}{\delta}$$

$$\left.\frac{\partial^2 \mathcal{N}}{\partial \boldsymbol{q}^2}\right|_0 \boldsymbol{q}_1^2 \approx \mathcal{N}(\Omega_0, \boldsymbol{q}_0 + 2\epsilon \boldsymbol{q}_1) - 2\mathcal{N}(\Omega_0, \boldsymbol{q}_0 + \epsilon \boldsymbol{q}_1) + \mathcal{N}(\Omega_0, \boldsymbol{q}_0)$$

$$\left.\frac{\partial^2 \mathcal{N}}{\partial \Omega^2}\right|_0 \approx \frac{\mathcal{N}\big((1+2\delta)\Omega_0, \boldsymbol{q}_0\big) - 2\mathcal{N}\big((1+\delta)\Omega_0, \boldsymbol{q}_0\big) + \mathcal{N}(\Omega_0, \boldsymbol{q}_0)}{\delta^2}$$

$$\left.\frac{\partial^2 \mathcal{N}}{\partial \Omega \partial \boldsymbol{q}}\right|_0 \boldsymbol{q}_1$$

$$\approx \frac{\mathcal{N}\big((1+\delta)\Omega_0, \boldsymbol{q}_0 + \epsilon \boldsymbol{q}_1\big) - \mathcal{N}\big((1+\delta)\Omega_0, \boldsymbol{q}_0\big) - \mathcal{N}(\Omega_0, \boldsymbol{q}_0 + \epsilon \boldsymbol{q}_1) + \mathcal{N}(\Omega_0, \boldsymbol{q}_0)}{\delta}$$

CHAPTER 5.

Results for RD-170 Model

In this chapter results for the ORSC engine design modeled on the Russian RD-170 are reviewed and analyzed. The acoustic fields and stability results for both the main chamber and preburner are computed separately.

5.1. Main Chamber Model

The geometry for the main chamber is displayed in Fig. 2 and consists of the combustion chamber itself coupled by the injector manifold to the upstream oxidizer dome. It is terminated downstream by a surface representing the throat-cross section of the exit nozzle. The mean flow at the throat attains sonic velocity such that no acoustic signals from further downstream in the nozzle can affect the oscillations in the main chamber.

A grid independence study is conducted to ensure convergence of the results. The geometry is discretized by a nonconforming tetrahedral mesh with the element growth rate (i.e. the maximum allowable percentage difference in volume for adjacent elements) capped at 40%. The refinement is done by fixing the minimum element size at 2 mm, and reducing the maximum allowed element size progressively. Table 5 shows the element sizes and corresponding total tetrahedral mesh elements, and Fig. 21 shows external views of the meshes. For the refinement study, only the baffled configuration is utilized.

Table 5: Mesh characteristics of refinement levels used for mesh independence study

	Level 1	Level 2	Level 3
Max. element size (mm)	50	30	10
Number of elements	2,814,003	2,824,858	3,621,150

Table 6 shows the eigenvalue results for the 1T and 2T modes for the different grid resolutions. The results indicate an extremely marginal change in frequency results with grid refinement. Modal distributions of pressure and velocity also show no discernable change and are not shown here; all figures showing modal distributions in subsequent sections are representative of the results. This is attributable to the fact that a typical acoustic wavelength in the main chamber covers several element diameters in the coarsest mesh. The refinement study indicates that we may choose the coarsest resolution to minimize simulation time, while not significantly affecting the results.

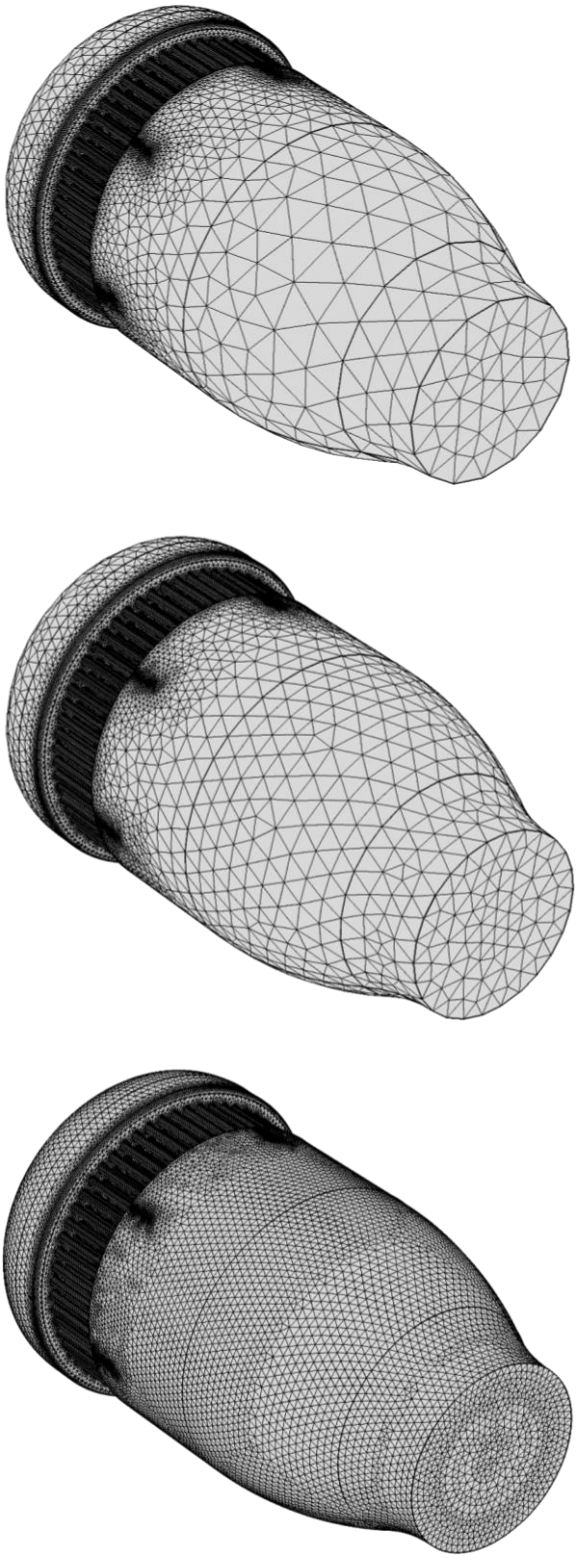

(a)

(b)

(c)

Fig. 21: Grids used for grid independence study (a) normal (b) fine (c) finest

Table 6: Eigenvalue results for grid sensitivity

	Level 1	Level 2	Level 3
1T	1881	1880	1880
2T	3152	3152	3151.5

5.1.1. Eigenvalue Analysis

As a baseline, the normal acoustic mode shapes and frequencies of the main combustion chamber are determined by an eigenvalue analysis of the system (21) and (22) with rigid boundaries ($Z \to \infty$). The first tangential (1T) and second tangential (2T) modes are known to dominate, and so are the focus of the present results. Fig. 22-Fig. 28 show results for these modes, for both baffled and unbaffled injectors. Because the amplitudes in a linear analysis are arbitrary, in all figures the pressure and velocity amplitudes have been suitably normalized to unity. The calculated natural frequencies are listed in Table 7.

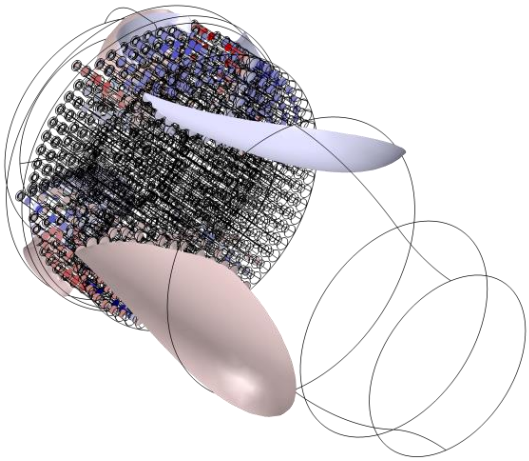

(a)

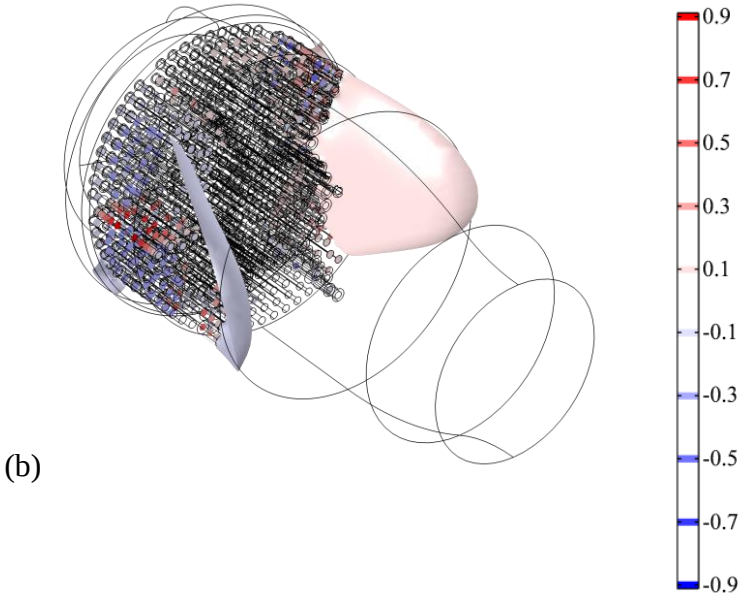

(b)

Fig. 22: Pressure isosurfaces for the 1T mode in (a) unbaffled and (b) baffled configurations

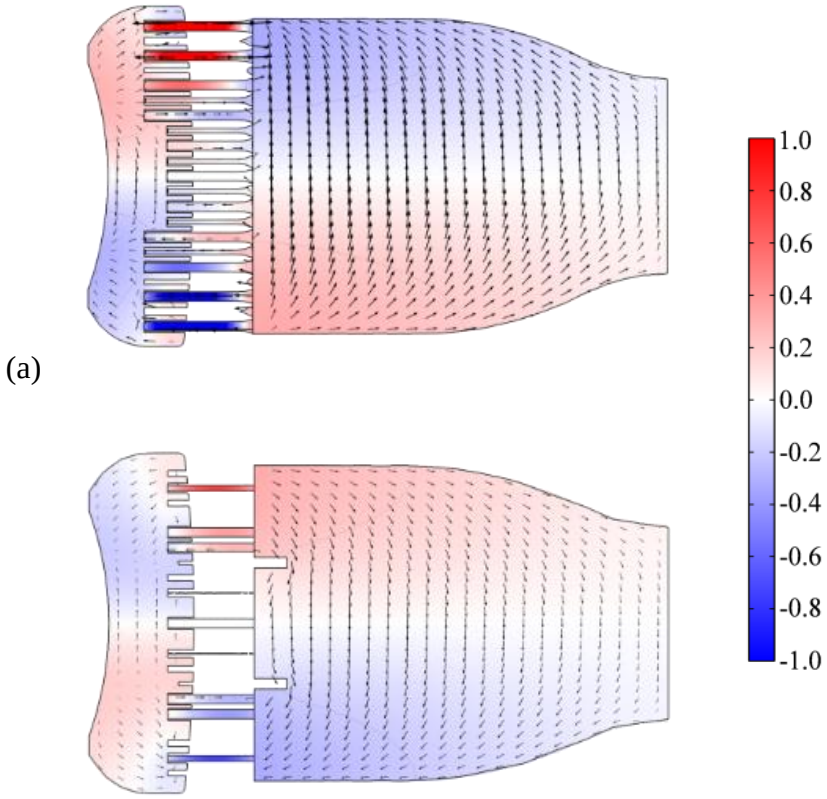

(a)

(b)

Fig. 23: Pressure and velocity fields for 1T mode at 0° longitudinal cross section (a) unbaffled and (b) baffled configuration

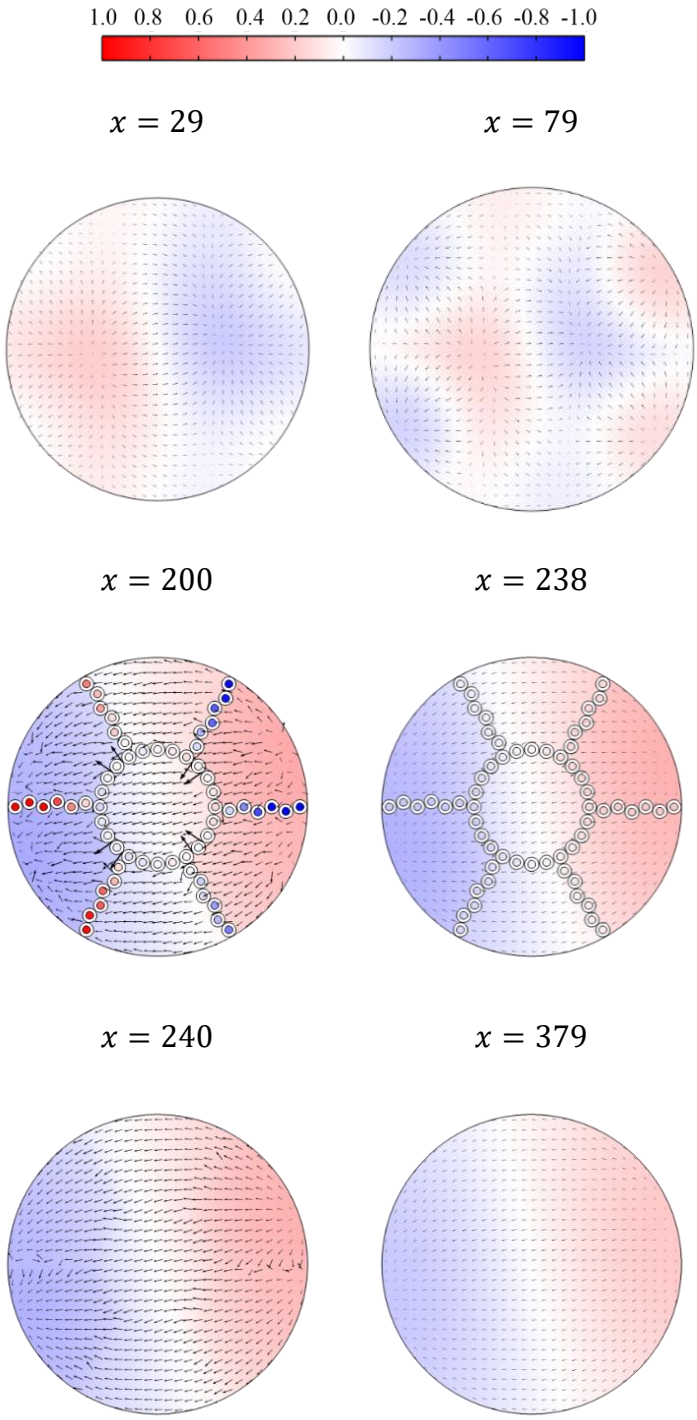

Fig. 24: Axial cross sections of pressure and velocity fields for first tantential (1T) mode for baffled configuration (all dimensions in mm)

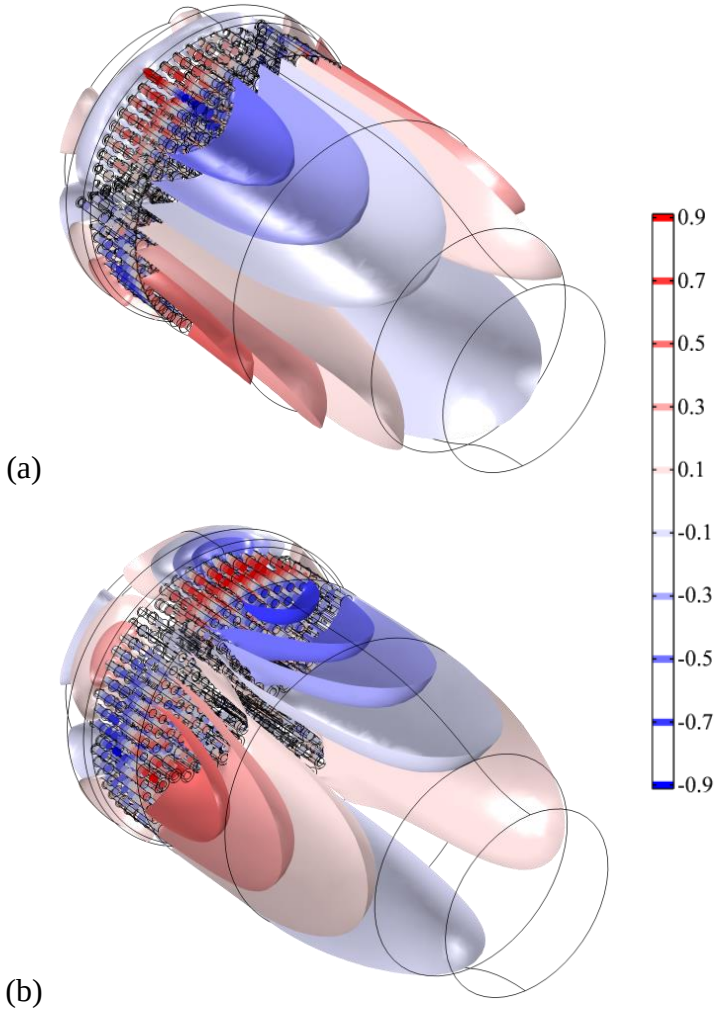

Fig. 25: Pressure isosurfaces for second tangential (2T) mode in (a) unbaffled and (b) baffled configuration

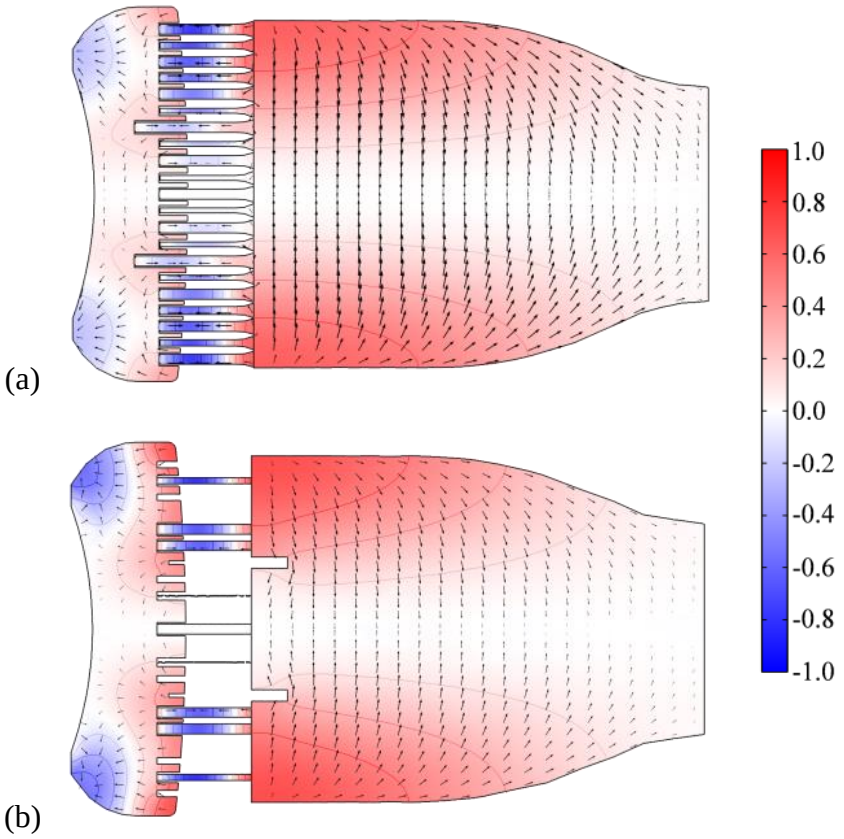

Fig. 26: Pressure and velocity fields of second tangential (2T) mode at 0° longitudinal cross section in (a) unbaffled and (b) baffled configuration

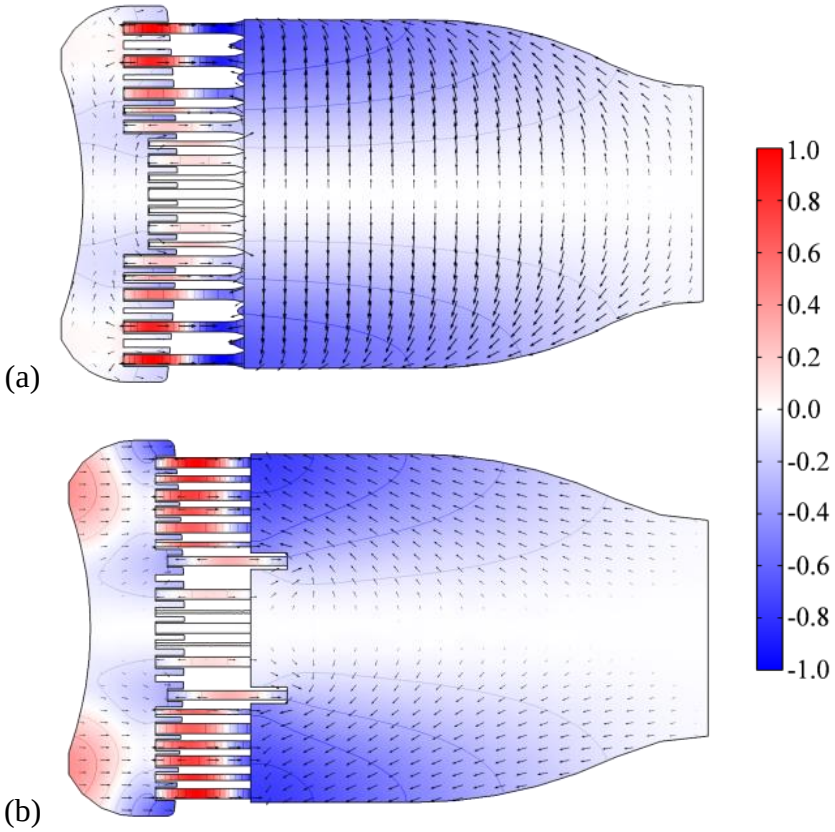

Fig. 27: Pressure and velocity fields of second tangential (2T) mode at 90° longitudinal cross section in (a) unbaffled and (b) baffled configuration

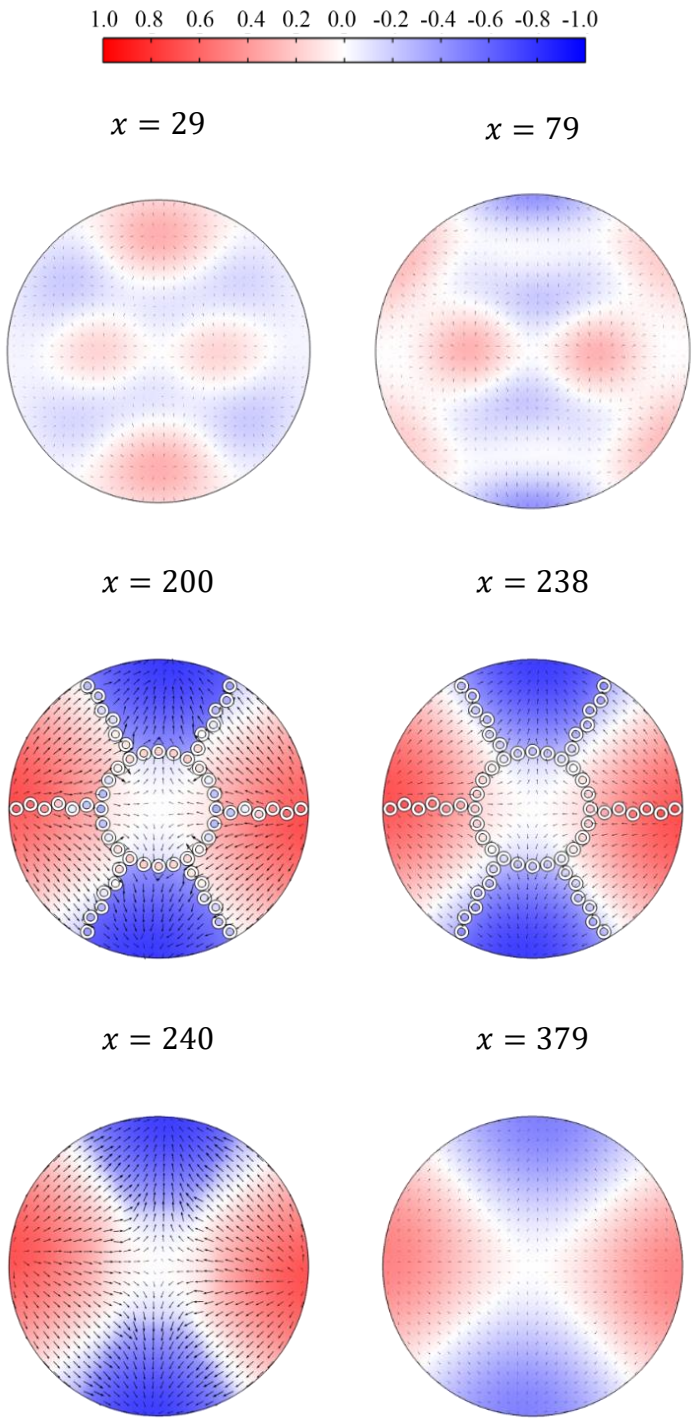

Fig. 28: Axial cross sections of pressure and velocity fields for second tangential (2T) modes (all dimensions in mm)

Table 7: Normal frequencies (Hz) of RD-170 main combustion chamber

Mode	Unbaffled	Baffled
1T	1908	1881
2T	3217	3152

The addition of baffles slightly decreases the frequency of oscillation, a result consistent with findings from previous studies. For the chamber and injection geometries considered here, the approximate formula of Dranovky et al. [7] predicts a decrease of about 1% in the natural frequency with the addition of baffles, in reasonable agreement with the results of Table 7.

The acoustic waves are longitudinal within the injectors, with their amplitude attaining a maximum value. The waves become slightly longitudinalized within the baffle compartments, and acoustic pressure is more concentrated near the injector plane for the baffled configuration. A similar observation was made by You et al. [79] in the study of acoustic waves in baffled combustors.

The baffled and unbaffled model geometries in Fig. 22a and b respectively are oriented identically in space, as are those in Fig. 25a and b. The addition of baffles alters the preferred spatial orientation of the acoustic mode for both the 1T and 2T modes. A more detailed study of the phenomenon, including the dynamics of spinning waves in baffled combustion chambers, is needed.

5.1.2. Effect of Boundary and Injector Damping

Equation (26) can be expanded to form an explicit function of frequency and used as a boundary condition. This approach, however, is cumbersome for an iterative solver. Instead, nominal constant values of the impedance based on the natural frequencies are determined in advance and used as the boundary condition. Equations (21) and (22), now with Z specified using the impedance model (26) are solved. The values for the impedance are shown in Table 1, along with the nominal eigenmodes frequencies from the previous section used as inputs to the impedance model. Table 9 shows the corresponding damped eigenvalue results. Note that in reality the oscillation frequency and boundary conditions are mutually dependent on each other; the problem is coupled and must be solved iteratively. The change in frequency due to damping effects, however, is generally negligible, and the errors introduced by fixing an impedance value are expected to be small. Fig. 29-Fig. 31 show the acoustic pressure and velocity fields of the first and second tangential modes for the rigid and impedance boundary conditions, respectively. For brevity, only the longitudinal cross sections are presented. No discernable difference in the mode shape between the two different boundary conditions is observed.

Table 8: Nominal flow-distributor impedances applied for each mode

Mode	Frequency (Hz)	Normalized Impedance
1T	1880	$2.624 - 0.365i$
2T	3150	$2.569 - 0.667i$

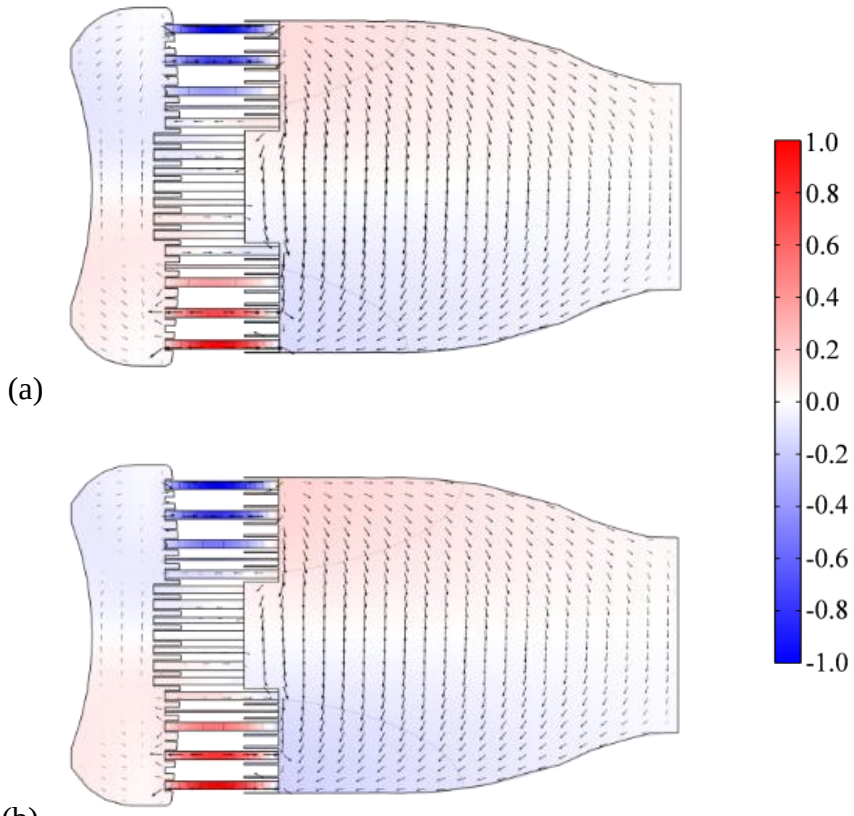

Fig. 29: First tangential (1T) mode shapes of acoustic pressure and velocity at 0° longitudinal cross section for (a) rigid and (b) impedance flow distributor boundary conditions

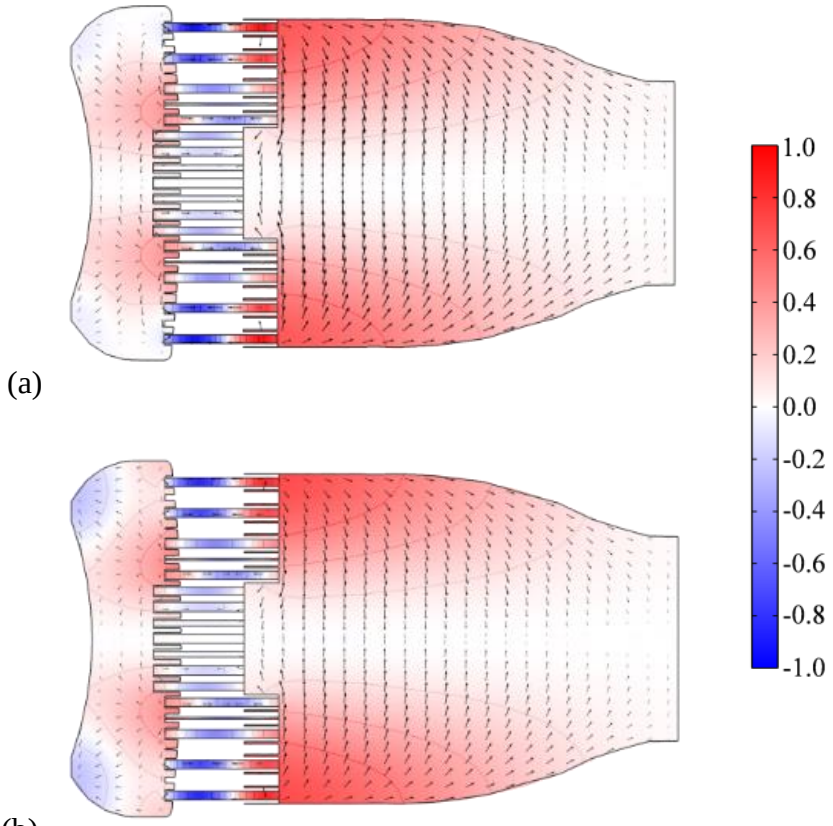

Fig. 30: Second tangential (2T) mode shapes of acoustic pressure and velocity at 0° longitudinal cross section for (a) rigid and (b) impedance flow distributor boundary condition

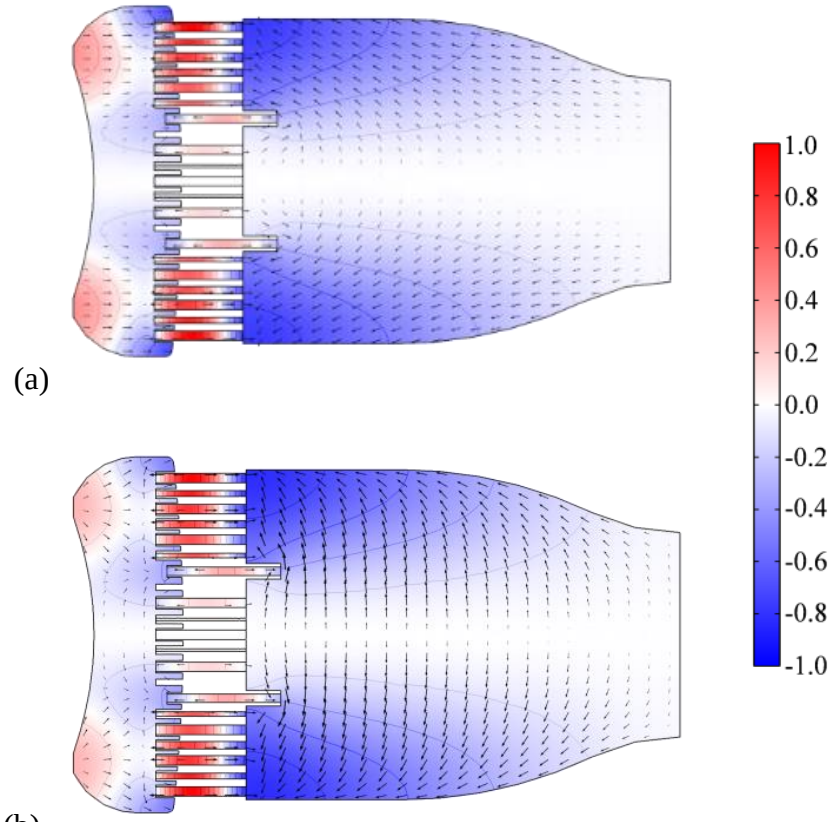

Fig. 31: Second tangential (2T) mode shapes of acoustic pressure and velocity at 90° longitudinal cross section for (a) rigid and (b) impedance flow distributor boundary condition

Table 9: Effect of flow distributor impedance on frequency and damping coefficient

Mode	Frequency (Hz)	Damped frequency (Hz)
1T	1880	$1886 + 6.6i$
2T	3150	$3151 + 1.8i$

The damping of the 2T mode is noticeably less than that of the 1T mode. This is attributable partially to the frequency dependence of the impedance, and partially to the nature of transverse oscillations in the oxidizer manifold. Owing to the small axial extent of the oxidizer plenum, the higher order transverse oscillations translate to a lower average angle of incidence between the incident waves and the distributor plate.

As described in Section 3.1.2., the Strouhal number $\omega R/\hat{u}$ is used to determine the controlling damping mechanism within injectors. The acoustic velocity is selected by assuming that the acoustic pressure $\hat{p}$ is 1% of the mean pressure, a condition valid for a linear acoustic analysis. Table 10 and Table 11 present some relevant flow variables for both injectors. Gas properties are taken from Table 1, where needed.

Table 10: Dimensions and flow parameters for main injector element

Axial Location	R (mm)	St_ω (1T)	St_ω (2T)
Inlet Orifice	4.00	4.50	7.54
Main Passage	5.50	6.19	10.38
Diverging Outlet 1	6.00	6.75	11.32
Diverging Outlet 2	8.87	9.98	16.73

Table 11: Dimensions and flow parameters for baffle injector element

Axial Location	R (mm)	St_ω (1T)	St_ω (2T)
Inlet Orifice	3.50	3.94	6.60
Main Passage	5.00	5.63	9.43
Second Passage	6.50	7.32	12.26

Note that the Mach number remains small throughout the injector except in the thin inlet orifice. The Strouhal numbers exceed unity over the entire injector, which suggests that for small amplitudes within the linear acoustic regime, viscous dissipation dominates the acoustic damping of the injectors. The situation may become different when oscillations become so strong that the energy transfer from the acoustic to the vortical mode prevails. Under that condition, both viscous dissipation and acoustic-viscous interaction should be considered to account for the acoustic damping of injectors.

In the present analysis, an impedance model for laminar viscous dissipation implemented. Such an impedance model was applied in Searby et al. [59] to accounting for the viscous damping within a resonator bank; it was applied as a lumped resistive layer at the entrance plane of the bank. In the current work, the injectors are included as part of the computational domain, and the impedance is applied along the interior surface of the injector. Further, only longitudinal acoustic motions are expected in the injectors because the radius is small. The impedance (29) is thus specified to the case $\theta = 90°$. Table 12 gives the values employed for the equivalent density and speed of sound based on the normal frequencies of the 1T and 2T modes, and Table 13 shows the effect on frequency

growth rate. Fig. 32-Fig. 34 show the 1T and 2T mode shapes resulting from the solution of Eqs. (21) and (22) with the indicated gas properties for cases with and without injector damping.

Table 12: Equivalent gas properties used for characterizing injector damping

Mode	Frequency (Hz)	Complex Density ρ_v (kg/m^3)	Speed of Sound c_v (m/s)
1T	1880	$32.3 - 0.785i$	487.3
2T	3150	$25 - 0.785i$	487.34

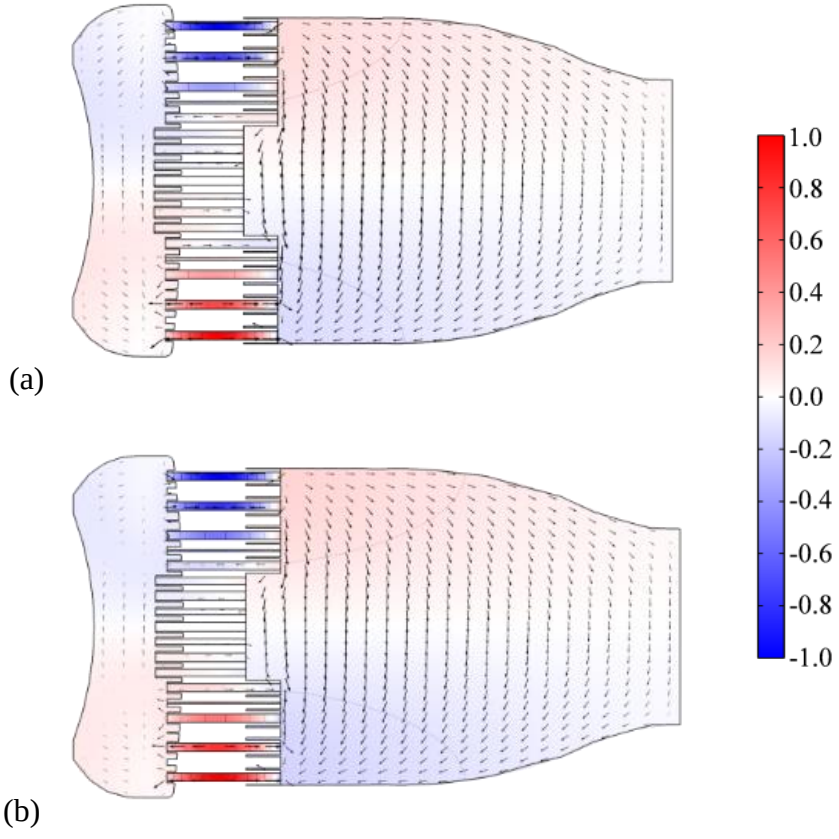

(a)

(b)

Fig. 32: First tangential (1T) mode shapes for pressure and velocity at 0° longitudinal cross section (a) with and (b) without injector damping

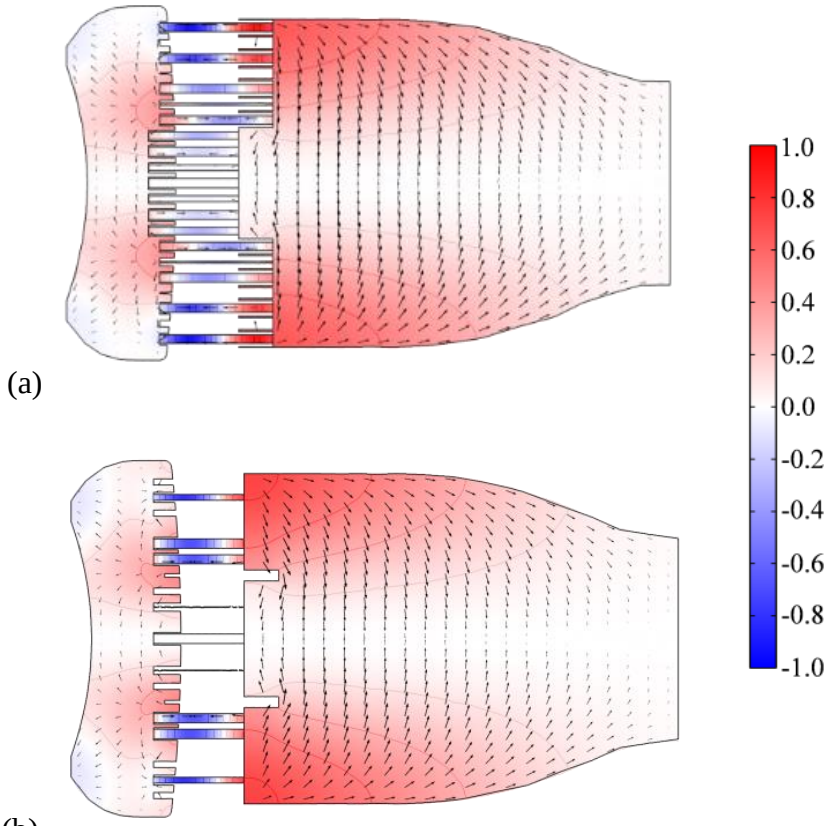

Fig. 33: Second tangential (2T) mode shapes of acoustic pressure and velocity at 0° longitudinal cross section (a) with and (b) without injector damping

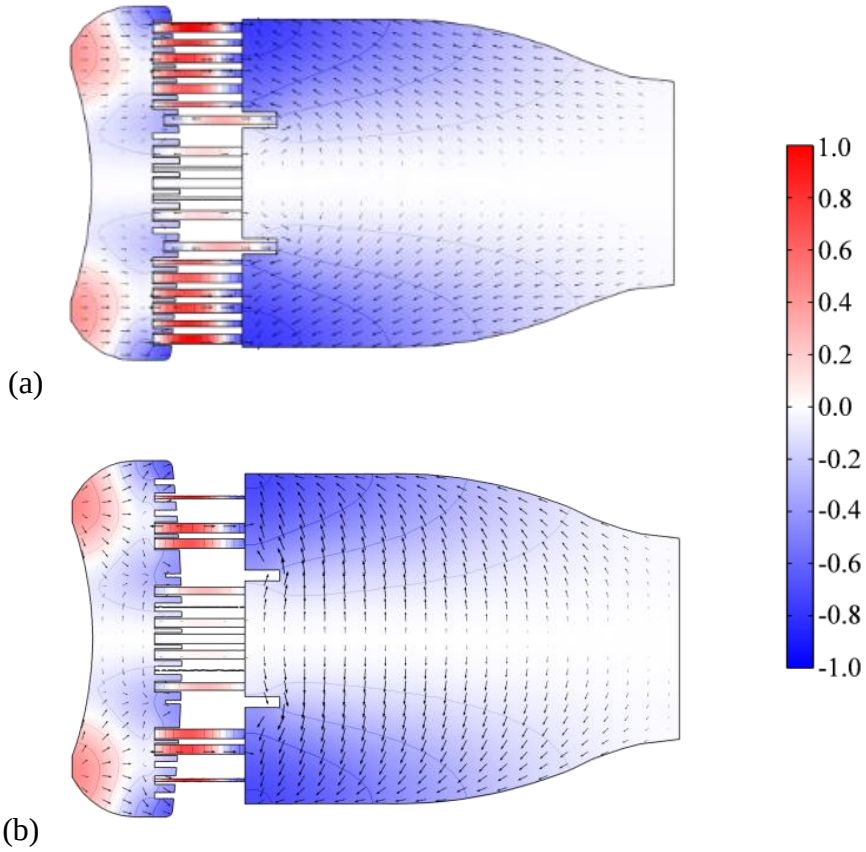

Fig. 34: Second tangential (2T) mode shapes of pressure and velocity at 90° longitudinal cross section (a) with and (b) without injector damping

Table 13: Effect of injector damping on frequency and damping coefficient

Mode	Mode Frequency (Hz)	Damped Frequency (Hz)
1T	1880	$1868 + 7.08i$
2T	3150	$3210 + 3.14i$

Again the damping of the 2T mode is lower than that of the 1T mode. However in this instance, the effects of frequency dependence predominates. Because the viscous damping is applied only within the injectors, and because in all cases the acoustic motions are

completely longitudinalized in this region, there is unlikely to be a significant difference associated with acoustic mode shape. Increasing the length of the injectors would straightforwardly increase the damping by virtue of the larger surface area over which the viscous stresses act. However this would potentially come at the expense of reduced injector performance due to unwanted flow losses.

5.1.3. Effect of Mean Flow

Both major types of mean flow effect are examined in this section. First we specify a uniform, axial flow with speed U. All solid surfaces are specified as acoustically closed ($Z \to \infty$), so as to isolate the effects of mean flow, rather than to elucidate the coupling of mean flow with impedance surfaces. The mean flow velocity U is applied piecewise with three nominal values: 17.63 m/s in the oxidizer dome, 93.4 m/s within the injectors, and 326.9 m/s in the main chamber, in accordance with the flow conditions in the RD-170 engine. These values were determined based on mass flow rate analysis for the RD-170. Secondly we add the effects of flow divergence by incorporating the swirling injector velocity fields shown in Section 4.1. Fig. 35-Fig. 37 show the 1T and 2T modes of acoustic pressure and velocity for cases with and without mean flow effects. The mode shapes for uniform mean flow are qualitatively indistinguishable from those for nonuniform flow, therefore the plots are not presented twice. Table 14 gives the calculated frequencies and damping coefficients of the acoustic oscillations.

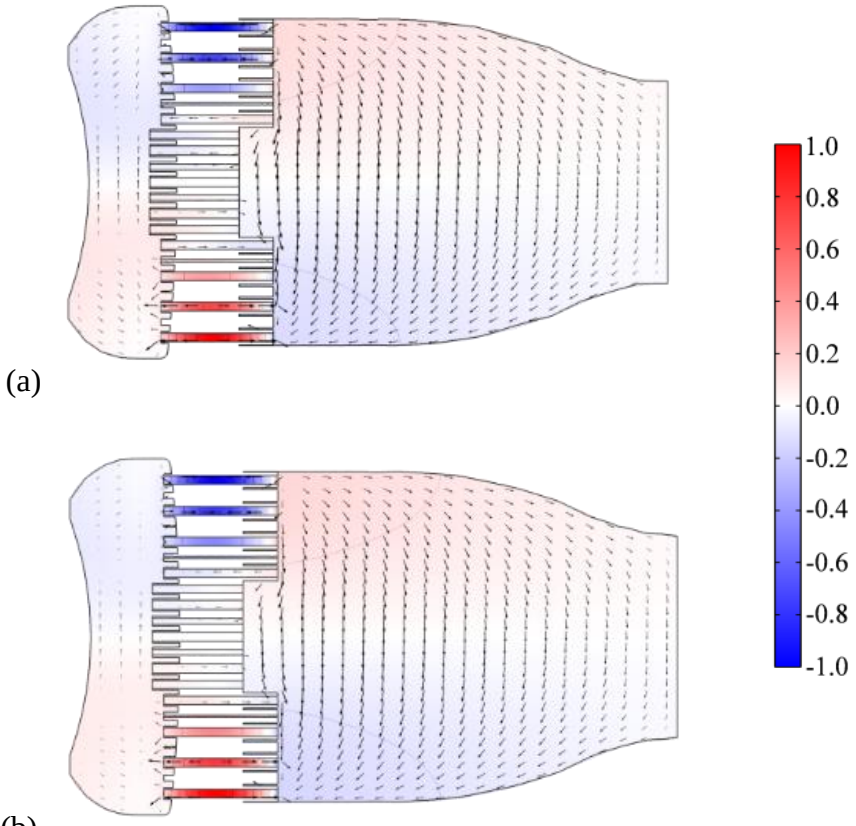

Fig. 35: First tangential (1T) mode shapes of pressure and velocity at 0° longitudinal cross section (a) with and (b) without mean flow

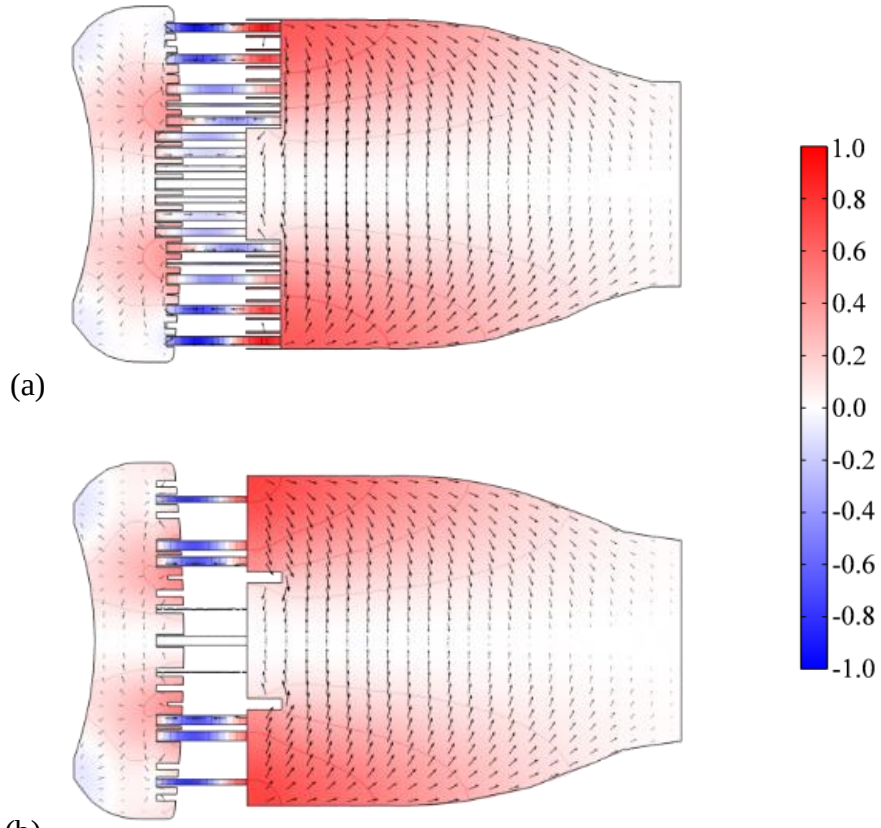

Fig. 36: Second tangential (2T) mode shapes of acoustic pressure and velocity at 0° longitudinal cross section (a) with and (b) without mean flow

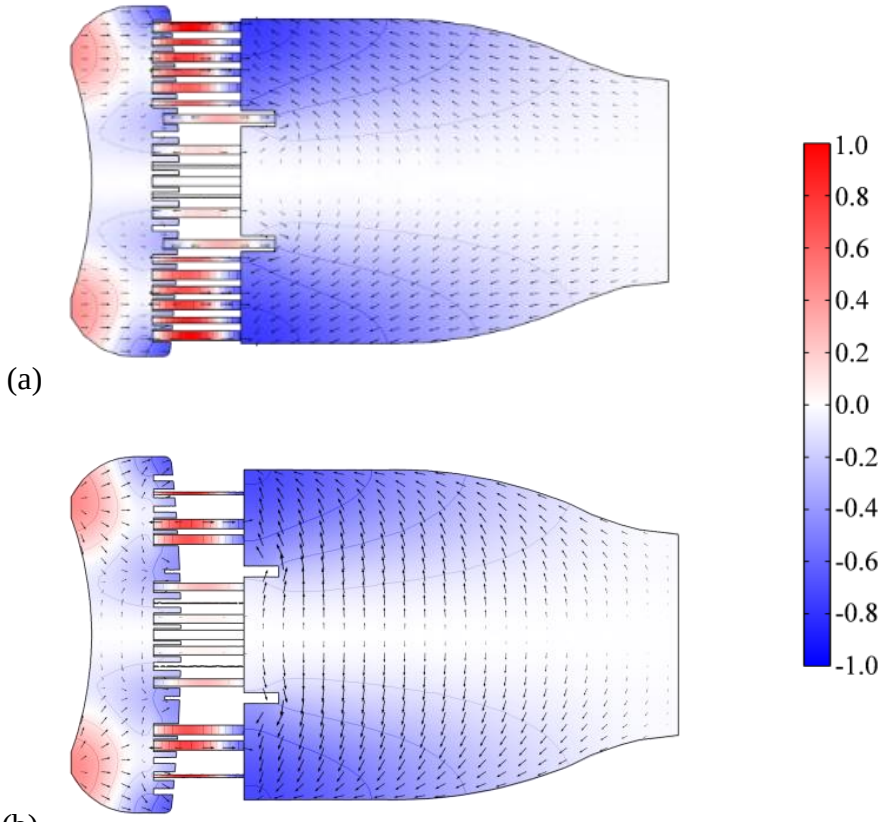

Fig. 37: Second tangential (2T) mode shapes of acoustic pressure and velocity at 90° longitudinal cross section (a) with and (b) without mean flow

Table 14: Effect of mean flow on frequency and damping coefficient

Mode	No Flow (Hz)	Uniform Flow (Hz)	Nonuniform Flow (Hz)
1T	1880	1874 + 32.4*i*	1870 + 40.2*i*
2T	3150	3142 + 53.5*i*	3131 + 65.1*i*

The damping provided by a mean flow appears to be significantly larger than other effects. In the presence of a uniform flow, the damping coefficient increases from 6.6 to 32.4 for the 1T mode and from 1.8 to 53.5 for the 2T mode, as compared with the contributions

from the flow distributor. The oscillation frequency is slightly reduced from the no-flow case, in qualitative agreement with modal theories. The large damping resulting from the mean flow may be attributable to convective losses of acoustic energy. Even in the case of a perfectly reflective exit plane (such as that employed here), acoustic energy is convected out by the mean flow, and the acoustic energy in the system is reduced.

This effect may be further explained with a calculation for an analogous cylindrical chamber. Consider a chamber of radius R with a uniform mean flow of Mach number M. The pressure and axial velocity fields may be constructed as superpositions of known eigen-solutions as follows

$$p'(x,r,\theta,t) = e^{i\Omega t}\sum_{n=-\infty}^{\infty}\sum_{m=0}^{\infty} J_n\left(\frac{\alpha_{nm}r}{R}\right)e^{in\theta}\left[P_{nm}^{+}e^{ik_{nm}^{+}x} + P_{nm}^{-}e^{ik_{nm}^{-}x}\right] \qquad (46)$$

$$u'(x,r,\theta,t) = -\frac{1}{\bar{\rho}\bar{c}}e^{i\Omega t}\sum_{n=-\infty}^{\infty}\sum_{m=0}^{\infty} J_n\left(\frac{\alpha_{nm}r}{R}\right)e^{in\theta}\left[\frac{P_{nm}^{+}k_{nm}^{+}e^{ik_{nm}^{+}x}}{k+Mk_{nm}^{+}} + \frac{P_{nm}^{-}k_{nm}^{-}e^{ik_{nm}^{-}x}}{k+Mk_{nm}^{-}}\right] \qquad (47)$$

where J_n denotes the Bessel function of the first kind of order n, α_{nm} the mth root of $J_n'(r)$, and

$$k_{nm}^{\pm} = \frac{kM \mp \sqrt{k^2 - (\alpha_{nm}/R)^2(1-M^2)}}{1-M^2}$$

The power transmitted axially by the acoustic field is given by the integral of the axial acoustic intensity over the cross-sectional area of the chamber:

$$\mathcal{P} = \int_S \langle \boldsymbol{I} \cdot \boldsymbol{e}_x \rangle \, dS$$

Using the expressions for pressure and velocity, this ultimately yields

$$\mathcal{P} = \frac{\pi R^2}{\bar{\rho}\bar{c}} (1 - M^2)^2 \sum_{n=-\infty}^{\infty} \sum_{m=0}^{m_0} \sigma_{nm} \left[\frac{|P_{nm}^+|^2}{(1 - M\sigma_{nm})^2} - \frac{|P_{nm}^-|^2}{(1 + M\sigma_{nm})^2} \right] \tag{48}$$

where m_0 denotes the number of cut on modes and an additional numerical factor from the Bessel function integration has been absorbed into the arbitrary modal amplitudes. The nondimensional group σ_{nm} is defined as $\sqrt{1 - (\alpha_{nm}/R)^2(1 - M^2)}$. Residual contributions from coupled evanescent modes are omitted.

Let us consider the contribution for a single arbitrary mode. We retain only the downstream propagating wave, as this is the component that transmits acoustic energy out of the domain:

$$\frac{\bar{\rho}\bar{c}\mathcal{P}_{nm}(M)}{\pi R^2 |P_{nm}^+|^2} = \frac{(1 - M^2)^2 \sqrt{1 - (\alpha_{nm}/kR)^2(1 - M^2)}}{\left[1 - M\sqrt{1 - (\alpha_{nm}/kR)^2(1 - M^2)}\right]^2}$$

Forming the ratio $\mathcal{P}_{nm}(M)/\mathcal{P}_{nm}(0)$ eliminates the remaining nondimensional scaling factor and allows for easier interpretation:

$$\frac{\mathcal{P}_{nm}(M)}{\mathcal{P}_{nm}(0)} = \frac{(1 - M^2)^2 \sqrt{1 - (\alpha_{nm}/kR)^2(1 - M^2)}}{\sqrt{1 - (\alpha_{nm}/kR)^2}\left[1 - M\sqrt{1 - (\alpha_{nm}/kR)^2(1 - M^2)}\right]^2} \tag{49}$$

which shows a monotonic increase in downstream power transmission with increasing Mach number.

Because of the nonuniform cross-section of the RD-170 main chamber and the coupling effects with upstream components, this calculation cannot be taken as exact. As the flow traverses the chamber, the decrease in area causes acceleration which culminates at the throat.

When the swirling shear flow downstream of the injectors is included, the damping increases even further. It is known that in the presence of shear flow acoustic wavefronts are diverted toward regions of low mean-velocity, which means that they will be directed to solid surfaces to be damped.

5.1.4. Effect of Combustion Response and Sensitivity Analysis

We shall combine in this section the results from the noncompact combustion response fields and the sensitivity analysis for the combustion response parameters, the methodology of which was outlined in Section 4.3. Fig. 38-Fig. 40 show the mode shapes results, and Table 15 shows the eigenvalues for all three combustion response cases.

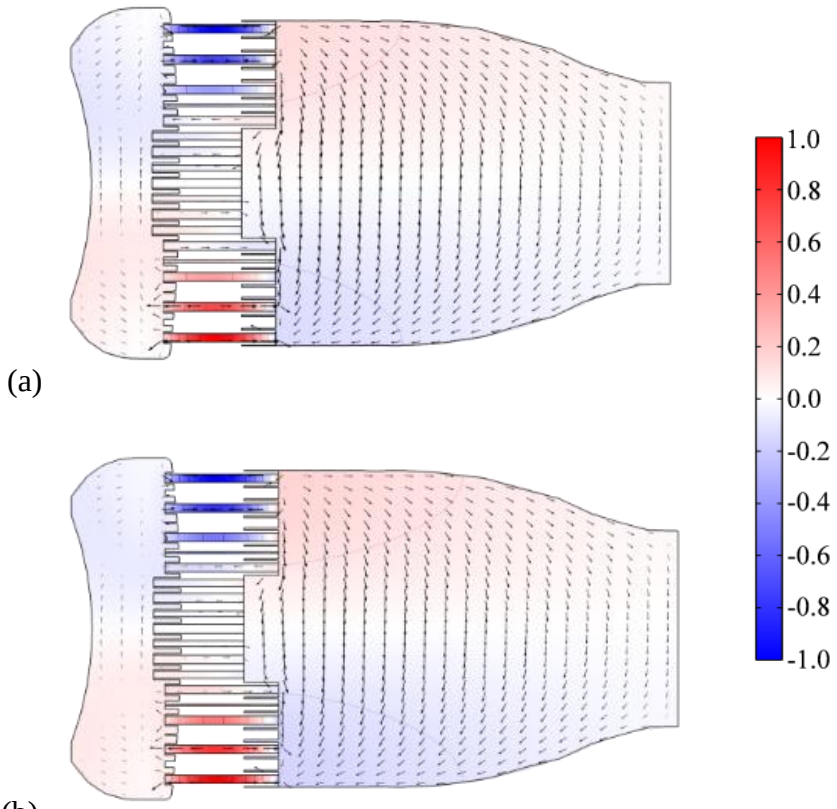

Fig. 38: First tangential (1T) mode shapes of acoustic pressure and velocity at 0° longitudinal cross section (a) with and (b) without combustion response.

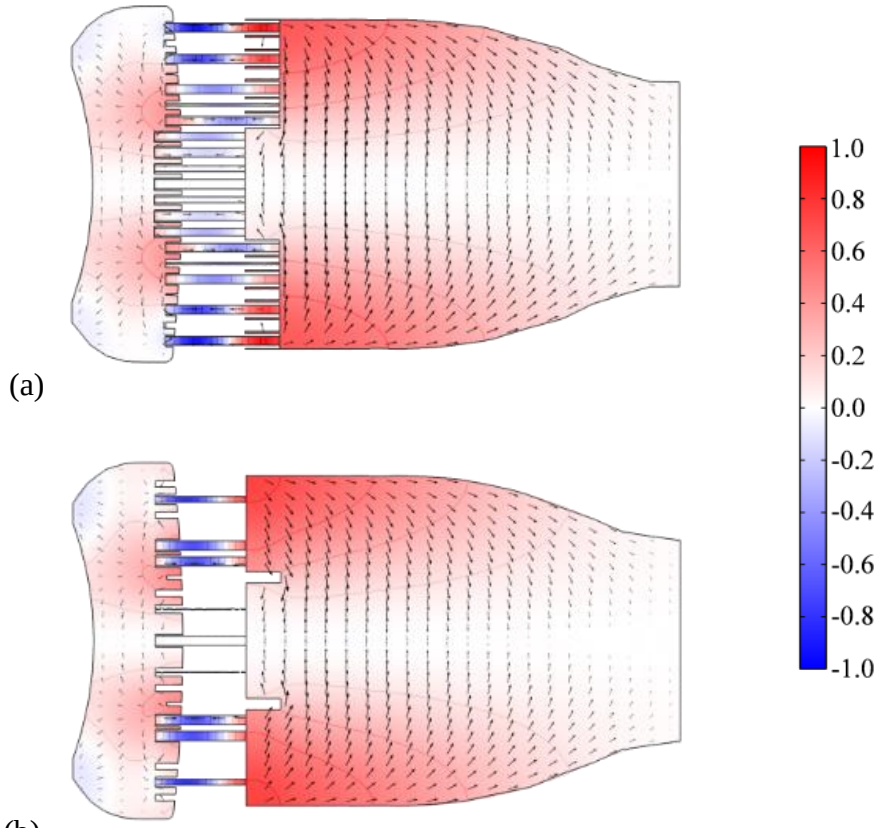

Fig. 39: Second tangential (2T) mode shapes of acoustic pressure and velocity at 0° longitudinal cross section (a) with and (b) without combustion response.

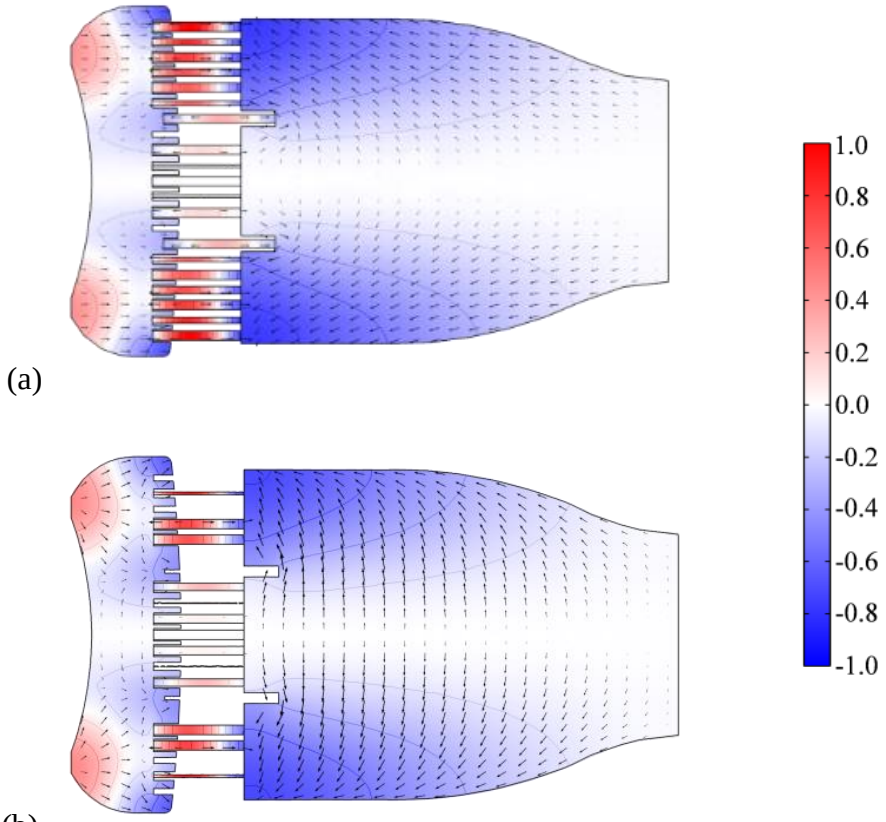

Fig. 40: Second tangential (2T) mode shapes of acoustic pressure and velocity at 90° longitudinal cross section (a) with and (b) without combustion response.

Table 15: Effect of distributed FTF on frequency and damping coefficient

Mode	Without FTF (Hz)	Full Recess FTF (Hz)	Intermediate Recess FTF (Hz)	No Recess FTF (Hz)
1T	1880	1870 – 39.4*i*	1870 – 39.8*i*	1872 – 41.3*i*
2T	3150	3141 – 60*i*	3142 – 60.8*i*	3139 – 62.2*i*

We shall conduct a sensitivity analysis for the parameters of the combustion response fields for each of the injector recess lengths. We consider a $\pm 10\%$ deviation in each of the characteristic combustion response quantities listed in Table 4. Fig. 41-Fig. 45 show the results for the full recess, Fig. 46-Fig. 50 for the intermediate recess, and Fig. 51-Fig. 55 for the case with no recess.

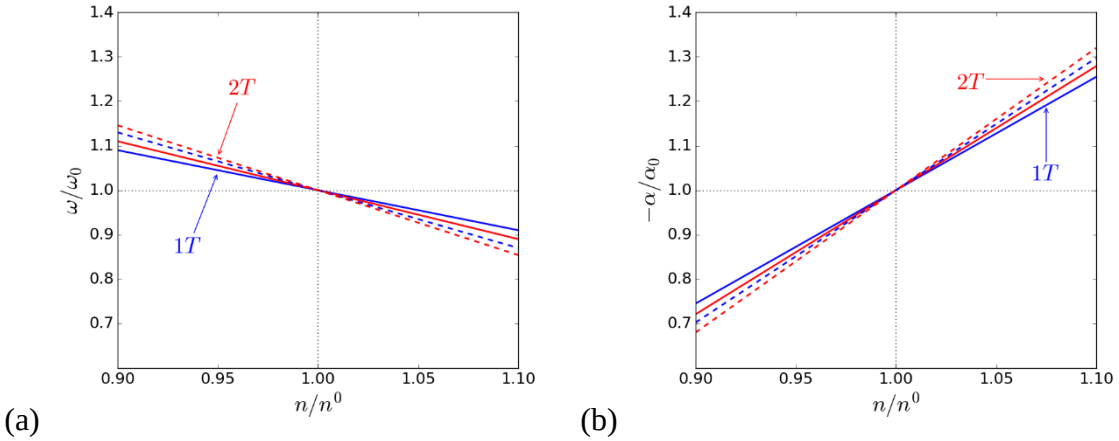

(a) (b)

Fig. 41: Sensitivity of (a) frequency and (b) growth rate to FTF gain parameters for the full recess FTF. Solid: $n_{\text{avg}}/n^0_{\text{avg}}$, dashed: $n_{\text{max}}/n^0_{\text{max}}$

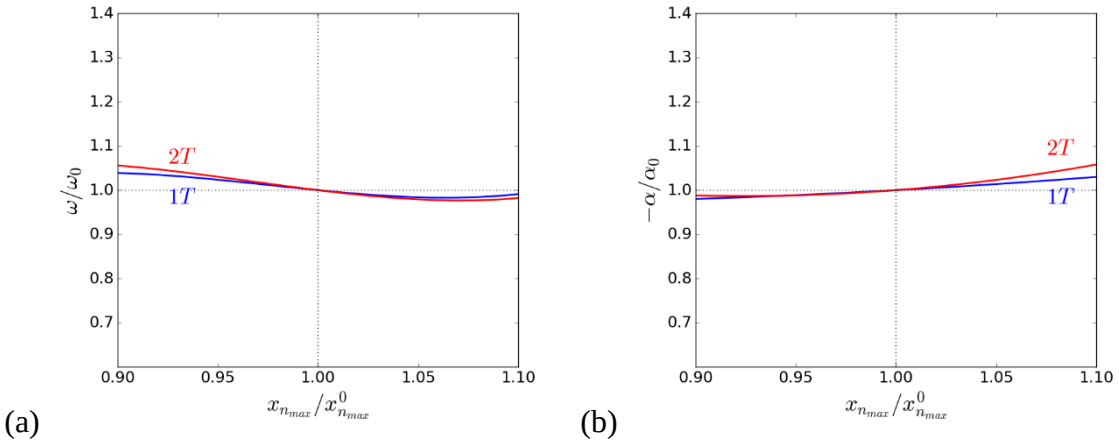

(a) (b)

Fig. 42: Sensitivity of (a) frequency and (b) growth rate to axial location of maximum FTF gain for the full recess FTF.

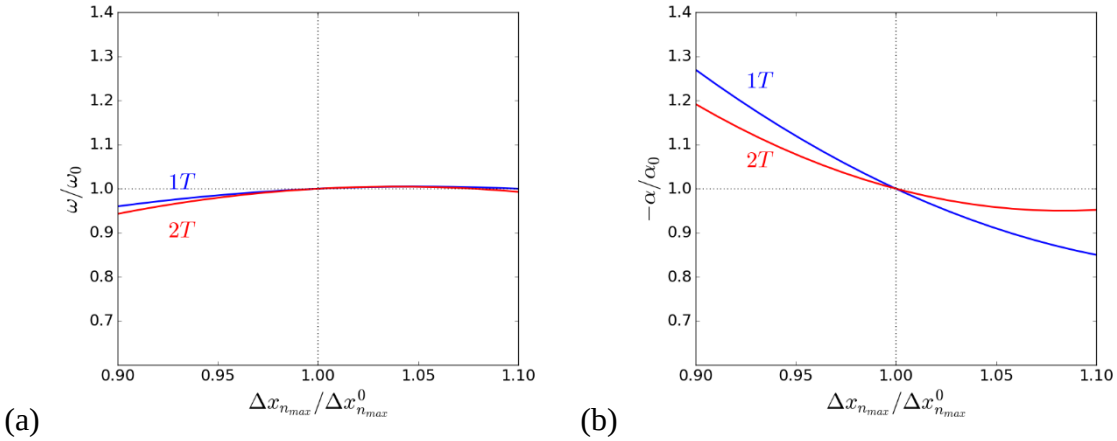

(a) (b)

Fig. 43: Sensitivity of (a) frequency and (b) growth rate to spread of FTF gain about maximum for the full recess FTF.

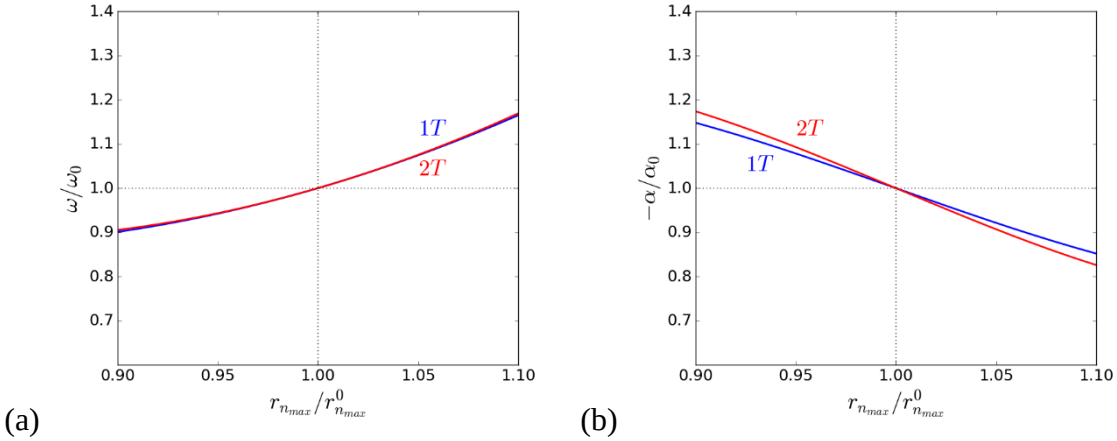

(a) (b)

Fig. 44: Sensitivity of (a) frequency and (b) growth rate to radial location of maximum FTF gain for the full recess FTF.

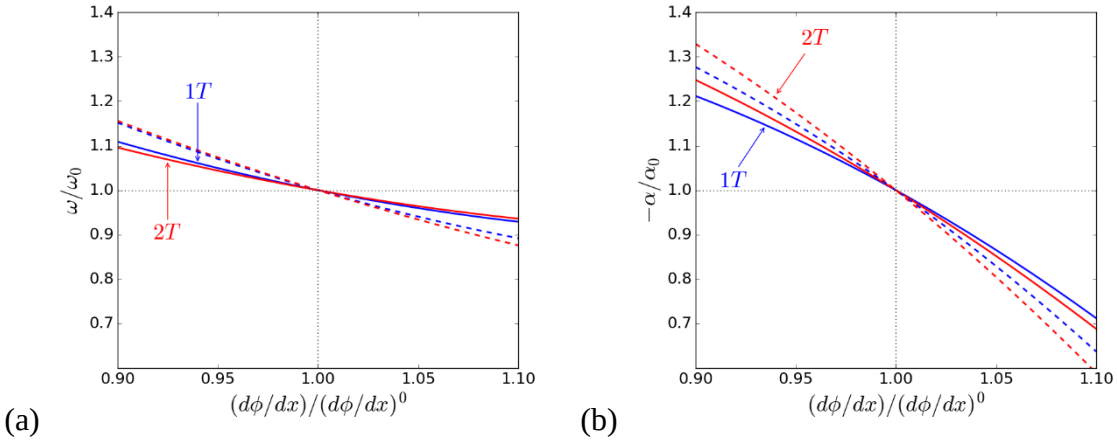

(a) (b)

Fig. 45: Sensitivity of (a) frequency and (b) growth rate to axial FTF phase slope for the full recess FTF. Solid: $(d\phi/dx)_{\text{avg}}/(d\phi/dx)^0_{\text{avg}}$, dashed: $(d\phi/dx)_{\text{max}}/(d\phi/dx)^0_{\text{max}}$

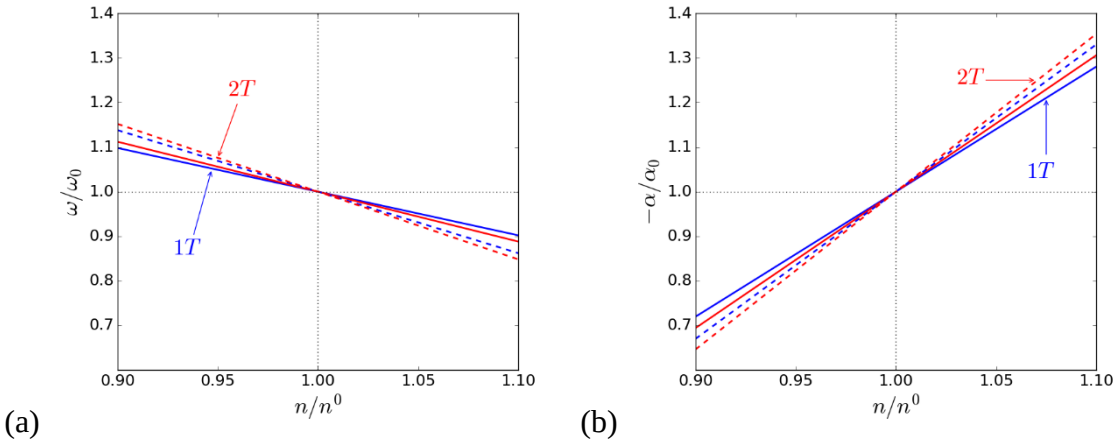

(a) (b)

Fig. 46: Sensitivity of (a) frequency and (b) growth rate to FTF gain parameters for the intermediate recess FTF. Solid: $n_{\text{avg}}/n^0_{\text{avg}}$, dashed: $n_{\text{max}}/n^0_{\text{max}}$

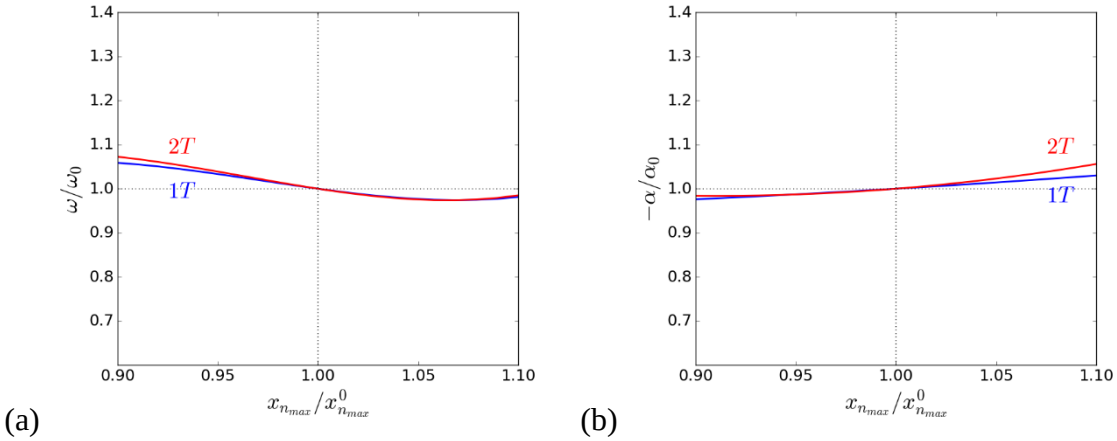

(a) (b)

Fig. 47: Sensitivity of (a) frequency and (b) growth rate to axial location of maximum FTF gain for the intermediate recess FTF.

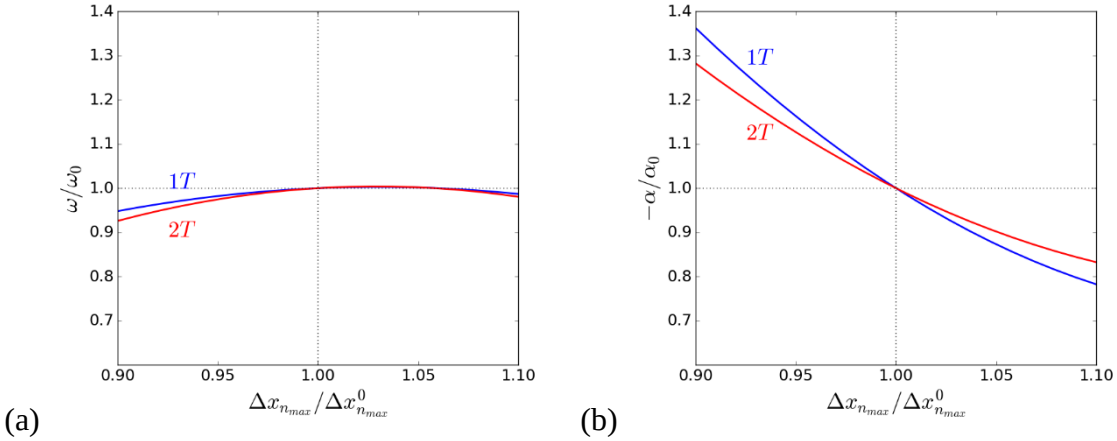

(a) (b)

Fig. 48: Sensitivity of (a) frequency and (b) growth rate to spread of FTF gain about maximum for the intermediate recess FTF.

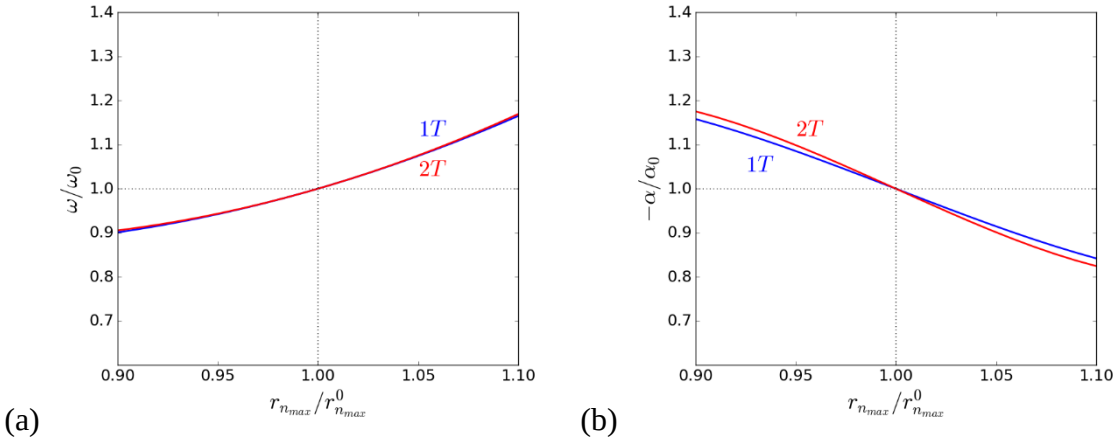

(a) (b)

Fig. 49: Sensitivity of (a) frequency and (b) growth rate to radial location of maximum FTF gain for the intermediate recess FTF.

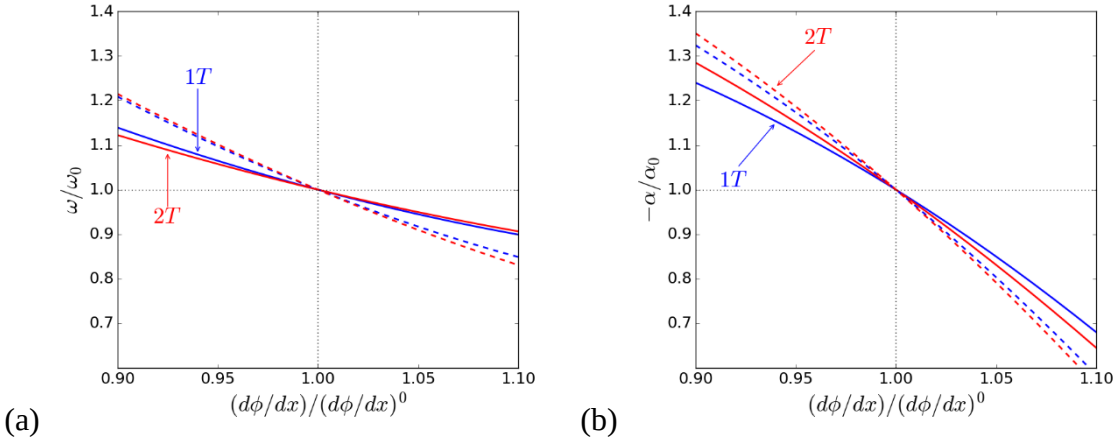

(a) (b)

Fig. 50: Sensitivity of (a) frequency and (b) growth rate to axial FTF phase slope for the intermediate recess FTF. Solid: $(d\phi/dx)_{\text{avg}}/(d\phi/dx)^0_{\text{avg}}$, dashed: $(d\phi/dx)_{\text{max}}/(d\phi/dx)^0_{\text{max}}$

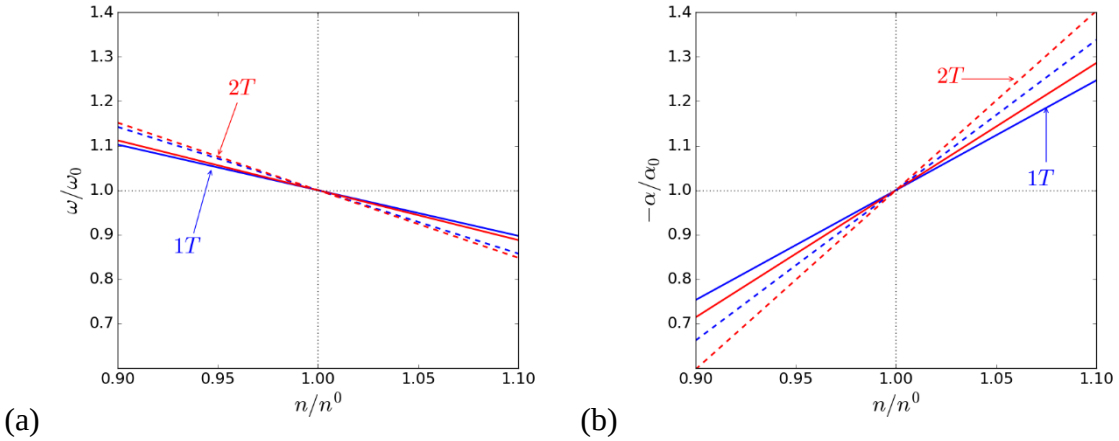

(a) (b)

Fig. 51: Sensitivity of (a) frequency and (b) growth rate to FTF gain parameters for the no recess FTF. Solid: $n_{\text{avg}}/n^0_{\text{avg}}$, dashed: $n_{\text{max}}/n^0_{\text{max}}$

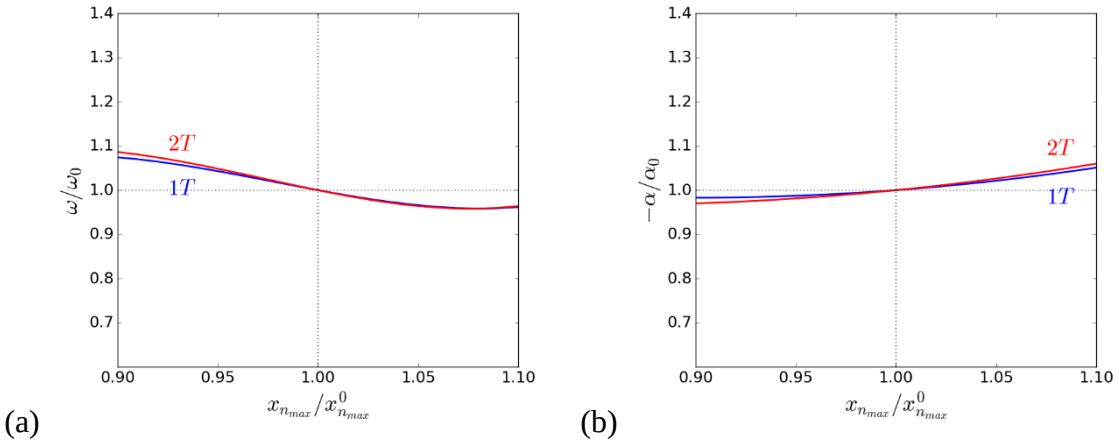

(a) (b)

Fig. 52: Sensitivity of (a) frequency and (b) growth rate to axial location of maximum FTF gain for the no recess FTF.

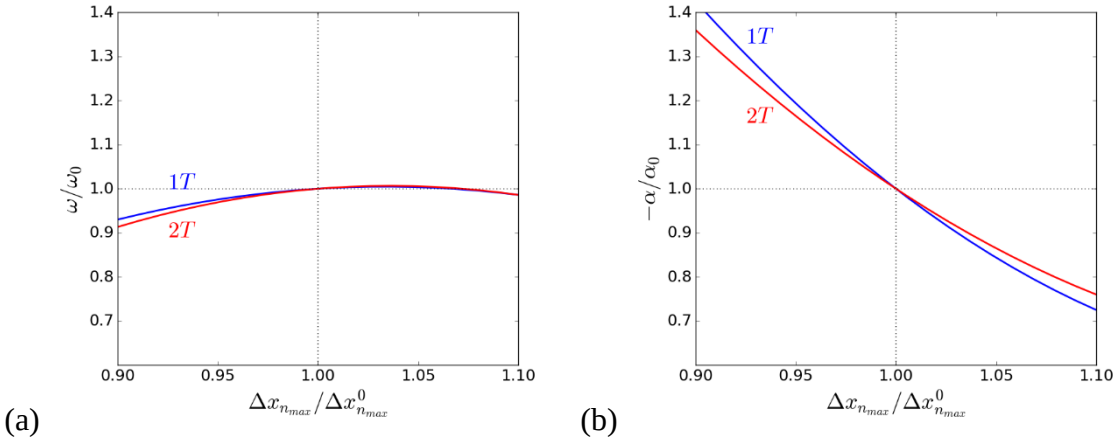

(a) (b)

Fig. 53: Sensitivity of (a) frequency and (b) growth rate to spread of FTF gain about maximum for the no recess FTF.

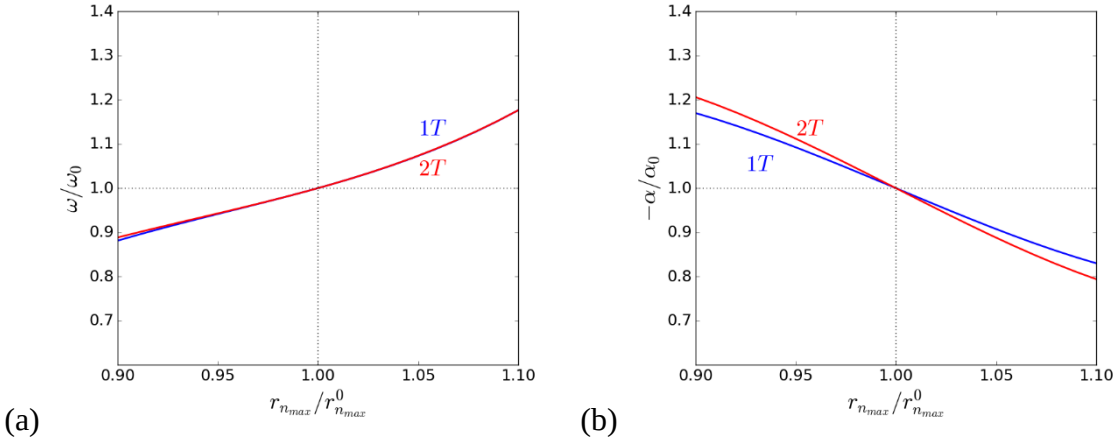

(a) (b)

Fig. 54: Sensitivity of (a) frequency and (b) growth rate to radial location of maximum FTF gain for the no recess FTF.

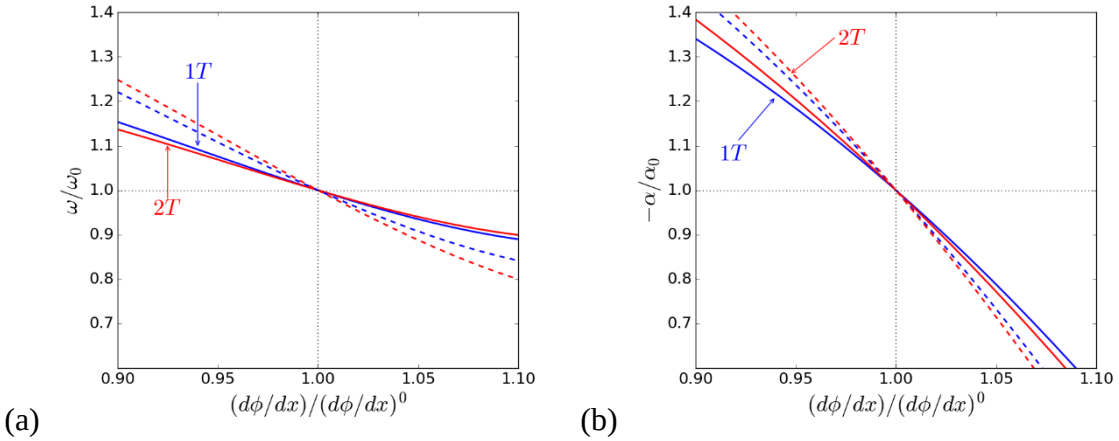

(a) (b)

Fig. 55: Sensitivity of (a) frequency and (b) growth rate to axial FTF phase slope for the no recess FTF. Solid: $(d\phi/dx)_{\text{avg}}/(d\phi/dx)^0_{\text{avg}}$, dashed: $(d\phi/dx)_{\text{max}}/(d\phi/dx)^0_{\text{max}}$

The sensitivity results illuminate the controlling physics of the system, and there are many features to note from the foregoing plots. Firstly, it can be seen that overall the three recess configurations can be ranked from least sensitive to most sensitive as follows: full recess, intermediate recess, no recess. That is, the sensitivity generally increases as the recess length decreases. By "more sensitive" it is meant that for any given perturbation, for example $n_{\text{avg}}/n^0_{\text{avg}}$, *in most cases* the corresponding change in output quantities (ω/ω^0 and $-\alpha/\alpha^0$) is greater. This may be attributed to the exposure of the flame base to oscillations in the main chamber. The heat release distribution for a nonpremixed flame is such that most occurs at the base, where the species gradients are the greatest. An exception is the change in growth rate sensitivities between the intermediate and no recess cases as a function of the average FTF gain; that is, between the solid lines in Fig. 46b and Fig. 51b. In this case, the sensitivities for the no recess case are slightly lowered from the intermediate recess case.

It is also of note that the second tangential mode is in general more sensitive to perturbations in combustion parameters than the first tangential mode. This may be due to the increased gradients of acoustic pressure and velocity in the 2T mode in the regions that excite heat release oscillations.

In Fig. 41, Fig. 46, and Fig. 51 the results for perturbations in the average and maximum FTF gain are displayed on the same axis. Results for both 1T and 2T modes exhibit higher sensitivities to $n_{\max}$ than n_{avg}. Likewise Fig. 45, Fig. 50, and Fig. 55 show the results for average and maximum axial FTF phase slope are displayed on the same axis, and similarly the sensitivity to $(d\phi/dx)_{\max}$ is greater than that of $(d\phi/dx)_{\text{avg}}$. In particular, the sensitivities for the maximum phase slopes are greater than the sensitivities for average phase slopes for all conditions.

The most significant parameters which affect the stability of the system via the growth rate across all conditions are seen to be the FTF gain, the spread of the gain about its maximum value as defined earlier, and the axial slope of the phase. The effect of the FTF gain is expected and easily understood; an increase in the gain (as measured either by the mean or maximum) represents an increase in the amount of energy transferred to the acoustic field and thus an increase in the growth rate. On the other hand, a negative trend in growth rate is observed for both the axial spread about the maximum gain and the axial phase slope. Both of these trends are qualitatively consistent with simplified theoretical studies of linearized acoustic response to unsteady heat release. In their report on ORSC engine technology development, Yang et al. [9] conducted a similar computational study using a simplified combustion response model. They found that increasing the overall axial extent over which the combustion response was spread caused an increase in stability.

The radial location of maximum gain is also seen to have a negative correlation with growth rate. This is corroborated by Li et al. [80] who showed that an increase in spatial (in this case azimuthal) nonuniformity of combustion response parameters likewise has a stabilizing effect. As $r_{n_{\max}}$ increases, the maxima for two adjacent flames approach each other more closely and the chamber level field becomes more unevenly distributed.

Overall the largest influence on the growth rate for all injector configurations is the axial phase slope. The axial phase slope straightforwardly quantifies how quickly the phase changes downstream, and thus serves as one measure of noncompactness. It also may be viewed as a spatial analog of the time delay, which is sometimes expressed in simplified combustion models as $\tau \approx d\phi/d\omega$. Though this provides a potential qualitative explanation of the influence of the phase slope, the analogy likely has limits since the functional dependence of the growth rate on the time delay is known to be oscillatory over a large enough range [81]. That is, it is unclear if there are regions of stability that correspond to certain gradations of the phase field analogous to regions of stability corresponding to certain time delay ranges. The actual frequency derivative of the phase is not utilized in the present study because of the outsized computational cost involved in computing it for all conditions. The phase is not computed as an explicit function of frequency; it and the gain are only computed for certain discrete frequencies as outlined in Section 4.2.

5.2. Preburner

In this section we shall review the eigenvalue results for the preburner. Equations (21) and (22) are solved over the geometries for both a single preburner and the preburner-turbine assembly, shown in Fig. 3b and Fig. 4.

5.2.1. Single Preburner

The overall length of the single preburner is 0.637 m, and its maximum diameter, that of the mixing chamber, is 0.294 m. Additional dimensions are shown in the references [9]. Fig. 56 shows the acoustic pressure and velocity distributions on a longitudinal cross-section of the preburner. The corresponding eigenfrequencies are given in Table 16. The outlet boundary condition is treated as acoustically open to reflect the fact that there is no obstruction at this plane between the preburner and the turbine hub.

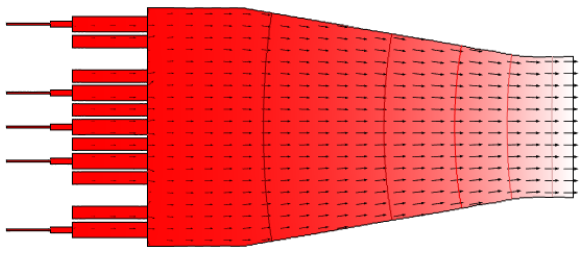

(a)

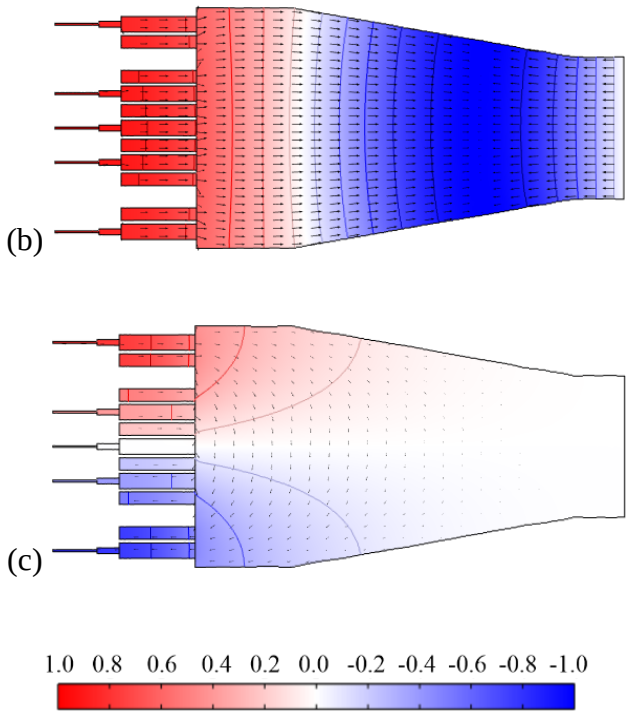

Fig. 56: Acoustic pressure and velocity distributions on a longitudinal cross-section of the preburner (a) Bulk mode (b) 1L mode (c) 1T mode

Table 16: Eigenfrequencies (Hz) of preburner for acoustically open outlet condition

Bulk Mode	1L	1T
199	797	995

5.2.2. Preburner-Turbine Inlet Hub

For the composite preburner-turbine inlet assembly, several boundary conditions are considered for the turbine inlet-annulus: open, closed, and the blade row impedance discussed in Section 3.2. Fig. 57 shows the acoustic pressure and velocity distributions on a longitudinal cross-section of the assembly. The corresponding surface pressure

distributions are presented in Fig. 58. Table 17 lists the eigenvalues for all boundary conditions. Because the pressure distributions do not change appreciably for different boundary conditions, they are only presented once.

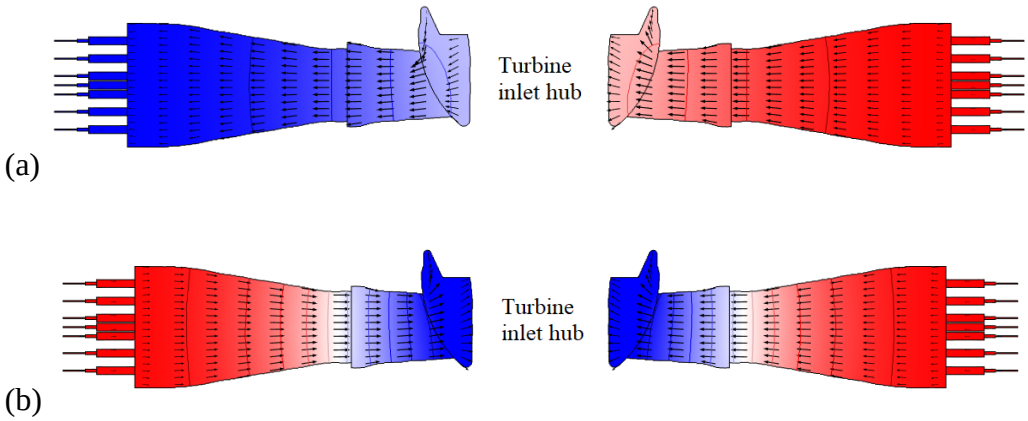

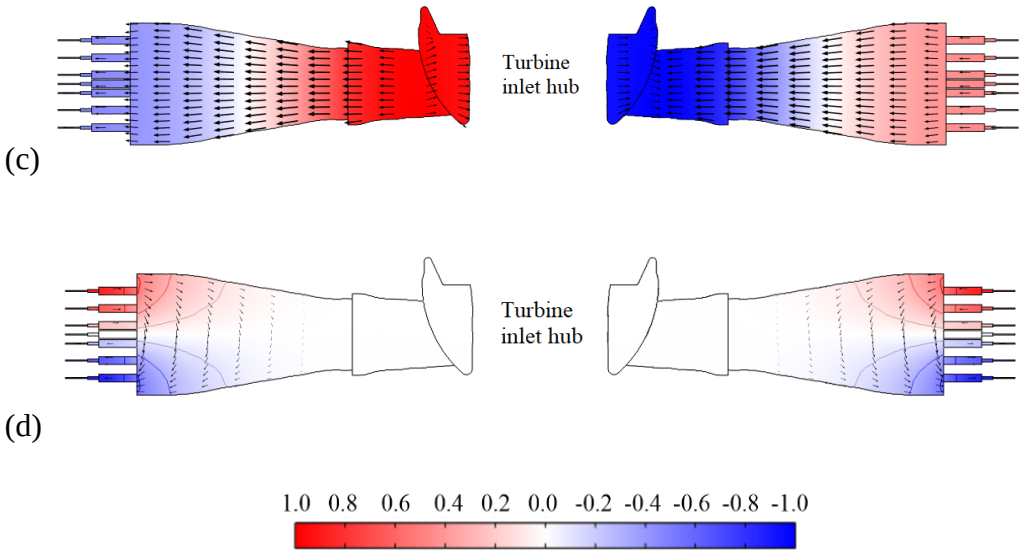

Fig. 57: Acoustic pressure and velocity distributions on a longitudinal cross-section of the preburner-turbine inlet hub assembly, (a) 1L mode (b) 2L mode (c) 3L mode (d) 1T mode (reoriented so nodal surfaces are coplanar)

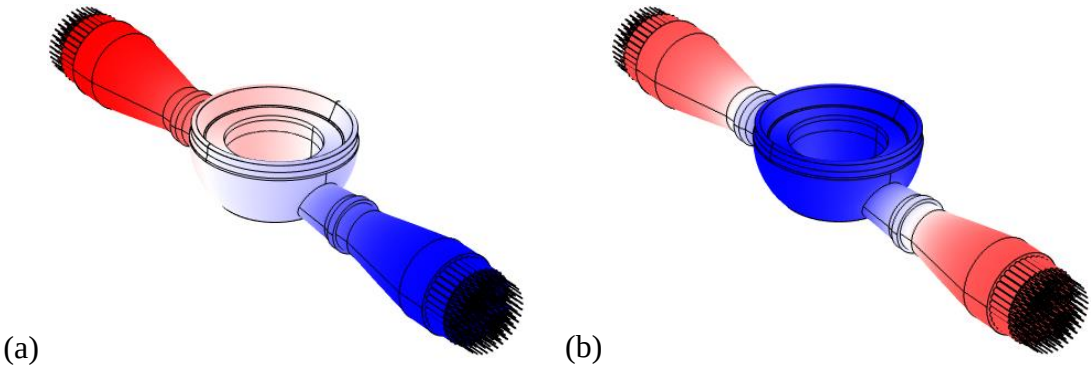

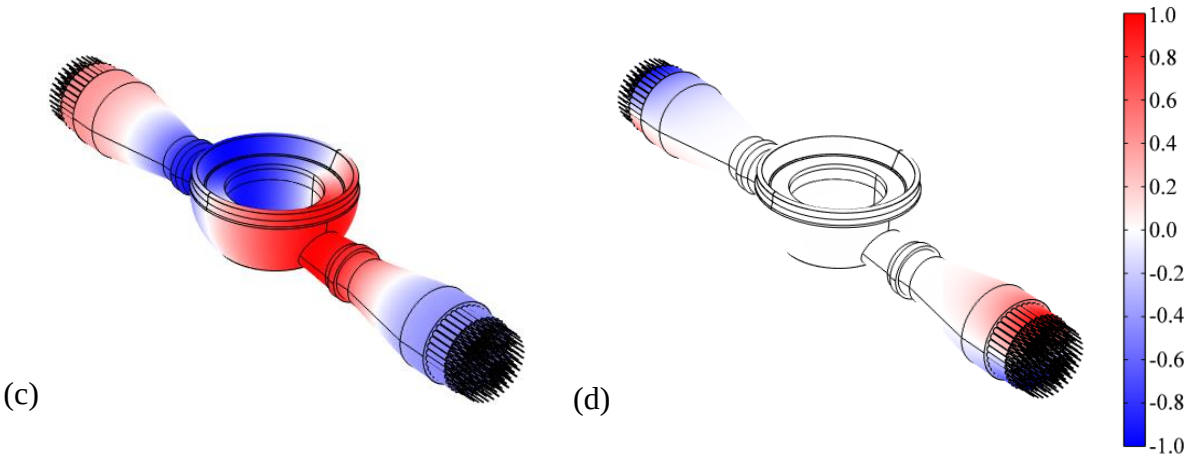

Fig. 58: Surface distribution of acoustic pressure in the preburner-turbine inlet hub assembly (a) 1L mode (b) 2L mode (c) 3L mode (d) 1T mode

Table 17: Eigenfrequencies (Hz) of preburner-turbine inlet assembly for indicated boundary condition

Turbine BC	1L	2L	3L	1T
Closed	113	215.7	423	995
Open	127.5	N/A	541.6	995
Impedance	$113 + 2.9i$	$174.3 + 66.5i$	$441 + 57.7i$	995

The lowest mode exhibited by the single preburner geometry is a bulk (Helmholtz) mode in which all pressure and velocity oscillations are in phase everywhere in the chamber and a nodal line is only present at the boundary of the domain. This corresponds to (one half of) the 2L mode of the composite preburner-turbine inlet assembly, which occurs at approximately the same frequency. Note that Helmholtz like behavior occurs in each

preburner in the composite assembly, but there is no low pressure region corresponding to the near field of the nodal surface and the frequency does not match. The frequency of the 1T mode identified in the single preburner also agrees exactly with that for the 1T mode identified in the composite preburner-turbine inlet hub assembly. Thus, correspondence between the two geometries is established.

Of particular interest are the decay constants found for the modes of the assembly of the preburners and turbine inlet hub. Due to its quasi-one dimensional geometry, the acoustic motions in the system are predominantly longitudinal. One might expect based on this qualitative observation that the impedance boundary condition imposed at the turbine inlet annulus would not be "activated" by virtue of its orientation. However as shown in Fig. 58, the geometry near this region is such that there is locally a component of acoustic velocity normal to the surface which results in damping of acoustic waves. The frequencies for all the longitudinal modes in the composite assembly are nontrivially changed when the turbine blade row boundary condition is changed; those for the 1L and 3L modes are higher for an acoustically closed boundary than for an open issue.

The 1T mode, by contrast, exhibits no damping constant because its oscillations are entirely removed from the turbine inlet annulus. Furthermore, the 1T oscillations on either end of the preburner-turbine inlet assembly are decoupled. In Fig. 57 the oscillations have been manually rotated so as to be displayed in a single plane. Fig. 58 more clearly shows that the spatial orientation of the transverse oscillations in each preburner are independent. This suggests the possibility of unique failure modes associated with transverse oscillations. Were a spinning 1T (or higher) oscillation to develop such that the mode in each preburner spun in a different direction or at a different rate in the same direction, a

periodic torque would be developed and act on the entire assembly. Likewise, if standing 1T oscillations of identical spatial phase in each preburner were to arise a periodic bending moment would be developed. Determination of which occurrence is more likely would depend on knowledge of the dynamics of spinning waves in the system. Evidence from annular combustors suggests that spinning or standing modes could be preferred depending on factors such as injector swirl, injector spacing, and equivalence ratio [82].

The 2L mode is revealed to be the most stable with the largest damping coefficient, while the 1L mode is least damped. This trend can be explained by considering the form of the impedance boundary condition. As seen from Fig. 15, the impedance, and hence the damping, increases with frequency until the maximum at a frequency of approximately 1935 Hz for the present system. Thus, higher longitudinal modes tend to be damped more effectively. The fact that the damping coefficient of the 3L mode is slightly less than that for the 2L mode can be attributed to the slightly shallower average angle of incidence on the turbine blade row exhibited by the oscillations of the 3L mode. In the case that the boundary is considered acoustically open, the 2L mode is completely suppressed.

No information about the absolute magnitude of the oscillations can be obtained from the present linear analysis. The distribution of acoustic velocity is of interest from a combustion dynamic perspective. As indicated by Fig. 57, the magnitude of the acoustic velocity is lower near the injectors that farther downstream for all longitudinal modes. For the transverse mode, the opposite is the case.

CHAPTER 6.

Conclusions and Future Work

6.1. Discussion

In this thesis a consistent methodology has been developed to conduct a linear acoustic stability analysis of ORSC rocket engines which incorporates realistic a realistic combustion response accounting for the complex turbulent combustion physics present in the engine. A numerical eigenvalue problem is solved utilizing the finite element code COMSOL to determine the effect of various physics on the growth rate of acoustic oscillations in the chamber. The two primary components of the engine to be considered in the stability analysis are the main combustion chamber and the preburner assembly.

Whereas in the main chamber the gas may be approximated as ideal, in the preburner the pressure is high enough that the fluid must be considered supercritical. A real fluid equation of state must be employed to correctly account for the speed of sound, and thus the frequency. The longitudinal modes in the composite assembly, in particular the global 2L mode, are most highly damped. By contrast the 2T mode is undamped because its oscillations are confined to the preburner injector region far away from the turbine inlet.

The largest contributor to the damping in the main chamber was found to be the mean velocity field. Two cases were considered: piecewise uniform mean flow and swirl flow derived from LES computations. The former provide an effective damping by convecting acoustic energy out of the domain, while the latter adds the effect of acoustic refraction. Incorporation of the combustion response was done by specifying volume

source terms in the wave equation utilizing Flame Transfer Function (FTF) gain and phase fields postprocessed from LES data. Responses for three different injector configurations were studied: full recess, intermediate recess, and full recess. Eigenvalue results indicated that the configuration with no recess produces the largest linear growth rate, indicating that it is the likeliest to be unstable. This is because the heat release oscillations associated with the base of the nonpremixed flame is most exposed to the transverse acoustic oscillations of the main chamber.

The net growth rate, that is the sum of all growth rates associated with individual physical processes studied, shows that the system is damped for all conditions; indeed there is a considerable stability margin. This is in qualitative agreement with the empirical observations regarding the combustion stability of the RD-170.

An adjoint sensitivity analysis was conducted to determine how the eigenvalue results change with perturbations in certain combustion response parameters which characterized the distributed fields. It was found that the most significant influences on the growth rate were the (maximum) FTF gain, the axial spread about the maximum gain, and the (maximum) axial phase slope. A rough analogy can be made between the axial phase slope and a combustion response time delay which helps to explain the importance of this quantity; however, the growth rate does not exhibit an oscillatory dependence on the phase slope over the perturbation range considered as it has been observed to with respect to time delay.

To recap, this thesis has made the following research contributions:

- Established a complete, consistent, linear stability analysis and applied it to a case study of a model engine which has a complex geometry and closely mimics a real ORSC engine.
- Incorporation of realistic chamber-level mean flow fields and distributed combustion response generated from LES of individual injectors. The effect of the injector design is investigated through simulations with three distinct injector recess lengths.
- A sensitivity analysis of a reduced set of scalar parameters characterizing the distributed combustion which demonstrate the controlling physics of the combustion-acoustic interactions for acoustically and convectively noncompact flames.

6.2. Future Work

This work has focused on linear stability and thus there remain several pieces of important physics to be explored further. The most notable omissions are the conditions under which the system will attain a limit cycle, and the corresponding amplitude of that limit cycle. These questions are difficult to answer for complex systems with realistic geometry and flow fields. Indeed the severe nonlinearity of the problem may require the problem to be addressed in a statistical sense. Additional nonlinear effects such as intermodal energy transfer may require dedicated investigation to clarify the relationship between certain physical problem parameters and quantities of interest.

The mean velocity field effect also deserves additional investigation. It has been a standing topic of discussion in the aeroacoustics research community for several decades which terms in the mean-flow wave equation should be kept on the right hand side as source terms, and which should be moved to the left hand side as part of the wave operator. The Culick and Yang framework utilized in this thesis is known to be consistent and correctly account for all the physics represented in its terms; however, there remain questions as to whether or not the no-flow wave operator on the left hand side of Eq. (15) is the optimal formulation for numerical studies utilizing the wave equation. There may be numerical artifacts which could be eliminated by utilizing instead, for example, the convective operator D/Dt. This may require more sophisticated numerical methods.

As the most important physical sub-model in the stability analysis, the combustion response deserves continued scrutiny so as to ensure accurate, meaningful results. The approximations utilized in this thesis, namely a purely pressure-coupled combustion response, may not be accurate under all circumstances. Further investigation is needed in which stability results are compared between pressure coupled and velocity coupled results. Furthermore, though the combustion response fields used in this thesis should contain all the relevant physics, much of that information remains opaque. In particular, no significant attempt was made to investigate one of the most interesting aspects of kinematic flame response: it is known from analyses of the level-set equations described briefly in Section 1.3.3. in the introduction that flame response is *non-local*. That is, because wrinkles convect at the local flow speed along the flame front, the combustion response at any point is due only partially to the underlying flow disturbance at that location, and partially to the flame wrinkle convecting from upstream. In other words the combustion response at any

point depends on the response history at all upstream locations. The proper incorporation of this effect is an open question. It is possible that space-lagged terms may be introduced into the wave equation, such that it ceases to be a differential equation and becomes instead an integro-differential equation. Fundamental theoretical and computational investigations are warranted to clarify this matter.

Additional experimental interrogation of the combustion response itself would also be extremely enlightening. The most obvious, and to some degree the easiest, avenue of experimental validation of the present methodology is direct comparison of the system acoustic stability results with acoustic pressure measurements in real instrumented engines. However the combustion response function is itself an important quantity which can be accessed through post-processing of experimental measurements. A campaign of experiments to investigate the spatial distribution of combustion response parameters and compare with the results of LES postprocessing could do much to help quantify the accuracy and uncertainty of results.

Perhaps the single most important piece of physics neglected in the current study is the combustion response in the preburner. Preburners are known anecdotally to exhibit a strong propensity to instability due to their high energy densities and relatively low internal damping, and complete investigation of combustion response in this environment is essential. This was not included in the preburner analysis in this work because of the lack of availability of a reliable LES dataset for the preburner injectors. Consistent LES of turbulent combustion in a supercritical preburner environment is a topic which itself deserves additional research attention.

APPENDIX A.

Derivation of Acoustic Wave Equation

The derivation of the nonlinear acoustic wave equation (15) begins with the conservation equations written for an idealized two phase flow. A mass conservation equation is written for both the gas and condensed phases, while a single momentum equation and a single energy equation is written for both phases:

$$\frac{\partial \rho_g}{\partial t} + \nabla \cdot \left(\rho_g \boldsymbol{u}\right) = w_c \tag{50}$$

$$\frac{\partial \rho_c}{\partial t} + \nabla \cdot \left(\rho_c \boldsymbol{u}_c\right) = -w_c \tag{51}$$

$$\frac{\partial}{\partial t}\left(\rho_g \boldsymbol{u} + \rho_c \boldsymbol{u}_c\right) + \nabla \cdot \left(\rho_g \boldsymbol{u}\boldsymbol{u} + \rho_c \boldsymbol{u}_c \boldsymbol{u}_c\right) + \nabla p = 0 \tag{52}$$

$$\frac{\partial}{\partial t}\left(\rho_g e_0 + \rho_c e_{c_0}\right) + \nabla \cdot \left(\rho_g e_0 \boldsymbol{u} + \rho_c e_{c_0} \boldsymbol{u}_c\right) + \nabla \cdot \left(p\boldsymbol{u}\right) = \dot{Q} \tag{53}$$

We have used the subscripts g and c to denote gas and condensed phases, respectively. However the velocity and energy of the gas phase have not been marked with a subscript. The symbol w_c represents the rate of mass conversion from condensed phase to gas phase per unit volume, and $\dot{Q}$ represents the rate of heat release due to combustion in the gas phase. The effects of finite viscosity and thermal conductivity have been neglected.

The first step is to reform the conservation equations into a set describing the flow as through only a single homogeneous phase were present. It shall have properties which are some combination of the physical properties of the actual gas and condensed phases,

which will be determined through the analysis. We shall begin by combining the mass conservation equations (50) and (51):

$$\frac{\partial \rho_g}{\partial t} + \nabla \cdot \left(\rho_g \boldsymbol{u}\right) + \frac{\partial \rho_l}{\partial t} + \nabla \cdot \left(\rho_l \boldsymbol{u}_l\right) = w_l - w_l$$

$$\frac{\partial \left(\rho_g + \rho_l\right)}{\partial t} + \nabla \cdot \left(\left(\rho_g + \rho_l\right)\boldsymbol{u}\right) + \nabla \cdot \left(\rho_l \delta \boldsymbol{u}_l\right) = 0$$

$$\frac{\partial \rho}{\partial t} + \nabla \cdot \left(\rho \boldsymbol{u}\right) + \nabla \cdot \left(\rho_l \delta \boldsymbol{u}_l\right) = 0$$

Then expanding and rearranging,

$$\frac{\partial \rho}{\partial t} + \boldsymbol{u} \cdot \nabla \rho = \underbrace{-\rho \nabla \cdot \boldsymbol{u} - \nabla \cdot \left(\rho_c \delta \boldsymbol{u}_c\right)}_{\dot{w}} \tag{54}$$

where we have defined the total density $\rho \equiv \rho_g + \rho_c$ and where the right hand side is an effective mass source term.

Next we move to the momentum equation. Expanding the derivatives, and introducing the two mass conservation equations (50) and (51), we have

$$\rho_g \frac{\partial \boldsymbol{u}}{\partial t} + \rho_g \boldsymbol{u} \cdot \nabla \boldsymbol{u} + \nabla p$$

$$= -\boldsymbol{u} \underbrace{\left[\frac{\partial \rho_g}{\partial t} + \nabla \cdot \left(\rho_g \boldsymbol{u}\right)\right]}_{w_c} - \boldsymbol{u}_c \underbrace{\left[\frac{\partial \rho_c}{\partial t} + \nabla \cdot \left(\rho_c \boldsymbol{u}_c\right)\right]}_{-w_c} - \rho_c \left[\frac{\partial \boldsymbol{u}_c}{\partial t} + \boldsymbol{u}_c \cdot \nabla \boldsymbol{u}_c\right]$$

Rearranging further,

$$\rho_g \frac{\partial \boldsymbol{u}}{\partial t} + \rho_g \boldsymbol{u} \cdot \nabla \boldsymbol{u} + \nabla p = \underbrace{-\rho_c \left(\frac{\partial \boldsymbol{u}_c}{\partial t} + \boldsymbol{u}_c \cdot \nabla \boldsymbol{u}_c\right)}_{\boldsymbol{F}_c} - \underbrace{w_c (\boldsymbol{u} - \boldsymbol{u}_c)}_{\boldsymbol{\sigma}}$$

where we identify $\boldsymbol{F}_c$ as the force of interaction between the gas and condensed phases, and $\boldsymbol{\sigma}$ as the momentum transfer to the gas from the condensed phase due to phase change.

The energy equation is manipulated in similar fashion, again introducing the continuity equations where appropriate as well as the state relations $e_0 = c_V T$ and $e_{c_0} = cT_c$:

$$\rho_g c_V \frac{\partial T}{\partial t} + \rho_g c_V \boldsymbol{u} \cdot \nabla T + \rho_c c \left(\frac{\partial T_c}{\partial t} + \boldsymbol{u}_c \cdot \nabla T_c \right) + \left(e_0 - e_{c_0} \right) w_c + \boldsymbol{u} \cdot \nabla p + p \nabla \cdot \boldsymbol{u} = \dot{Q}$$

From the foregoing we subtract $\boldsymbol{u}$ times the momentum equation to ultimately yield

$$\rho_g c_V \frac{\partial T}{\partial t} + \rho_g c_V \boldsymbol{u} \cdot \nabla T + p \nabla \cdot \boldsymbol{u}$$

$$= \dot{Q} \underbrace{- \rho_c c \left(\frac{\partial T_c}{\partial t} + \boldsymbol{u}_c \cdot \nabla T_c \right)}_{\dot{Q}_c} + \left(e_{c_0} - e_0 \right) w_c + \boldsymbol{u} \cdot \boldsymbol{\sigma} - \boldsymbol{u} \cdot \boldsymbol{F}_c + \boldsymbol{u}_c \cdot \underbrace{\rho_g \left(\frac{\partial \boldsymbol{u}}{\partial t} + \boldsymbol{u} \cdot \nabla \boldsymbol{u} \right)}_{\boldsymbol{F}_c}$$

where we have again identified the mutual force between the condensed and gas phases, as well as the heat transfer between them.

We introduce new variables to account for the deviation between the velocities and temperatures of the condensed and gas phases: $\delta \boldsymbol{u}_c = \boldsymbol{u}_c - \boldsymbol{u}$ and $\delta T_c = T_c - T$. Introducing these definitions into the foregoing equations and manipulating produces

$$\rho \frac{\partial \boldsymbol{u}}{\partial t} + \rho \boldsymbol{u} \cdot \nabla \boldsymbol{u} + \nabla p = \delta \boldsymbol{F}_c - \boldsymbol{\sigma} \tag{55}$$

$$\rho \bar{c}_V \left(\frac{\partial T}{\partial t} + \boldsymbol{u} \cdot \nabla T \right) + p \nabla \cdot \boldsymbol{u} = \dot{Q} + \delta \dot{Q}_c + \left(e_{c_0} - e_0 \right) w_c + \boldsymbol{u} \cdot \boldsymbol{\sigma} + \delta \boldsymbol{u}_c \cdot \boldsymbol{F}_c \tag{56}$$

where

$$\delta \boldsymbol{F}_c = -\rho_c \left(\frac{\partial \delta \boldsymbol{u}_c}{\partial t} + \delta \boldsymbol{u}_c \cdot \nabla \delta \boldsymbol{u}_c + \delta \boldsymbol{u}_c \cdot \nabla \boldsymbol{u} + \boldsymbol{u} \cdot \nabla \delta \boldsymbol{u}_c \right)$$

$$\delta \dot{Q}_c = -\rho_c c \left(\frac{\partial \delta T_c}{\partial t} + \delta \boldsymbol{u}_c \cdot \nabla \delta T_c + \delta \boldsymbol{u}_c \cdot \nabla T + \boldsymbol{u} \cdot \nabla \delta T_c \right)$$

$$\boldsymbol{\sigma} = -\delta \boldsymbol{u}_c w_c$$

and where the mass weighted specific heat of the two-phase mixture $\bar{c}_V \equiv (c_V + c_m c)/(1 + c_m)$, where $c_m \equiv \rho_c / \rho_g$.

Now, the mass conservation equation and momentum equation are in acceptable form, but the energy equation must be put in terms of pressure rather than temperature. This is easily done by means of ideal gas relationships to leave finally the reformed system of conservation equations as follows:

$$\frac{\partial \rho}{\partial t} + \boldsymbol{u} \cdot \nabla \rho = \mathcal{W} \tag{57}$$

$$\rho \frac{\partial \boldsymbol{u}}{\partial t} + \rho \boldsymbol{u} \cdot \nabla \boldsymbol{u} = -\nabla p + \boldsymbol{\mathcal{F}} \tag{58}$$

$$\frac{\partial p}{\partial t} + \bar{\gamma} p \nabla \cdot \boldsymbol{u} + \boldsymbol{u} \cdot \nabla p = \mathcal{P} \tag{59}$$

where

$$\mathcal{W} = -\rho \nabla \cdot \boldsymbol{u} - \nabla \cdot (\rho_c \delta \boldsymbol{u}_c) \tag{60}$$

$$\boldsymbol{\mathcal{F}} = \delta \boldsymbol{F}_c + \delta \boldsymbol{u}_c w_c \tag{61}$$

$$\mathcal{P} = \frac{\bar{R}}{\bar{c}_V} \left[\dot{Q} + \delta \dot{Q}_c + \delta \boldsymbol{u}_c \cdot \boldsymbol{F}_c + \left(e_{c_0} - e_0 - \boldsymbol{u} \cdot \delta \boldsymbol{u}_c \right) w_c - \bar{c}_V T \nabla \cdot (\rho_c \delta \boldsymbol{u}_c) \right] \tag{62}$$

The system of equations above is a single set of conservation equations governing the two-phase mixture as though it were a single phase mixture with gas properties that are appropriate combinations of the real mixture.

We decompose all flow quantities into their mean and fluctuating components as $\rho(\boldsymbol{r},t)=\bar{\rho}+\rho'(\boldsymbol{r},t)$, $\boldsymbol{u}(\boldsymbol{r},t)=\overline{\boldsymbol{u}}(\boldsymbol{r})+\boldsymbol{u}'(\boldsymbol{r},t)$, and $p(\boldsymbol{r},t)=\bar{p}+p'(\boldsymbol{r},t)$, where we have assumed that the mean density and pressure are uniform throughout the system, while the mean velocity is allowed to vary in space. These assumptions are not strictly necessary, and indeed there may be nontrivial effects associated with, for example, spatially varying mean density. However these generalizations are tedious and may be safely disregarded in the systems under consideration. The perturbations are assumed to satisfy $\rho'/\bar{\rho}$, $\boldsymbol{u}'/\overline{\boldsymbol{u}}$, $p'/\bar{p}\ll 1$. We introduce these decompositions into the system (57)-(59) and retain terms up to second order in small perturbations. Note that there are in fact *two* asymptotic parameters implicit in this analysis, the wave amplitude and the mean flow Mach number. Under this formulation, terms proportional to $|\overline{\boldsymbol{u}}|^2|\boldsymbol{u}'|$, $|\overline{\boldsymbol{u}}||\boldsymbol{u}'|^2$, or $|\boldsymbol{u}'|^3$ are all third order terms and may be discarded. For a more rigorous explication of the asymptotic analysis, the reader is referred to Ref [20]. After these simplifications, the unsteady momentum and energy equations are

$$\bar{\rho}\frac{\partial \boldsymbol{u}'}{\partial t}+\nabla p'=-\bar{\rho}(\overline{\boldsymbol{u}}\cdot\nabla\boldsymbol{u}'+\boldsymbol{u}'\cdot\nabla\overline{\boldsymbol{u}}+\boldsymbol{u}'\cdot\nabla\boldsymbol{u}')-\rho'\frac{\partial \boldsymbol{u}'}{\partial t}+\boldsymbol{\mathcal{F}}' \tag{63}$$

and

$$\frac{\partial p'}{\partial t}+\bar{\gamma}\bar{p}\nabla\cdot\boldsymbol{u}'=-\overline{\boldsymbol{u}}\cdot\nabla p'-\bar{\gamma}p'\nabla\cdot\overline{\boldsymbol{u}}-\boldsymbol{u}'\cdot\nabla p'-\bar{\gamma}p'\nabla\cdot\boldsymbol{u}'+\mathcal{P}' \tag{64}$$

where the fluctuating forces and energy sources are contained in the final groups in the foregoing equations. Explicitly, they are:

$$\boldsymbol{\mathcal{F}}' = \delta \boldsymbol{F}_c' + \delta \boldsymbol{u}_c w_c' \tag{65}$$

and

$$\mathcal{P}' = (\bar{\gamma} - 1)\big[\dot{Q}' + \delta \dot{Q}_c + \delta \boldsymbol{u}_c \cdot \boldsymbol{F}_c' + \big(e_{c_0}' - e_0' - \boldsymbol{u}' \cdot \delta \boldsymbol{u}_c\big)\bar{w}_c + \big(\bar{e}_{c_0} - \bar{e}_0 - \bar{\boldsymbol{u}} \cdot \delta \boldsymbol{u}_c\big)w_c' - \bar{c}_V T' \nabla \cdot (\bar{\rho}_c \delta \boldsymbol{u}_c) - \bar{c}_V \bar{T} \nabla \cdot (\rho_c' \delta \boldsymbol{u}_c)\big] \tag{66}$$

For most systems, the volumetric source term (66) is dominated by the chemical heat release due to combustion in the gas phase, $\dot{Q}'$.

Finally, these equations are combined to form a nonlinear wave equation in the acoustic pressure. First differentiate Eq. (64) with respect to time:

$$\frac{\partial^2 p'}{\partial t^2} + \bar{\gamma}\bar{p} \nabla \cdot \left(\frac{\partial \boldsymbol{u}'}{\partial t}\right) = -\bar{\boldsymbol{u}} \cdot \frac{\partial (\nabla p')}{\partial t} - \bar{\gamma}\left(\frac{\partial p'}{\partial t}\right) \nabla \cdot \bar{\boldsymbol{u}} - \left(\frac{\partial \boldsymbol{u}'}{\partial t}\right) \cdot \nabla p' - \boldsymbol{u}' \cdot \frac{\partial (\nabla p')}{\partial t} - \bar{\gamma}\left(\frac{\partial p'}{\partial t}\right) \nabla \cdot \boldsymbol{u}' - \bar{\gamma} p' \nabla \cdot \left(\frac{\partial \boldsymbol{u}'}{\partial t}\right) + \frac{\partial \mathcal{P}'}{\partial t}$$

Then we may introduce Eq. (63) to eliminate the unsteady acceleration term. After some simplification and rearrangement there results

$$\frac{1}{\bar{\rho}\bar{c}^2}\frac{\partial^2 p'}{\partial t^2} - \frac{1}{\bar{\rho}}\nabla^2 p' = -\frac{1}{\bar{\rho}\bar{c}^2}\left(\overline{\boldsymbol{u}}\cdot\nabla\frac{\partial p'}{\partial t} + \bar{\gamma}\frac{\partial p'}{\partial t}\nabla\cdot\overline{\boldsymbol{u}} + \frac{\partial(\boldsymbol{u}'\cdot\nabla p')}{\partial t} + \bar{\gamma}\frac{\partial(p'\nabla\cdot\boldsymbol{u}')}{\partial t} - \frac{\partial\mathcal{P}'}{\partial t}\right) + \frac{1}{\bar{\rho}}\nabla\cdot\left(\bar{\rho}(\overline{\boldsymbol{u}}\cdot\nabla\boldsymbol{u}' + \boldsymbol{u}'\cdot\nabla\overline{\boldsymbol{u}}) + \bar{\rho}\boldsymbol{u}'\cdot\nabla\boldsymbol{u}' + \rho'\frac{\partial\boldsymbol{u}'}{\partial t} - \boldsymbol{\mathcal{F}}'\right) \tag{67}$$

The two groups on the right hand side are then identified as respectively $\mathcal{M}$ and $\boldsymbol{\mathcal{D}}$ as defined in Section 2.1. This equation must be supplemented by a boundary condition on the acoustic pressure. Taking the dot product of Eq. (63) with a unit normal vector $\boldsymbol{n}$ pointing toward the interior of the domain, we find

$$-\frac{1}{\bar{\rho}}(\boldsymbol{n}\cdot\nabla p') = \boldsymbol{n}\cdot\frac{\partial\boldsymbol{u}'}{\partial t} + \boldsymbol{n}\cdot(\overline{\boldsymbol{u}}\cdot\nabla\boldsymbol{u}' + \boldsymbol{u}'\cdot\nabla\overline{\boldsymbol{u}} + \boldsymbol{u}'\cdot\nabla\boldsymbol{u}') + \frac{1}{\bar{\rho}}\boldsymbol{n}\cdot\left(\rho'\frac{\partial\boldsymbol{u}'}{\partial t}\right) + \frac{1}{\bar{\rho}}\boldsymbol{n}\cdot\boldsymbol{\mathcal{F}}' \tag{68}$$

also as listed in Section 2.1.

REFERENCES

[1] Lieuwen, T. C. and Yang, V., *Combustion Instabilities in Gas Turbine Engines: Operational Experience, Fundamental Mechanisms and Modeling*, Progress in Astronautics and Aeronautics, Vol. 210. AIAA, 2005.

[2] Choi, J.-Y., Ma, F. and Yang, V., "Combustion Oscillations in a Scramjet Engine Combustor with Transverse Fuel Injection," *Proceedings of the Combustion Institute*, Vol. 30, 2, 2005. pp. 2851-2858

[3] Lin, K.-C., Jackson, K., Behdadnia, R., Jackson, T. A., Ma, F. and Yang, V., "Acoustic Characterization of an Ethylene-Fueled Scramjet Combustor with a Cavity Flameholder," *Journal of Propulsion and Power*, Vol. 26, 6, 2010. pp. 1161-1170

[4] De Luca, L., Price, E. W. and Summerfield, M., *Nonsteady Burning and Combustion Stability of Solid Propellants*, Progress in Astronautics and Aeronautics, Vol. 143. AIAA, 1992.

[5] Yang, V., Brill, T. B. and Ren, W., *Solid Propellant Chemistry Combustion and Motor Interior Ballistics*, Progress in Astronautics and Aeronautics, Vol. 185. AIAA, 2000.

[6] Anderson, W. E. and Yang, V., *Liquid Rocket Engine Combustion Instability*, Progress in Astronautics and Aeronautics, Vol. 169. University Park, Pennsylvania. AIAA, 1995. DOI: 10.2514/4.866371

[7] Dranovsky, M. L., Yang, V., Culick, F. E. C. and Talley, D. G., *Combustion Instabilities in Liquid Rocket Engines: Testing and Development Practices in Russia*, Progress in Astronautics and Aeronautics, Vol. 221. AIAA, 2007.

[8] Yang, V., Ku, D. D., Walker, M. L. R., Williams, L. and Leahy, J. C., "Liquid Oxygen/Kerosene Staged Combustion Rocket Engines with Oxidizer-Rich Preburners," NASA/TP-2015-218203, 2015.

[9] Yang, V., Ku, D. D., Lioi, C. B., Yeh, S.-T., Leahy, J. C. and Kenny, R. J., "Liquid Oxygen/Kerosene Oxidizer-Rich, Staged Combustion Engine Technology Development," NASA/TP-2016-218226, 2016.

[10] Rayleigh, J. W. S., *The Theory of Sound, Vols. I and II*, Vol. Dover Publications, New York, 1945.

[11] Culick, F. E. C., "A Note on Rayleigh's Criterion," *Combustion Science and Technology*, Vol. 56, 4-6, 1987. pp. 159-166

[12] Oefelein, J. C. and Yang, V., "Modeling High-Pressure Mixing and Combustion Processes in Liquid Rocket Engines," *Journal of Propulsion and Power*, Vol. 14, 1998. pp. 843-857

[13] Yang, V., "Modeling of Supercritical Vaporization, Mixing, and Combustion Processes in Liquid-Fueled Propulsion Systems," *Proceedings of the Combustion Institute*, Vol. 28, 1, 2000. pp. 925-942

[14] Meng, H. and Yang, V., "A Unified Treatment of General Fluid Thermodynamics and its Application to a Preconditioning Scheme," *Journal of Computational Physics*, Vol. 189, 1, 2003. pp. 277-304

[15] Katorgin, B. I. and Chelkis, F. J., "The RD-170, A Different Approach to Launch Vehicle Propulsion," presented at the AIAA/SAE/ASME/ASEE 29th Joint Propulsion Conference and Exhibit, Monterey, CA, 1993.

[16] Pieringer, J., Sattelmayer, T. and Fassl, F., "Simulation of Combustion Instabilities in Liquid Rocket Engines with Acoustic Perturbation Equations," *Journal of Propulsion and Power*, Vol. 25, 5, 2009. pp. 1020-1031 DOI: 10.2514/1.38782

[17] Schulze, M. and Sattelmayer, T., "Low-Order Modelling of the Non-Local Acoustic Reacting Combustion Chamber-Dome Interface in Rocket Engines," in 19th AIAA International Space Planes and Hypersonic Systems and Technologies Conference - Paper 3086, Atlanta, GA, 2014.

[18] Culick, F. E. C., "Stability of Three-Dimensional Motions in a Combustion Chamber," *Combustion Science and Technology*, Vol. 10, 3-4, 1975. pp. 109-124

[19] Culick, F. E. C. and Yang, V., "Prediction of the Stability of Unsteady Motions in Solid-Propellant Rocket Motors," in Nonsteady Burning and Combustion Stability of Solid Propellants, Vol. 143, L. De Luca, E. W. Price and M. Summerfield, ed. AIAA, 1992, pp. 719-779.

[20] Culick, F. E. C., "Unsteady Motions in Combustion Chambers for Propulsion Systems," North Atlantic Treaty Organization, NATO/RTO-AG-AVT-039, 2006.

[21] Culick, F. E. C. and Yang, V., "Overview of Combustion Instabilities in Liquid-Propellant Rocket Engines," in Liquid Rocket Engine Combustion Instability, Vol. 169, W. E. Anderson and V. Yang, ed. AIAA, 1995, pp. 3-37.

[22] Culick, F. E. C., "Nonlinear Behavior of Acoustic Waves in Combustion Chambers—I," *Acta Astronautica*, Vol. 3, 9, 1976. pp. 715-734

[23] Yang, V., Kim, S. I. and Culick, F. E. C., "Triggering of Longitudinal Pressure Oscillations in Combustion Chambers. I: Nonlinear Gasdynamics," *Combustion Science and Technology*, Vol. 72, 4-6, 1990. pp. 183-214

[24] Wicker, J. M., Greene, W. D., Kim, S.-I. and Yang, V., "Triggering of Longitudinal Combustion Instabilities in Rocket Motors-Nonlinear Combustion Response," *Journal of Propulsion and Power*, Vol. 12, 6, 1996. pp. 1148-1158

[25] Wicker, J. M., Yoon, M. W. and Yang, V., "Linear and Non-linear Pressure Oscillations in Baffled Combustion Chambers," *Journal of Sound and Vibration*, Vol. 184, 1, 1995. pp. 141-171

[26] Yang, V., Kim, S. I. and Culick, F. E. C., "Third-Order Nonlinear Acoustic Instabilities in Combustion Chambers, Part I: Longitudinal Modes," presented at the AIAA/SAE/ASME 23rd Joint Propulsion Conference, San Diego, CA, 1987.

[27] Yang, V., Kim, S. I. and Culick, F. E. C., "Third-Order Nonlinear Acoustic Instabilities in Combustion Chambers, Part II: Transverse Modes," in AIAA 26th Aerospace Sciences Meeting, Reno, NV, 1988: AIAA.

[28] Williams, F. A., *Combustion Theory*, 2nd, Vol. The Benjamin/Cummings Publishing Company, Inc., 1985.

[29] Peters, N., *Turbulent Combustion*, Vol. Cambridge, United Kingdom. Cambridge University Press, 2000.

[30] Fleifil, M., Annaswamy, A. M., Ghoneim, Z. A. and Ghoniem, A. F., "Response of a Laminar Premixed Flame to Flow Oscillations: A Kinematic Model and Thermoacoustic Instability Results," *Combustion and Flame*, Vol. 106, 1996. pp. 487-510

[31] You, D., Huang, Y. and Yang, V., "A Generalized Model of Acoustic Response of Turbulent Premixed Flame and its Application to Gas-Turbine Combustion Instability Analysis," *Combustion Science and Technology*, Vol. 177, 2005. pp. 1109-1150

[32] Cho, J. H. and Lieuwen, T. C., "Laminar Premixed Flame Response to Equivalence Ratio Oscillations," *Combustion and Flame*, Vol. 140, 2005. pp. 116-129

[33] Shreekrishna, Hemchandra, S. and Lieuwen, T. C., "Premixed Flame Response to Equivalence Ratio Perturbations," *Combustion Theory and Modelling*, Vol. 14, 2010. pp. 681-714

[34] Wang, H. Y., Law, C. K. and Lieuwen, T. C., "Linear Response of Stretch-Affected Premixed Flames to Flow Oscillations," *Combustion and Flame*, Vol. 156, 2009. pp. 889-895

[35] Preetham, S. H., Thumuluru, S. K., Lieuwen, T. C. and Hemchandra, S., "Linear Response of Laminar Premixed Flames to Flow Oscillations: Unsteady Stretch Effects," *Journal of Propulsion and Power*, Vol. 26, 2010. pp. 524-532

[36] Hemchandra, S., Peters, N. and Lieuwen, T. C., "Heat Release Response of Acoustically Forced Turbulent Premixed Flames—Role of Kinematic Restoration," *Proceedings of the Combustion Institute*, Vol. 33, 2011. pp. 1609-1617

[37] Tyagi, M., Chakravarthy, S. R. and Sujith, R. I., "Unsteady Combustion Response of a Ducted Non-Premixed Flame and Acoustic Coupling," *Combustion Theory and Modelling*, Vol. 11, 2007. pp. 205-226

[38] Balasubramanian, K. and Sujith, R. I., "Nonlinear Response of Diffusion Flames to Uniform Velocity Disturbances," *Combustion Science and Technology*, Vol. 180, 2008. pp. 418-436

[39] Magina, N., Shin, D.-H., Acharya, V. and Lieuwen, T. C., "Response of Non-Premixed Flames to Bulk Flow Perturbations," *Proceedings of the Combustion Institute*, Vol. 34, 2013. pp. 963-971

[40] Magina, N. and Lieuwen, T. C., "Effect of Axial Diffusion on the Response of Over-Ventilated Diffusion Flames to Axial Flow Perturbations," in 52nd Aerospace Science Meeting, 2014.

[41] Magina, N., Acharya, V., Sun, T. and Lieuwen, T. C., "Propagation, Dissipation, and Dispersion of Disturbances on Harmonically Forced, Non-Premixed Flames," *Proceedings of the Combustion Institute*, Vol. 35, 2015. pp. 1097-1105

[42] Magina, N. A. and Lieuwen, T. C., "Effect of Axial Diffusion on the Response of Diffusion Flames to Axial Flow Perturbations," *Combustion and Flame*, Vol. 167, 2016. pp. 395-408

[43] Lieuwen, T. C., "Modeling Premixed Combustion-Acoustic Wave Interactions: A Review," *Journal of Propulsion and Power*, Vol. 19, 5, 2003. pp. 765-781

[44] Zong, N. and Yang, V., "Near-Field Flow and Flame Dynamics of LOX/Methane Shear-Coaxial Injector Under Supercritical Conditions," *Proceedings of the Combustion Institute*, Vol. 31, 2007. pp. 2309-2317

[45] Wang, X. and Yang, V., "Supercritical Mixing and Combustion of Liquid-Oxygen/Kerosene Bi-Swirl Injectors," *Journal of Propulsion and Power*, Vol. 33, 2, 2016. pp. 316-322

[46] Tamanampudi, G. M. R. and Anderson, W. E., "Development of Combustion Instability Analysis Tool by Incorporating Combustion Response Models," in 51st

AIAA/SAE/ASEE Joint Propulsion Conference, Orlando, FL, 2015: AIAA Paper 2015-4165.

[47] Martin, C. E., Benoit, L. J.-L., Sommerer, Y., Nicoud, F. and Poinsot, T., "Large-Eddy Simulation and Acoustic Analysis of a Swirled Staged Turbulent Combustor," *AIAA Journal*, Vol. 44, 4, 2006. pp. 741-750 10.2514/1.14689

[48] Kim, S.-K., Choi, H. S., Kim, H. J., Ko, Y. S. and Sohn, C. H., "Finite Element Analysis for Acoustic Characteristics of Combustion Stabilization Devices," *Aerospace Science and Technology*, Vol. 42, April-May 2015. pp. 229-240

[49] Urbano, A., Selle, L., Staffelbach, G., Cuenot, B., Schmitt, T., Ducruix, S. and Candel, S. M., "Exploration of combustion instability triggering using Large Eddy Simulation of a multiple injector Liquid Rocket Engine," *Combustion and Flame*, Vol. 169, 2016. pp. 129-140

[50] Urbano, A., Douasbin, Q., Selle, L., Staffelbach, G., Cuenot, B., Schmitt, T., Ducruix, S. and Candel, S., "Study of flame response to transverse acoustic modes from the LES of a 42-injector rocket engine," *Proceedings of the Combustion Institute*, Vol. 2016. pp.

[51] Durox, D., Schuller, T., Noiray, N., Birbaud, A.-L. and Candel, S. M., "Rayleigh Criterion and Acoustic Energy Balance in Unconfined Self-Sustained Oscillating Flames," *Combustion and Flame*, Vol. 156, 2009. pp. 106-119

[52] Myers, M. K., "On the Acoustic Boundary Condition in the Presence of Flow," *Journal of Sound and Vibration*, Vol. 71, 3, 1980. pp. 429-434

[53] Lemmon, E. W., Huber, M. L. and McLinden, M. O., "NIST Standard Reference Database 23, Fluid Thermodynamic and Transport Properties REFPROP, User's Guide," National Institute of Standards and Technology (NIST), 2013

[54] Kunz, O. and Wagner, W., "The GERG-2008 Wide-Range Equation of State for Natural Gases and Other Mixtures: An Expansion of GERG-2004," *Journal of Chemical & Engineering Data*, Vol. 57, 11, 2012. pp. 3032-3091 10.1021/je300655b

[55] Hughes, I. J. and Dowling, A. P., "The Absorption of Sound by Perforated Linings," *Journal of Fluid Mechanics*, Vol. 218, 1990. pp. 299-335

[56] Howe, M. S., "On the Theory of Unsteady High Reynolds Number Flow Through a Circular Aperture," *Proceedings of the Royal Society of London A: Mathematical, Physical and Engineering Sciences*, Vol. 366, 1725, 1979. pp. 205-223 DOI: 10.1098/rspa.1979.0048

[57] Howe, M. S., *Acoustics of Fluid-Structure Interactions*, Vol. Cambridge University Press, 1998.

[58] Luong, T., Howe, M. S. and McGowan, R. S., "On the Rayleigh Conductivity of a Bias-Flow Aperture," *Journal of Fluids and Structures*, Vol. 21, 8, 2005. pp. 769-778

[59] Searby, G., Habiballah, M., Nicole, A. and Laroche, E., "Prediction of the Efficiency of Acoustic Damping Cavities," *Journal of Propulsion and Power*, Vol. 24, 3, 2008. pp. 516-523 DOI: 10.2514/1.32325

[60] Flandro, G. A., Cai, W. and Yang, V., "Turbulent Transport in Rocket Motor Unsteady Flowfield," in Solid Propellant Chemistry, Combustion, and Motor Interior Ballistics, Vol. 185, ed. (Progress in Astronautics and Aeronautics). AIAA, 2000, pp. 837-858.

[61] Apte, S. and Yang, V., "Unsteady Flow Evolution in Porous Chamber with Surface Mass Injection, Part 2: Acoustic Excitation," *AIAA Journal*, Vol. 40, 2, 2002. pp. 244-253 DOI: 10.2514/2.1666

[62] Kaji, S. and Okazaki, T., "Propagation of Sound Waves Through a Blade Row: I. Analysis Based on the Semi-Actuator Disk Theory," *Journal of Sound and Vibration*, Vol. 11, 3, 1970. pp. 339-353

[63] Kaji, S. and Okazaki, T., "Propagation of Sound Waves Through a Blade Row: II. Analysis Based on the Acceleration Potential Method," *Journal of Sound and Vibration*, Vol. 11, 3, 1970. pp. 355-375

[64] Muir, R. S., "The Application of a Semi-Actuator Disk Model to Sound Transmission Calculations in Turbomachinery, Part I: The Single Blade Row," *Journal of Sound and Vibration*, Vol. 54, 3, 1977. pp. 393-408

[65] Dowling, A. P. and Mahmoudi, Y., "Combustion Noise," *Proceedings of the Combustion Institute*, Vol. 35, 1, 2015. pp. 65-100

[66] Cumpsty, N. A. and Marble, F. E., "The Interaction of Entropy Fluctuations with Turbine Blade Rows; A Mechanism of Turbojet Engine Noise," *Proceedings of the Royal Society of London A: Mathematical, Physical and Engineering Sciences*, Vol. 357, 1690, 1977. pp. 323-344 DOI: 10.1098/rspa.1977.0171

[67] Bauerheim, M., Duran, I., Livebardon, T., Wang, G., Moreau, S. and Poinsot, T., "Transmission and Reflection of Acoustic and Entropy Waves Through a Stator–Rotor Stage," *Journal of Sound and Vibration*, Vol. 374, 21, 2016. pp. 260-278

[68] Wang, X. and Yang, V., "High-Fidelity Simulation of Combustion Processes in Liquid Rocket Engines," in 10th U. S. National Combustion Meeting, College Park, Maryland, 2017: The Combustion Institute.

[69] Zhang, L., Wang, X., Li, Y., Yeh, S.-T. and Yang, V., "Supercritical Fluid Flow Dynamics and Mixing in a Gas-Centered Liquid-Swirl Coaxial Injector," *Physics of Fluids*, Vol. 30, 2018. pp.

[70] Lumley, J. L., "The Structure of Inhomogeneous Turbulent Flows," *Atmospheric Turbulence and Radio Wave Propagation*, Vol. 790, 1967. pp. 166-178

[71] Loeve, M., *Probability Theory: Foundations, Random Sequences*, Vol. van Nostrand Princeton, NJ, 1955.

[72] Berkooz, G., Holmes, P. and Lumley, J. L., "The Proper Orthogonal Decomposition in the Analysis of Turbulent Flows," *Annual Review of Fluid Mechanics*, Vol. 25, 1, 1993. pp. 539-575

[73] Box, G. E. P. and Jenkins, G. M., *Time Series Analysis, Control, and Forecasting*, Vol. 3226. San Francisco, CA. Holden Day, 1976.

[74] Yeh, S.-T., Wang, X., Li, Y., Zhang, L. and Yang, V., "Identification and Quantification of Intrinsic Combustion Dynamics in a Rocket Injectors," *Combustion and Flame*, Vol. 2018. pp.

[75] Magri, L. and Juniper, M. P., "Adjoint-Based Linear Analysis in Reduced-Order Thermo-Acoustic Models," *International Journal of Spray and Combustion Dynamics*, Vol. 6, 3, 2014. pp. 225-246

[76] Magri, L., Bauerheim, M. and Juniper, M. P., "Stability Analysis of Thermo-Acoustic Nonlinear Eigenproblems in Annular Combustors. Part I. Sensitivity," *Journal of Computational Physics*, Vol. 325, 2016. pp. 395-410

[77] Silva, C. F., Magri, L., Runte, T. and Polifke, W., "Uncertainty Quantification of Growth Rates of Thermoacoustic Instability by an Adjoint Helmholtz Solver," *Journal of Engineering for Gas Turbines and Power,* Vol. 139, 1, 2017. pp. 1-14 10.1115/1.4034203

[78] Luchini, P. and Bottaro, A., "Adjoint Equations in Stability Analysis," *Annual Review of Fluid Mechanics*, Vol. 46, 2014. pp. 493-517

[79] You, D., Ku, D. D. and Yang, V., "Acoustic Waves in Baffled Combustion Chamber with Radial and Circumferential Blades," *Journal of Propulsion and Power*, Vol. 29, 6, 2013. pp. 1453-1467

[80] Li, L., Sun, X., Lioi, C. and Yang, V., "Effect of Azimuthally Nonuniform Heat Release on Longitudinal Combustion Instabilities," *Journal of Propulsion and Power*, Vol. 33, 1, 2016. pp. 193-203

[81] Dowling, A. P. and Stow, S. R., "Acoustic Analysis of Gas Turbine Combustors," *Journal of Propulsion and Power,* Vol. 19, 5, 2003. pp. 751-764 DOI: 10.2514/2.6192

[82] Worth, N. A. and Dawson, J. R., "Modal Dynamics of Self-Excited Azimuthal Instabilities in an Annular Combustion Chamber," *Combustion and Flame*, Vol. 160, 11, 2013. pp. 2476-2489